Realistic Modelling of Water/Solid Interfaces from *Ab Initio* Molecular Dynamics

Gabriele Tocci

A dissertation submitted in partial fulfilment of
the requirements for the degree of

Doctor of Philosophy

of the

University College London

Department of Chemistry

UCL

1^{st} Supervisor
Prof. Angelos Michaelides

2^{nd} Supervisor
Prof. Geoff Thornton

1st December 2014

I, Gabriele Tocci confirm that the work presented in this thesis is my own. Where information has been derived from other sources, I confirm that has been indicated in the thesis.

Abstract

Water/solid interfaces are of utmost importance to a number of technological processes. Theoretical studies, based on *ab initio* approaches are suitable to unveil processes occurring at water/solid interfaces and can therefore be instrumental to delineate guidelines to improve the efficiency of these processes. In this thesis we study several systems of current interest using *ab initio* methods based on density functional theory (DFT). By going often beyond the use of standard DFT methods and approximations we have provided insights into processes occurring at water/solid interfaces under ambient conditions and in non stoichiometric conditions. Specifically, we will investigate the interactions between water and ZnO, an important metal-oxide especially used in industry to produce methanol. One of the most important results of this study is that proton hopping is dramatically enhanced under wet conditions compared to ideal ultra-high vacuum conditions. Also, we will compute the friction between liquid water in contact with 2-D layered materials, and delineate the guidelines on how to alter the friction coefficient in membranes used for desalination or osmotic power harvesting. Finally, in collaboration with Geoff Thornton's group we have investigated the role of defects on the surface chemistry of the rutile $TiO_2(110)$, which is *the* model oxide surface used in photocatalysis applications. On the whole, in this work we have used *ab initio* methods to reduce the gap between the ultra-high vacuum-style studies of adsorption on perfect defect-free surfaces and the complex behaviour of liquid/solid interfaces under technologically relevant conditions.

Contents

Chapter 1

Introduction

The interface between water and other substances is important to an enormous amount of phenomena in science, technology and in our every day life. For instance, water is often considered to be the matrix of life for its active role in biological systems (see *e.g.* Refs. [1, 2]). Also, water and aqueous solutions in general are commonly used in electrochemistry. Applications include hydrogen production from water splitting in photoelectrochemical cells [3], and the energy conversion in fuel cells from H_2 to produce electricity and water as an exhaust product. Further, in the earth sciences the hydrological cycle involves a series of complex multi-scale processes going from water precipitation to water evaporation, which are all fundamental to life on our planet.

We could mention a never ending list of examples where the interactions between water and other substrates or solutes are crucial, but the few ones already tell us how broad and important the field of water/solid interfaces

is. As scientists interested in the properties of water at interfaces, our goal would be to understand the nature of these interactions in intimate details, up to the molecular level; to then be able to control and tailor the properties of their constituent materials to finally produce a desired result. Referring to the examples above, one such result could be for instance the development of drugs that can bind more effectively to their targets to block specific enzymes, and this may be achieved through the understanding of the molecular structure and dynamics of hydrated proteins [2]. Also, through the study of the molecular structure of water adsorbed on solid surfaces and their interactions with light, we hope to find the guidelines to design more efficient photocatalysts for the splitting of water, so as to make the production of H_2 more affordable [4]. Further, by looking at the microscopic processes occurring during ice formation in the atmosphere, we may design agents to prevent or facilitate ice nucleation and thus enhance or limit the precipitation in a specific region of the atmosphere.

In the mentioned examples the crucial steps are to reach molecular level understanding of the interface of interest and then to control and modify its properties. The idea to monitor and control the properties of materials down to the atomic scale was perhaps first envisaged by Feynman in his popular talk at the American Physical Society in 1959 "There's Plenty of Room at the Bottom" [5]. Since Feynman's inspiring talk a lot of progress has been made in the miniaturization of devices through *e.g.* the technique of lithography and in the imaging of ever smaller systems, especially using electron microscopes. However, not until the development of the scanning tunneling microscope (STM) in 1980s did it become possible to image and

move atoms in a controlled manner [6–8]. As a proof of the capabilities of the STM, at the beginning researchers at IBM wrote the name of their company moving individual Xenon atoms on a Ni(110) surface at 4 K [8]. Now they have gone further, and they have created a movie of a boy playing with a ball using CO molecules on a Cu substrate at around 5 K [9]. One of the possible developments stemming from atomic-scale manipulation at this level of complexity could be the design of atomic-scale memory for very big data storage.

There is a large body of knowledge coming from STM surface science style studies on the structure of water/metal and water/oxide interfaces [10, 11]. However, STM is not suitable to investigate water/solid interfaces under ambient conditions, because experiments are performed under ultra-high vacuum (UHV) conditions and often at cryogenic temperatures. Even with the atomic force microscope (AFM), that can be used to investigate liquid/solid interfaces under ambient conditions, atomic resolution of complex interfaces has not been achieved so far. Other techniques such as ambient pressure photoelectron spectroscopy (APPS) have been used to gain insights on the structure and the reactivity of liquid/solid interfaces [12]. Nevertheless, APPS being a spectroscopic technique, real space imaging is not possible, nor is atomic-scale manipulation. Further, under ambient conditions important processes occurring at the interface between liquid water and solid surfaces are usually too fast to be temporally resolved using current techniques. An important example is proton transfer at liquid water/solid interfaces, which may occur on the femtosecond time scale. Monitoring spontaneous proton transfer has not been achieved, but a way has been found to monitor proton

transfer in solution via irradiation using infrared spectroscopy [13, 14]. Overall, current state of the art experiments have not so far reached spatial as well as temporal atomic resolution and control of realistic liquid water/solid interfaces.

On the other hand, computational techniques have reached such a state of maturity that realistic liquid water/solid interfaces can be studied routinely using atomistic simulations. Atomistic simulations have demonstrated to be most useful for the explanation of experimental results [15], or to understand processes occurring under extreme conditions of temperature and pressure, such as in the middle "ice layers" of giant planets [16]. However, we are slowly experiencing a shift: increasingly atomistic modelling is being used for materials design, or to predict the phases of existing materials or even to discover entirely new materials. For instance, atomistic simulations have been used to identify hundreds of thousands of zeolites structures to improve the efficiency of carbon dioxide capture and storage [17].

Electronic structure methods, especially those based on density functional theory (DFT) simulations, are increasingly being used for the design of catalysts, for *e.g.* the formation of methane from CO, or to prevent fuel cell poisoning from CO oxidation (see Ref. [18] for a review). DFT simulations are especially suitable to predict catalytic properties of materials and design more efficient and cheaper catalysts for gas-phase reactions. However, in many important electrochemical processes surfaces are in contact with a liquid phase. Reactions and processes at liquid/solid interfaces pose additional challenges compared to gas-phase [18].

Electronic structure methods based on DFT have been used to address a number of important problems related to water on solid surfaces. These include: i) What is the nature of the bonding and the adsorption structure of water on a given surface under ideal UHV conditions and at 0 K? ii) How do different conditions of temperature and pressure affect the structure and dynamics of water on surfaces? iii) How does the presence of surface defects alter the stability of water on surfaces? These are some of the questions which are important to improve our current understanding of water/solid interfaces, and are therefore key to *e.g.* the design of better catalysts under wet conditions or to improve the efficiency of nano-membranes used for desalination or power harvesting. These are also some of the typical questions that we answer to in this thesis using DFT.

Although in principle DFT is exact, approximations have to be made to practically solve the electronic structure problem. The most crucial approximation is that of the exchange-correlation functional, where all the complex quantum mechanical phenomena of the many-particle problem are hidden. The particular approximations of the exchange-correlation functional can have a dramatic impact on the accuracy of DFT to predict the structure and dynamics of water/solid interfaces. Two of the most important issues of standard exchange-correlation functionals are the presence self-interaction error, and the lack of van der Waals dispersion interactions [19]. In order to perform state-of-the-art DFT calculations of water/solid interfaces, it is important to address both these issues and we do so throughout this thesis. The model used to describe water/solid interfaces can be of critical importance for the accuracy of the results. It is important to ensure that the properties

of interest are converged with the model used to describe the interface. Again this issue is also addressed throughout in this study.

In this thesis we investigate a range of water/solid interfaces that pose a number of scientific and technological challenges. Specifically, we use DFT-based methods to provide guidelines on how to solve important problems relating to heterogeneous catalysis and power harvesting. The systems investigated include water at the interface with TiO_2 and with ZnO – two of the most important metal oxides in photocatalysis [4] and heterogeneous catalysis [20] – and graphene and hexagonal boron nitride, which offer promising alternatives to power harvesting using salinity concentration gradients (so-called "blue energy") [21], and to conventional desalination membranes [22].

After a brief introduction to DFT and to *ab initio* molecular dynamics (AIMD) in Chapter 2, results on the structure of the clean and water covered ZnO$(10\bar{1}0)$ surface will be shown in Chapter 3. According to state-of-the-art DFT calculations at different levels of theory, a fraction of water is dissociated on the surface under ideal UHV-like conditions. This will pave the way for the study of proton transfer on ZnO$(10\bar{1}0)$ under aqueous conditions in Chapter 4. By comparing the proton dynamics of water on ZnO$(10\bar{1}0)$ under UHV-like conditions with that under aqueous conditions it is found that proton transfer is dramatically enhanced when ZnO$(10\bar{1}0)$ is in contact with liquid water. This can have important implications for ZnO-based catalytic reactions, such as for the formation of methanol [20].

An astounding achievement of nanotechnology is the capability to manufacture carbon and other inorganic nano-sized membranes, which are prom-

ising for their use in water desalination, energy conversion and as supercapacitors [21–25]. In these applications liquid/solid friction is one of the main sources of dissipation. In Chapter 5 the friction coefficient between liquid water and graphene is compared with that between liquid water and an hexagonal boron nitride sheet. AIMD simulations consistently reveal an increased friction on boron nitride compared to graphene, although the liquid film structure is almost indistinguishable between the two. In this study it is demonstrated for the first time that AIMD can be used to compute transport properties at liquid/solid interfaces, and that friction is a complex property not directly related to the structure and wetting of the substrate. Guidelines are also provided on how to manipulate liquid water/solid friction at the nanoscale.

Finally, in Chapter 6 results are presented for the structure of *the* model photocatalytic interface: water on rutile TiO_2(110). An extensive series of simulations using "flavours" of DFT that correct one of its most encumbering problems have been performed to interpret new surface X-ray diffraction (SXRD) results from Geoff Thornton's group at UCL on the adsorption of water on TiO_2(110) [26]. Particularly important in this study is the role of point defects and inner surface relaxation to water dissociation and adsorption of OH species. DFT simulations beyond the standard approximations have provided insights into the structure obtained from SXRD. This has allowed us to make sound statements on ways to alter the OH concentration on the surface, which is of utmost importance to the photocatalytic activity of TiO_2(110).

Chapter 2

Theoretical background

Summary

Quantum mechanics and statistical mechanics lay the foundations for our understanding of the properties of matter. In this chapter we first review the fundamental definitions of the many-body Hamiltonian of electrons and nuclei in condensed matter. This leads naturally to the introduction of density functional theory, one of the most popular methods for the solution of the many-body problem. We will then discuss *ab initio* molecular dynamics as a method stemming from electronic structure theory and statistical mechanics to efficiently sample phase space and that we will use throughout our study of liquid/solid interfaces.

2.1 Many-body problem of interacting electrons and nuclei

The Hamiltonian for a system of interacting electrons and nuclei is at the root of the electronic structure problem. If we adopt Hartree atomic units $\hbar = m_e = e = 1/4\pi\epsilon_0 = 1$, the Hamiltonian $\hat{H}$ can be written as:

$$\begin{aligned}\hat{H} = &-\frac{1}{2}\sum_i \nabla_i^2 - \sum_{i,I}\frac{Z_I}{|\mathbf{r}_i - \mathbf{R}_I|} + \frac{1}{2}\sum_{i\neq j}\frac{1}{|\mathbf{r}_i - \mathbf{r}_j|} \\ &- \frac{1}{2M_I}\sum_I \nabla_I^2 + \frac{1}{2}\sum_{I\neq J}\frac{Z_I Z_J}{|\mathbf{R}_I - \mathbf{R}_J|} \qquad (2.1)\\ = &\hat{T}_e + \hat{V}_{n-e} + \hat{V}_{e-e} + \hat{T}_n + \hat{V}_{n-n}\,, \qquad (2.2)\end{aligned}$$

where lower case subscripts refer to the electrons, and upper case subscripts refer to nuclei with charge Z and mass M. In eq. 2.2 the Hamiltonian has been rewritten in a more compact way, where $\hat{T}_e$ is the kinetic energy the electrons, $\hat{V}_{n-e}$ is the potential acting on the electrons due to the nuclei, $\hat{V}_{e-e}$ is the electron-electron interaction and $\hat{V}_{n-n}$ is the interaction between the nuclei. The significant velocity of the electrons (the Fermi velocity) is $\approx 10^8$ cm/s, and much larger than the ionic velocity, around 10^5 cm/s, such that one can assume that at any instant of time the electrons are at their ground state for that particular ionic configuration [27]. This is the Born–Oppenheimer approximation, which is an excellent approximation in most cases, *e.g.* for the calculation of the phonon dispersion of a crystal [28]. The Born–Oppenheimer approximation represents also a starting point for the description of more complex phenomena where electrons and phonons are

coupled. Typical examples are electron transport in metals and superconductivity, which can be treated for instance using perturbation theory [28, 29].

Within the Born–Oppenheimer approximation the time-independent solution of the Hamiltonian in eq. 2.1 is obtained by solving the many-body Schrödinger equation, which is written as:

$$\hat{H}\,|\Psi\rangle = (\hat{T}_e + \hat{V}_{n-e} + \hat{V}_{e-e} + \hat{V}_{n-n})\,|\Psi\rangle = E\,|\Psi\rangle \tag{2.3}$$

where $|\Psi\rangle$ is the eigenstate of the Hamiltonian and it represents the many-body wavefunction which depends on the $3N$ electronic coordinates $\mathbf{r}_i$, *i.e.* $\Psi(\mathbf{r}_1, \mathbf{r}_2, \ldots, \mathbf{r}_N)$. Solution of eq. 2.3 gives a set of eigenfunctions and eigenvalues, E, the total energy. The lowest of the eigenvalues is the ground state energy E_0, from which all ground-state properties can be obtained. These include the cohesive energies of solids, their equilibrium crystal structure and the phase transition between different structures, the nuclear motion, *etc.*. Even excited state properties such as the optical absorption spectra or the phonon spectra can be obtained from a perturbation of the ground state properties [27–29].

The exact solution to eq. 2.3 is limited to a few very small systems, notably, the H atom, H_2^+, and perturbatively the He atom. Another important system in solid state physics for which an exact solution exists is the homogeneous electron gas [30], which is a model of interacting electrons in a uniform positively charged background.

The number of electrons in condensed phase systems is of the order of 10^{23}, which makes it impractical (to say the least) to solve eq. 2.3 exactly for a

real system. Fortunately, methods to obtain approximate solutions to eq. 2.3 have been developed (see *e.g.* Ref. [31] for a review). In the following section we provide an introduction to one of the most popular electronic structure methods: Kohn-Sham density functional theory.

2.2 Introduction to density functional theory

Kohn-Sham density functional theory (DFT) is the most widely used method for describing the electronic structure of materials [19]. The first and second Hohenberg-Kohn theorems lay the foundations of DFT [32]. However, not until the formulation of Kohn and Sham did DFT become a consistent and practical method to solve the many body problem [33].

2.2.1 The foundations of DFT

The first Hohenberg-Kohn theorem states that in a system of interacting electrons in the presence of an external potential $v_{ext}(\mathbf{r})$, the potential $v_{ext}(\mathbf{r})$ is determined uniquely by the ground state electron density $n_0(\mathbf{r})$, except for a constant shift in the energy. Therefore, the ground state electron wave function $\Psi_0(\mathbf{r}_1, \mathbf{r}_2, \ldots, \mathbf{r}_N)$ can be obtained simply by knowing the ground state density $n_0(\mathbf{r})$. Accordingly, any ground state property of a material can be obtained from the density. From this follows the second Hohenberg-Kohn theorem, which states that there exists a *universal* functional of the electron density ($F[n(\mathbf{r})]$) for any given external potential $v_{ext}(\mathbf{r})$ [28]. For any external potential the ground state energy E_0 can be obtained from the

minimization of this functional at the ground state density $n_0(\mathbf{r})$, namely:

$$E_0 = E[n_0(\mathbf{r})] \leq E[n(\mathbf{r})]. \tag{2.4}$$

Together the first and second Hohenberg-Kohn theorems attempt to find a solution to the complicated many-body problem in terms of $n(\mathbf{r})$ alone instead of the much more complicated many-body wave function that depends on $3N$ degrees of freedom.

Unfortunately, stating that a universal functional of the electron density exists does not mean that it is known. In fact, accurate ways to express the kinetic energy in eq. 2.3 only in terms of the density exist only for simple metals and alloys [34].

2.2.2 The Kohn-Sham ansatz

A more successful approach to solve the many-body problem has been introduced by Kohn and Sham [33]. The main idea of Kohn and Sham was to reformulate the electron kinetic energy and the electron-electron interaction of the interacting electron system in terms of a non-interacting one. All the complexity arising from the quantum mechanical many-body interactions is then reintroduced into a term called the exchange-correlation functional, $E_{\mathrm{xc}}[n(\mathbf{r})]$.

Following the Kohn-Sham ansatz, the Hamiltonian in eq. 2.3 can be rewritten in terms of a system of non-interacting particles, using a so-called single-particle approach. The electron density can therefore be represented by the electron density of a system of non-interacting particles. $n(\mathbf{r})$ itself

is obtained as the sum of the squares of the non-interacting orbitals ψ_i^σ for each spin σ:

$$n(\mathbf{r}) = \sum_\sigma n(\mathbf{r}, \sigma) = \sum_\sigma \sum_{i=1}^{N^\sigma} |\psi_i^\sigma(\mathbf{r})|^2 \,. \tag{2.5}$$

In Kohn-Sham theory the expectation value of the kinetic energy for the interacting system appearing $\langle \hat{T}_e \rangle$ (see eq. 2.3) is approximated with the single-particle kinetic energy T_s, given by:

$$T_s[n(\mathbf{r})] = \frac{1}{2} \sum_\sigma \sum_{i=1}^{N^\sigma} \int \mathrm{d}^3 r \, |\nabla \psi_i^\sigma(\mathbf{r})|^2 \,. \tag{2.6}$$

Analogously, the mean electron-electron interaction $\langle V_{e-e} \rangle$ is approximated with the single-particle energy for the electron-electron interaction, which is just the Coulomb interaction energy for the self-interacting density (*i.e.* the Hartree energy):

$$E_{\mathrm{Hartree}}[n(\mathbf{r})] = \frac{1}{2} \int \mathrm{d}^3 r \, \mathrm{d}^3 r' \, \frac{n(\mathbf{r}) n(\mathbf{r}')}{|\mathbf{r} - \mathbf{r}'|} \,, \tag{2.7}$$

By approximating $\langle \hat{T} \rangle$ with T_s and $\langle V_{e-e} \rangle$ with E_{Hartree}, all the many-body interactions are neglected. These are put into the exchange-correlation energy E_{xc}, which is at the heart of Kohn-Sham DFT and defined as

$$E_{\mathrm{xc}}[n(\mathbf{r})] = \langle \hat{T} \rangle - T_s[n(\mathbf{r})] + \langle V_{e-e} \rangle - E_{\mathrm{Hartree}}[n(\mathbf{r})] \,. \tag{2.8}$$

The Kohn-Sham total energy functional altogether reads:

$$E_{\mathrm{KS}}[n(\mathbf{r})] = T_s[n(\mathbf{r})] + \int \mathrm{d}^3r\, v_{ext}(\mathbf{r})n(\mathbf{r}) + E_{\mathrm{Hartree}}[n(\mathbf{r})] + E_{\mathrm{xc}}[n(\mathbf{r})] + E_{II}\,, \tag{2.9}$$

where the integral of the external potential $v_{ext}(\mathbf{r})$ refers at minimum to the potential acting on the electrons due to the nuclei and E_{II} is the energy due to the interaction between the nuclei (see eq. 2.2). Using variational calculus eq. 2.9 can be minimized, yielding the set of Kohn-Sham equations:

$$\left(-\frac{1}{2}\nabla^2 + v^{\sigma}_{\mathrm{KS}}(\mathbf{r})\right)\psi^{\sigma}_i(\mathbf{r}) = \epsilon^{\sigma}_i\psi^{\sigma}_i(\mathbf{r}) \quad i = 1, 2, \ldots N\,, \tag{2.10}$$

$$v^{\sigma}_{\mathrm{KS}} = v_{ext}(\mathbf{r}) + \int \mathrm{d}^3r\, \frac{n(\mathbf{r}')}{|\mathbf{r}-\mathbf{r}'|} + \frac{\delta E_{\mathrm{xc}}}{\delta n(\mathbf{r},\sigma)}\,, \tag{2.11}$$

where ϵ^{σ}_i are the eigenvalues of eq. 2.10. The theory is now complete. Altogether, eq. 2.5 and eq. 2.10 allow to solve the electronic structure problem.

In Kohn-Sham theory the electrons are viewed as independent particles, moving under the effective potential v_{KS} [19]. In this picture, however, the dependence on $\psi^{\sigma}_{i=1,2,\ldots N}(\mathbf{r})$ has been introduced. This is not the many body wavefunction $\Psi(\mathbf{r}_1, \mathbf{r}_2, \ldots, \mathbf{r}_N)$ but a set of fictitious single-particle orbitals. The introduction of the single-particle orbitals means that N eigenvalue problems given by eqs. 2.10 have to be solved. Obviously, the dependence on $3N$ degrees of freedom from a computational point of view is not as appealing as only on 3, as in the original formulation of Hohenberg and Kohn. However,

this is one of the prices to pay for the simplicity of Kohn-Sham DFT.

2.2.3 Exchange-correlation functionals

Another problem is that no explicit expression is known for the exchange correlation functional E_{xc}. Although Kohn-Sham DFT is exact, approximations have to be made for the exchange-correlation functional. The simplest of these is the local density approximation (LDA):

$$E_{xc-LDA}[n(\mathbf{r})] = \int \mathrm{d}^3 r \, n(\mathbf{r}) \epsilon_{xc-heg}(n(\mathbf{r})) \,. \tag{2.12}$$

Within the LDA the exchange-correlation energy density $\epsilon_{xc-heg}(n(\mathbf{r}))$ is approximated with that of the homogeneous electron gas evaluated locally (i.e. at each point in space) at a given density. The exchange energy density is known exactly for the homogeneous electron gas from Hartree-Fock theory and the correlation energy has been calculated by fitting to very accurate quantum Monte Carlo methods [35]. The LDA works well in cases of a slowly varying density $n(\mathbf{r})$, and it is seen to be a reasonable start in the calculation of solids, atoms and molecules [19, 36]. However, it generally overbinds atomization energies of atoms and molecules too much. For instance, the mean error for atomization energies with respect to a test set containing experimental data with better than 1 kcal/mol precision (the so-called "chemical accuracy") is about 3.5 eV/atom with the LDA [19].

The generalized gradient approximation (GGA) is more sophisticated. Now the exchange-correlation energy density depends also on the gradient of the electron density, *i.e.* $\epsilon_{xc-heg}(n(\mathbf{r}), \nabla n(\mathbf{r}))$. Popular functionals within the

GGA are *e.g.* PW91 [37], PBE [38] and BLYP [39, 40]. Although GGAs have shown an overall improvement over the LDA on the ground state properties of solids, atomization energies of atoms and molecules, it is thought that some properties are better described with the LDA. One important example is the surface energy of solids [41–43]. More advanced formulations to express the exchange correlation functional involve expansions to higher order derivatives of the density, as e.g. the meta-GGA which uses the laplacian of the density.

2.2.4 Beyond standard density functionals

Even though many properties of solids, surfaces, and interfaces can be captured using standard density functionals within the LDA or the GGA, there are some outstanding failures of standard functionals. These are notably the lack of dispersion forces, and the inability to provide good estimates of the band-gap of semiconductors and insulators.

Dispersion is a fully non-local interaction, part of van der Waals interactions. It can be defined as the electron density response to instantaneous density fluctuations in other regions of space. Dispersion gives rise to the well-known attractive dipole dipole-induced interaction, which scales as $-1/r^6$ for large interatomic separations r. There exists a wide variety of methods to account for dispersion within DFT (see Ref. [44] for a review). A class of very popular methods involves the calculation of the dispersion energy from the pairwise sum of a $-C_6/r^6$ term, where C_6 is the dispersion coefficient [45–49]. Each of these schemes differs in the way the C_6 coefficients for the pair of atoms are computed and on how the divergence at low separation is treated.

Another class of dispersion corrections is based on the calculation of the

dispersion interaction energy directly from the density and for this reason they are usually called van der Waals density functionals [50–53]. The basic idea of these methods is that the dispersion contribution to the total energy functional is obtained by the non local correlation energy E_c^{nl} defined as:

$$E_c^{nl} = \int \mathrm{d}^3 r_1 \, \mathrm{d}^3 r_2 \, n(\mathbf{r_1}) \varphi(\mathbf{r_1}, \mathbf{r_2}) n(\mathbf{r_2}) \,, \tag{2.13}$$

where $n(\mathbf{r_1})$ and $n(\mathbf{r_2})$ are the electronic densities at coordinates $\mathbf{r_1}$ and $\mathbf{r_2}$ and $\varphi(\mathbf{r_1}, \mathbf{r_2})$ is an integration kernel that depends on the separation $\mathbf{r_1} - \mathbf{r_2}$ with the correct asymptotic behaviour $-1/|\mathbf{r_1} - \mathbf{r_2}|^6$ for large separations. The different van der Waals density functionals differ in the way the E_c^{nl} is calculated or in the way it is incorporated into the overall expression for the total energy (see *e.g.* Ref. [44]). The correction of the van der Waals density functionals is still pairwise, although they generally show an improvement in the accuracy over the $-C_6/r^6$ empirical correction.

Corrections beyond the pairwise sums and that account for the fact that the interactions between two electrons is screened by the presence of all the other electrons generally require the calculations of more complicated and more expensive expressions. One of the most popular approaches makes use of the adiabatic connection fluctuation dissipation theorem [54, 55], within the random phase approximation (RPA) [56, 57]. Although the RPA is at present one of the most accurate methods for the calculation of bulk properties in condensed phase systems [58, 59], this comes also to a great computational cost. Indeed, while the cost of traditional DFT methods and pairwise corrections scale with S^3 (where S is the system size), RPA-based methods

scale with S^4.

Besides dispersion corrections, methods that predict more accurate band structures in insulators or semiconductors have appeared already since quite some time (see *e.g.* Ref. [60]). The prediction of too small a band-gap in insulating materials is due to an error present in standard density functional approximations that is commonly referred to as self-interaction. Self-interaction is caused – in non-Hartree Fock based methods – by the incomplete cancellation between the Hartree energy of one electron interacting with itself and the exchange energy of the same electron interacting with itself. The calculation of band-gaps which are too small means that *e.g.* ground state properties of insulators in the presence of point defects are generally not sufficiently accurate. Perdew and Zunger first introduced a self-interaction correction by adding a self-Coulomb term and a self-exchange-correlation term to the total energy [60]. Also the DFT+U method can be used to correct for self-interaction, where the additive Hubbard-U term penalizes an excessive delocalization of the orbitals and "pushes" the orbitals towards being either fully occupied or fully unoccupied [61].

Further, the use of a certain fraction of exact exchange can correct for the self-interaction error (see *e.g.* Ref. [62]). This is the approach followed when using hybrid functionals. Popular hybrid functionals such as B3LYP [63, 64] and PBE0 [65] (and its short range version HSE06 [66]) have shown to generally improve the band-gap in semiconductors and insulators. However, the calculation of exact exchange scales like S^4 and it comes at a greater cost than standard functionals. RPA and other higher order methods like GW

also improve the description of band-gaps, and we point the interested reader to Refs. [28, 62, 67].

2.3 Solving the Kohn-Sham equations

The Kohn-Sham equations 2.5 and 2.10 form a complete set that allow to solve the electronic structure problem. The procedure to solve the equations 2.5 and 2.10 involves the following steps:

1. Guess the initial density $n^{(0)}(\mathbf{r})$ at each point in space;

2. Solve the set of N independent (single-particle) eigenvalue problems given by eq. 2.10;

3. Recompute density $n^{(1)}(\mathbf{r})$ using eq. 2.5 from the orbitals obtained from eq. 2.10;

4. If $|n^{(1)}(\mathbf{r}) - n^{(0)}(\mathbf{r})| < \text{tolerance}$, then stop, otherwise update density and start back from step 2.

Eqs. 2.10 and 2.5 have to be solved together until a solution is found iteratively, which means that the density and the Kohn-Sham potential have to be consistent. From this the name self-consistent loop is given to the algorithm just described.

2.3.1 Basis sets

To solve eq. 2.10 a set of N eigenvalue problems have to be solved for each

orbital $\psi_i(\mathbf{r})$, which have to be expanded in a given basis set $\phi(\boldsymbol{r})$:

$$\psi_i(\mathbf{r}) = \sum_{p=1}^{P} c_{i,p}\phi_p(\mathbf{r})\,, \tag{2.14}$$

where $c_{i,p}$ are the expansion coefficients and in principle $P \to \infty$, for $\psi_i(\mathbf{r})$ to be a complete basis set. In practice, we work with a finite number of basis functions and we stop at a number of P which is large enough to give properties converged to the desired accuracy. There exists a large number of basis sets which generally fall into two main groups: i) atom centered and ii) non-atom centered basis sets.

Among the different types of atom centered basis functions, Gaussian type orbitals are among the most popular because the calculations of several integrals and derivatives may be performed analytically. One of their main drawbacks, however, is that they cannot represent the proper behaviour near the nuclei, where the orbitals should have a "cusp", instead of being flat. Also, the accuracy of DFT calculations with localized basis functions depends critically on the size of the basis set. Basis-set incompleteness gives rise to the so-called basis set superposition error, which manifests itself in *e.g.* the calculation of the binding energy of dimers. In the calculation of the binding energy, each monomer is effectively described by a larger basis in the composite dimer than in the monomer, which gives rise to a non-physical increase in the binding. Methods like the counterpoise correction exist to correct for this error [31].

Among DFT codes that employ non-atom centered basis functions, those that use plane waves are very popular because the evaluation of integrals

makes large use of fast Fourier transforms and it is simple and efficient. Plane waves DFT codes usually employ periodic boundary conditions because they exploit the Bloch's Theorem [27]. The expansion in plane waves comes naturally from Bloch's Theorem, which states that the eigenfunctions of a Hamiltonian in a periodic potential are given by plane waves modulated by functions which have the same periodicity of the lattice. Using Bloch's Theorem the plane wave basis set expansion reads:

$$\psi_{n\mathbf{k}}(\mathbf{r}) = u_{n\mathbf{k}}(\mathbf{r})\, e^{i(\mathbf{k}\cdot\mathbf{r})}\,, \tag{2.15}$$

where $\mathbf{k}$ is a reciprocal vector within the first Brillouin zone and the function $u_{n\mathbf{k}}(\mathbf{r})$ has the periodicity of the lattice, *i.e.* $u_{n\mathbf{k}}(\mathbf{r}) = u_{n\mathbf{k}}(\mathbf{r}+\mathbf{R})$, for any translation vector $\mathbf{R}$ in the Bravais lattice. In eq. 2.15 the subscript n is denoted as band index and refers to the number of independent eigenvalues for each value of $\mathbf{k}$. Thanks to Bloch Theorem the wave vector $\mathbf{k}$ can always be translated back to the first Brillouin zone, and the eigenvalues are also periodic functions in the reciprocal space, *i.e.* $\epsilon_{n,\mathbf{k}+\mathbf{K}} = \epsilon_{n\mathbf{k}}$. This means that it is possible to perform plane wave DFT calculations using only the primitive unit cell, instead of a larger "supercell". The only problem is that we have to sample $\mathbf{k}$-space, which means that we have to solve the Kohn-Sham equations for a discrete set of k-points. The number of k-points is usually increased until the property of interest is converged.

Although plane wave and Gaussian basis functions are among the most popular, there is a growing demand for DFT codes that can treat efficiently systems of several thousands of atoms. For instance, this has led to the

development of codes that try to exploit the advantages of both methods, using the so-called Gaussian plane wave method (GPW) [68]. Using the GPW approach all integrals and derivatives in the Kohn-Sham equations are computed using Gaussian basis functions, except for the integral of the Hartree and of the exchange-correlation term, where auxiliary plane waves are used. Using this approach sub-linear scaling has been obtained, allowing calculations for systems containing several hundreds to thousands of atoms to be performed routinely on large enough parallel machines [69].

2.3.2 Treating the core electrons

It is important to treat the core electrons even if they are not involved in the bonding, otherwise the valence orbitals are not properly described due to a poor description of electron-electron interactions. However, near the nuclei the wavefunction has very many nodes and rapid oscillations due to the strong Coulomb potential of the core electrons. Especially in plane waves codes it is not efficient to describe the core electrons by simply using the basis set expansion as in eq. 2.14, *i.e.* using an all-electron basis set. One needs simply too many basis functions to treat correctly the rapid oscillations of the core electrons near the nuclei.

A possible way to treat the core electrons is to use pseudopotentials. In the pseudopotential method, the effects of the core electrons are replaced by an effective potential acting on the orbitals of the valence electrons. In this way the core electrons are effectively eliminated, thus reducing the cost of the calculation. Also, the valence orbitals are replaced with pseudo-orbitals, which have usually analytical forms. Within a cut-off radius r_c from the

nuclei, the pseudo-orbitals are much smoother than the reference orbitals. Then, at a distance $r \geq r_c$, the pseudo-orbitals match with reference orbitals. The pseudopotentials are usually divided in norm-conserving and ultra-soft types. As the name suggests, the norm-conserving pseudopotentials require the integral of the square modulus of the pseudo-orbital to be the same as that of the reference orbital. On the other hand, with ultra-soft pseudopotentials this constraint is relaxed and they are usually smoother and require a cut-off radius not as small as the norm-conserving ones [70].

Another popular method to treat the core electrons is the projector augmented wave (PAW) method [71]. The basic idea is to represent the all-electron wavefunction $|\psi\rangle$ with a smooth pseudo-wavefunction $|\tilde{\psi}\rangle$, which can be done by applying the linear operator $\hat{\mathrm{T}}$ to $|\tilde{\psi}\rangle$, that is $|\psi\rangle = \hat{\mathrm{T}}\,|\tilde{\psi}\rangle$. The operator takes the form $\hat{\mathrm{T}} = \mathbf{1} + \sum_m (|\psi_m\rangle - |\tilde{\psi}_m\rangle)\,\langle\tilde{p}_m|$, where the sum over m "partial waves" runs over the core region only and the $\langle\tilde{p}_m|$ is a projector function that corrects for the difference within the region of the nuclei between $|\tilde{\psi}\rangle$ and $|\psi\rangle$. It can be seen from the expression for the operator $\hat{\mathrm{T}}$ that the all-electron wavefunction $|\psi\rangle$ has to be obtained over the core region. This can be done on radial grids using analytical Bessel functions. Although the PAW method retains the core-electrons, they do not usually change during the calculations, using the so called "frozen-core" approximation.

2.4 *Ab initio* Molecular Dynamics

The development of efficient algorithms and electronic structure codes and of increasingly faster and bigger parallel machines has led to a revolution in

computational materials science: the possibility to treat the thermal motion of real systems including solids, liquids and solid/liquid interfaces using *ab initio* molecular dynamics [28].

The pioneers of *ab initio* molecular dynamics were Car and Parrinello [72]. In the Car-Parrinello method, both the ions and the electrons are evolved in time. Additional degrees of freedom are associated to the electronic motion to describe the fictitious electron dynamics. Using this approach the self-consistent loop expressed by eq. 2.5 and 2.10 has to be solved only once and then the ions and electrons can be evolved in time by integrating Newton's equations of motion. The use of Car-Parrinello molecular dynamics has opened the way for electronic structure methods to investigate an entire range of problems far beyond previous capabilities. These include the structure of liquid water and its infrared spectrum entirely from first principles [73, 74]. Examples on perhaps even more complex systems are the investigation of equilibrium properties of glucose in aqueous solution [75] and of several phases of carbon at high pressures and temperatures [76].

Although Car-Parrinello molecular dynamics has represented an enormous step forward in the computation of materials, the trajectories might deviate from the Born-Oppenheimer potential energy surface, with evident problems in sampling effectively phase space. Also it is not straightforward to choose an appropriate fictitious electron mass, and the time step must be sufficiently small to account for the fast oscillations of the fictitious electron degrees of freedom (which are much greater than the frequencies of the nuclei).

An alternative approach is to perform *ab initio* molecular dynamics within the Born-Oppenheimer approximation (here simply AIMD). The idea of AIMD is simple: to compute the total energy and forces at each time step by solving the self-consistent loop and integrate Newton's equations of motion to obtain the trajectory of the ions. The development of ever more efficient algorithms to solve the Kohn-Sham equations and to extrapolate the ground state wavefunction at each time step (see *e.g.* Refs. [77, 78]) has made the efficiency of AIMD within the Born-Oppenheimer approximation comparable with the scheme proposed by Car and Parrinello. Within the Born-Oppenheimer approximation and treating the nuclei as classical point-like particles Newton's second law reads:

$$M_I \ddot{\mathbf{R}}_I = -\frac{\partial E}{\partial \mathbf{R}_I} = \mathbf{F}_I[\{\mathbf{R}_J\}]\,. \tag{2.16}$$

Within Kohn-Sham DFT it is straightforward to compute the forces on the nuclei $\mathbf{F}_I[\{\mathbf{R}_J\}]$ thanks to the Hellmann-Feynman theorem which can be viewed as a consequence of DFT being based on the variational principle. From eq 2.9 for the Kohn-Sham total energy, the force equation using Hellmann-Feynman theorem is expressed as:

$$-\frac{\partial E}{\partial \mathbf{R}_I} = -\left\langle \psi \right| \frac{\partial \hat{H}}{\partial \mathbf{R}_I} \left| \psi \right\rangle - \frac{\partial E_{II}}{\partial \mathbf{R}_I} = -\int \mathrm{d}^3 n(\mathbf{r}) \frac{\partial v_{ext}(\mathbf{r})}{\partial \mathbf{R}_I} - \frac{\partial E_{II}}{\partial \mathbf{R}_I}\,. \tag{2.17}$$

The right hand side of eq. 2.17 illustrates that it is relatively simple to obtain the forces within DFT, and the time integration using standard schemes like *e.g.* the Verlet algorithm is even less computationally demanding. From this

it is clear that the bottleneck of any AIMD simulation is represented by the calculation of the self-consistent loop.

2.4.1 AIMD in the canonical ensemble

Given a set of initial conditions (*i.e.* ionic coordinates and velocities), the equations of motions can be integrated to perform an AIMD simulation in the microcanonical ensemble, that is where the number of particles, the volume and the total energy are conserved (NVE). Assuming that the simulation is so long that all the regions of phase space at constant energy are explored, a microcanonical distribution is generated and the time average of any quantity equals its phase space average. This is the ergodic hypothesis, which is a rather strong one especially in AIMD, where one is limited to trajectories usually not longer than several tens of picosecond. Although especially in systems with many degrees of freedom it is hard to prove (or disprove) ergodicity, it is clear that the hypothesis will not hold in cases where there are too high potential barriers, *i.e.* if there is a region of space where the potential $v_{ext}(\mathbf{r}) > E$.

Apart from the ergodicity problem, performing AIMD in the microcanonical ensemble poses the problem that usually experimental conditions are not under constant energy. An ensemble that more closely resembles common experimental set-ups is the one where N, V and the temperature T are conserved, *i.e.* the canonical ensemble. Although in the thermodynamic limit ($N \to \infty$) the canonical and the microcanonical ensembles are equivalent, most simulations are performed far away from this limit. Away from the thermodynamic limit energy fluctuations are not negligible and have to be

accounted for. Energy fluctuations are generated by a system in contact with an external bath. Methods to account for the energy fluctuations to give a constant temperature are called for an obvious reason thermostats, and have been around since the 80s (see *e.g.* Ref. [79] for a review).

Here, we introduce the Nosé-Hoover chains thermostat, which is one of the most popular schemes [80]. As opposed to *e.g.* the standard Nosé-Hoover thermostat [81, 82], the Nosé-Hoover chains thermostat has been shown to generate a canonical distribution for the positions and momenta even for the most pathological model systems [80]. With the Nosé-Hoover chains thermostat a number of fictitious equations of motion are added to control the temperature and rescale the ionic velocities according to the target temperature. There is a number of equations of motions N_c (chains) coupled together, which rescale the ionic velocities according to the desired temperature, thus mimicking the effect of the thermal bath. If we denote the actual momentum for the ions as $\mathbf{p}_I$, the fictitious momentum as p_η and the associated variable η, we can rewrite the equations of motion 2.16, now in the presence of the thermostat as:

$$
\begin{aligned}
\dot{\mathbf{R}}_I &= \frac{\mathbf{p}_I}{M_I} \\
\dot{\mathbf{p}}_I &= \mathbf{F}_I - \frac{p_{\eta_1}}{Q_1}\mathbf{p}_I \\
\dot{\eta} &= \frac{p_{\eta_j}}{Q_j} \qquad j = 1, \ldots, N_c \\
\dot{p}_{\eta_1} &= \left[\sum_{I=1}^{N} \frac{\mathbf{p}_I^2}{M_I} - dNkT\right] - \frac{p_{\eta_2}}{Q_2} p_{\eta_1} \\
\dot{p}_{\eta_j} &= \left[\frac{p_{\eta_{j-1}}^2}{Q_{j-1}} - kT\right] - \frac{p_{\eta_{j-1}}}{Q_{j+1}} p_{\eta_j} \qquad j = 2, \ldots, N_c - 1 \\
\dot{p}_{\eta_{N_c}} &= \left[\frac{p_{\eta_{N_c-1}}^2}{Q_{N_c-1}} - kT\right] .
\end{aligned} \tag{2.18}
$$

It can be seen that in Newton's equation for $\dot{\mathbf{p}}_I$ a new term appears $(p_{\eta_1}/Q_1)\mathbf{p}_I$, which in turn depends on another "chain" of $N_c - 1$ equations. The term Q_j is a parameter that sets the time scale over which the velocities are rescaled. The presence of N_c chains ensures the sampling of a canonical distribution [80].

We conclude this section by mentioning that equilibrium transport properties, obtained from *e.g.* linear response theory (such as the friction coefficient computed in Chapter 5), may not be properly described. While ensuring the sampling of the canonical distribution, the use of a thermostat such as Nosé-Hoover chains might yield a fictitious dynamics. Tests on the calculation of dynamical properties under the NVE ensemble are therefore needed. In the case that equilibrium transport properties are computed in the NVE ensemble, the underlying assumption is that the system is large enough that

the NVT and the NVE are equivalent and the temperature fluctuations are therefore negligible (they scale as $1/\sqrt{N_p}$, where N_p is the number of particles). It is possible to test the validity of this assumption by checking the convergence of the desired transport properties using cells of increasing system size.

Other ways of computing dynamical properties involve the use of non-equilibrium molecular dynamics. In this case the system is effectively perturbed and the response to the perturbation measured, in pretty much the same way as in experiments (see Ref. [83] for an example on the calculation of the friction coefficient). Using this approach the assumption of the thermodynamic limit is relaxed. Nevertheless, non-equilibrium molecular dynamics simulations are significantly more challenging, especially because they require a much longer simulation time for the calculation of converged dynamical properties.

Chapter 3

Structure of clean and water covered ZnO$(10\bar{1}0)$

3.1 Introduction

ZnO is a II-VI group semiconductor which has recently received a lot of attention in nanotechnology applications for electrical energy conversion from *e.g.* sunlight [84], ultrasonic waves [85] and mechanical energy [86]. ZnO plays also a major role in heterogeneous catalysis, where Cu nanoparticles deposited on ZnO surfaces are used for the synthesis of methanol, which is one of the most important products of the chemical industry nowadays [20, 87]. It is of great importance to characterize the electronic and structural properties of clean ZnO surfaces because surface properties have an increased influence on heterogeneous catalysis and on nano-devices, as opposed to those of the bulk.

3.1. INTRODUCTION

Being a II-VI semiconductor, ZnO presents interesting chemical bonding properties in that it exhibits a mixed covalent/ionic character. Under ambient conditions ZnO crystallizes in the wurtzite structure consisting of hexagonal Zn and O planes stacked in an alternate fashion, and where each cation is tetrahedrally coordinated to four neighbouring anions and vice versa. A tetrahedral structure is typical of group IV and III-V covalent semiconductors, like Si, diamond and GaAs, but interestingly the degree of ionicity is particularly pronounced in ZnO, which shows similarities with a prototypical ionic insulator like MgO [88].

Like other wurtzite crystals, ZnO exposes four main facets: the non-polar $(10\bar{1}0)$ and $(11\bar{2}0)$ orientations, and the polar (0001) and the $(000\bar{1})$ ones, which are Zn- and O-terminated, respectively. The $(10\bar{1}0)$ orientation is the most stable phase [87], and it has been the subject of many experimental investigations since the Low Energy Electron Diffraction (LEED) study of Lubinsky *et al.* [89–94]. Upon cleavage of the bulk crystal along the $(10\bar{1}0)$ plane, the surface structure looks like the one shown in Fig. 3.1. It forms an hexagonal bilayer structure made of ZnO dimers running along $[1\bar{2}10]$, with each dimer separated by trenches along $[000\bar{1}]$.

Although there are no reports documenting major reconstructions, the form and the degree of relaxation of the top surface atoms still remains controversial. Specifically, several LEED works reported an inward relaxation of the top Zn-atom of 0.45 Å, and essentially no displacement of the top O-atom (see *e.g.* Refs. [89–92]), and a resulting tilt of the top Zn–O bond with the anion above the cation. On the other hand, a very small relaxation of the

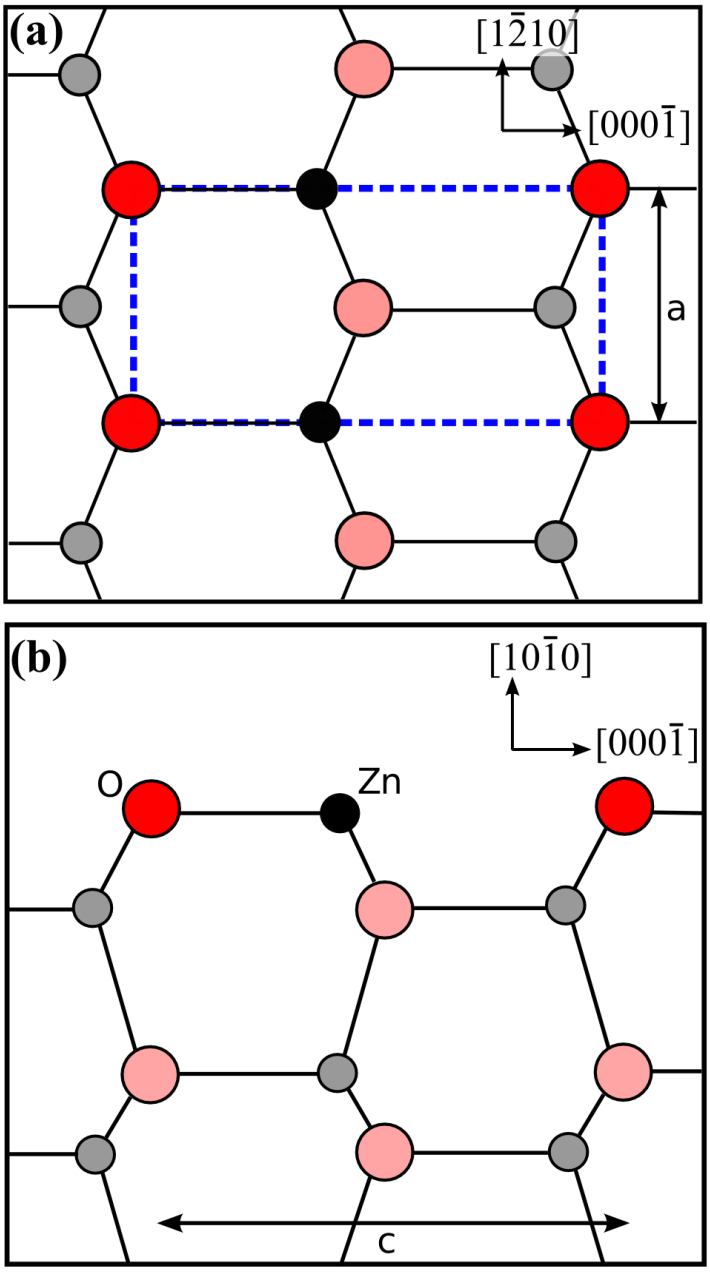

Figure 3.1: Illustration of the structure of ZnO(10$\bar{1}$0) in top (a) and side (b) views. Red and black circles are the O and Zn ions in the top layer, respectively. The pink and grey circles are O and Zn ions in the layers underneath. The surface unit cell is indicated by dashed lines.

Zn-atom toward the bulk of 0.06 ± 0.02 Å was found in a grazing incidence X-ray diffraction (GIXD) experiment of Jedrecy *et al.*, along with a larger relaxation of the O-atom toward the bulk of 0.12 ± 0.02 Å [93]. Accordingly, the surface would exhibit an opposite tilting to what shown in the other LEED studies with the anion below the cation.

The theoretical results on the details of the relaxation and of the tilting of the top Zn- and O-atoms are also scattered. The first *ab initio* Hartree-Fock or DFT-LDA studies on ZnO($10\bar{1}0$) obtained using Gaussian basis functions showed very small relaxations of about 0.1 Å of the top Zn and O atoms and a tilt of the Zn–O bond of about 2° [95, 96]. A more recent study using the B3LYP functional found similar results, although a slow convergence of the surface structure with the number of layers has also been reported [97]. Even though B3LYP, like other hybrid functionals, have shown improved description of bulk ZnO properties over LDA or other GGA based studies (see *e.g.* Refs. [98]), in Ref. [97] the ions have only been relaxed along the $[10\bar{1}0]$ direction, while they have not been relaxed within the $(10\bar{1}0)$ plane. This is not a sound procedure, as ZnO dimer has six degrees of freedom and the ions can move in all three directions. Other theoretical results from plane waves calculations and with the LDA or PBE exchange-correlation functionals found instead a converged structure using already 3 bilayer slabs and showed a larger tilt of $\approx 10°$ and a relaxation of the top Zn-atom between -0.3 and -0.4 Å with respect to bulk ZnO [88, 99].

Since the details of the relaxation are related to the ionic or covalent character of the surface, and this can for instance affect the activity of ZnO-

based catalysts, it is important to determine the extent of such relaxation. DFT has been extensively used to solve complex surface reconstruction and relaxation mechanisms in solid crystals (see *e.g.* Ref. [36]) and we will use it here to shed light on the details of the surface relaxation of ZnO($10\bar{1}0$). In the first part of this chapter, we will compare the performance of several exchange-correlation functionals for the description of the surface properties of clean ZnO($10\bar{1}0$). Specifically, we will show the results obtained from the PBE functional along with methods that partially correct for the self-interaction error of DFT, namely using a Hubbard-U correction [61] and the HSE06 hybrid functional [66].

In the second part of this Chapter we will focus on the adsorption of water on ZnO($10\bar{1}0$). Water is important in heterogeneous catalysis and in electrochemistry because many such processes occur under wet conditions and water may also participate during some steps of a reaction. In the case of ZnO, water is expected to play a role in the performance of nanowire dye-sensitized solar cells [84] and also in the synthesis of methanol because it is a side-product of the reverse water-gas shift reaction [20, 100]. For this reason there have been many experimental studies of water on well-defined ZnO surfaces, including experiments in-house in Geoff Thornton's group.

In any of such applications a major interest is whether or not water dissociates on a surface. Although water dissociation has been reported on many oxides (see *e.g.* Ref. [11]), the level of dissociation may depend on the atomistic details of the surface and on the coverage. Insight on the level of dissociation on oxide surfaces can be gained from surface science experiments

performed on ideal defect-free oxide surfaces and under ultra-high vacuum conditions. DFT calculations have often provided useful in the interpretation of experimental data. With regards to ZnO($10\bar{1}0$), DFT has been of aid to reveal a (2×1) water superstructure on the surface which has been imaged using scanning tunneling microscopy [100]. In this (2×1) superstructure one out of every two water molecules is dissociated, forming a so-called partially dissociated overlayer.

Previous theoretical work on the adsorption of water on ZnO($10\bar{1}0$) has focused on the structure of water using standard (*i.e.* GGA) density functionals [100–102]. Nevertheless, the water dissociation barrier resulting from standard GGA functionals may be underestimated due to the self-interaction error (see *e.g.* Ref. [19]). Also, it has been shown that the inclusion of dispersion interactions may alter the stability between two different adsorption modes of benzene on Si(001) compared to standard GGA functionals that neglect van der Waals dispersion forces [103]. Hence, in the second part of the Chapter (see Section 3.4) we investigate the adsorption of water on ZnO($10\bar{1}0$) using methods beyond the GGA, which include a fraction of exact exchange to give a better description of the water dissociation barrier, and that account for dispersion interactions.

3.2 Computational details

Static DFT calculations at zero K have been performed for the determination of the structure and energetics of clean and water covered ZnO($10\bar{1}0$). Within the framework of DFT we have used two different codes: VASP [104–

106], which uses plane waves to expand the wavefunctions of the valence electrons and the projector augmented wave method to treat the core electrons [71, 107]; and the CP2K/QUICKSTEP package [68, 69] which instead uses a combination of Gaussian and plane wave basis functions while the core electrons are treated using norm conserving pseudopotentials [108]. In VASP we used six valence electrons for oxygen ($2s^2 2p^4$) and twelve for zinc ($3d^{10} 4s^2$) and a cut-off of 500 eV for the plane wave expansion. Molecularly optimized double-ζ valence polarized (m-DZVP) basis functions are used for the Gaussian basis set [109] in CP2K and a 320 Ry cut-off for the plane wave expansion. Using m-TZVP basis functions for oxygen and hydrogen atoms changed the monomer adsorption energy by at most +15 meV/H_2O. In the VASP calculations we have employed a k-point mesh density of $6 \times 4 \times 1$ per primitive surface unit cell with the Monkhorst-Pack scheme [110]. Because it is only possible to sample k-space at the Γ point in CP2K a 6×4 unit cell has been used to reproduce the same k-point density as in the VASP calculations. We have relaxed all the atoms in the unit cell for the study of the clean surfaces, while in the case of water adsorption we have adsorbed water on one side of the slab and kept the other side fixed at its bulk-truncated position. Further, when adsorbing water a dipole correction has been used in VASP while the method by Martyna and Tuckerman [111] has been used in CP2K to treat the electrostatic interactions along the direction of the vacuum.

The comparison between the CP2K and the VASP codes have been performed using using the PBE functional [38]. Besides PBE we will also show the comparison with functionals which partially correct for the self-interaction error of DFT and that account for van der Waals dispersion

forces. In bulk ZnO self-interaction gives rise to a significant underestimation of the band-gap because of an excessive delocalization of Zn 3d-states. For instance, PBE predicts a value of 0.7 eV, as compared to the experimental gap of 3.4 eV [112]. DFT+U ameliorates this deficiency predicting an improved gap, depending on the value of the Hubbard-U parameter used. We apply the +U correction to PBE using with a value of U= 4.7 eV, according to Ref. [113]. Hybrid functionals also predict better gaps. We use the HSE06 [66] functional which predicts a gap of 2.5 eV, in much closer agreement with the experimental value than PBE (see *e.g.* [98]). Since the too large electron delocalization in PBE may affect the water dissociation barrier we will compare the transition from the intact to the partially dissociated state using the PBE and the HSE06 functional in Section 3.4. Further, van der Waals interactions may provide important contributions to the binding of water on solid surfaces, as shown *e.g.* in the case of 1D water chains on Cu(110) or Ru(0001) [114]. For this reason we also performed calculations of water adsorption on ZnO$(10\bar{1}0)$ using Grimme's D2 correction [46] and the optPBE-vdW and optB86b-vdW functionals [50, 51].

3.3 Structure and energetics of clean ZnO$(10\bar{1}0)$

The structure of ZnO$(10\bar{1}0)$ is shown in Fig. 3.2. Upon cleavage of the bulk crystal the ions in the first layers will relax and tilt to compensate for the missing bonds, as shown in Fig. 3.2(b). We focus here on the details and the magnitude of such relaxations. Table 3.1 summarizes the results for the structural and energetic properties of ZnO$(10\bar{1}0)$ as obtained using a

3 bilayer slab. We decide to model the ZnO$(10\bar{1}0)$ using a 3 bilayer slab because the structure and energetics are converged with such a number of bilayers. In agreement with LEED and angle-resolved photoemission ex-

Table 3.1: Structure and energetics of ZnO$(10\bar{1}0)$. Relaxation of the surface zinc ($\Delta d_\perp$(Zn)) and oxygen ($\Delta d_\perp$(O)) atoms with respect to their bulk position, bond length contraction ($C_{B,\parallel}$) and tilt angle ω_1 of the first layer Zn and O atoms, and the surface energy σ obtained for a 3 bilayer slab with the VASP and CP2K codes and with different functionals. Also reported are other DFT (PBE) and experimental (LEED) results, where the bracketed numbers identify quantities derived from those mentioned in the experiment.

	PBE^{CP2K}	PBE^{VASP}	PBE+U	HSE06	Other Theory[a]	Expt.[b]
$\Delta d_\perp$(Zn)(Å)	-0.28	-0.34	-0.49	-0.33	-0.36	-0.45 ± 0.1
$\Delta d_\perp$(O)(Å)	-0.01	-0.03	-0.24	-0.05	-0.04	-0.05 ± 0.1
ω_1	7.8°	9.4°	7.7°	8.3°	10.1°	$12° \pm 5°$
Δ(O$_1$−Zn$_1$) (Å)	0.27	0.31	0.25	0.27	0.33	0.40 ± 0.1
$C_{B,\parallel}$(%)	-6.5	-6.9	-6.9	-7.0	-7.2	-3
σ (meV/Å^2)	52.2	52.0	54.2	59.5	49.9	–

[a] Reference [88]
[b] Reference [90]

periments [90–92], our calculations predict an inward relaxation of the top Zn atom compared to bulk ZnO ($\Delta d_\perp$(Zn)), while the oxygen remains in its bulk position. This results in a tilting of the Zn–O bond in the top layer, with the cation below the anion, as seen in Fig. 3.2(b). A moderate tilting of the surface atoms with the surface cation moving downwards has been confirmed by other experimental studies and it also agrees with the PBE study from Meyer *et al.* [88]. The same type of surface reconstruction has been reported in other II-VI zinc-blende and wurtzite semiconductors [99, 115], and the underlying mechanism results from a competition between dehybridization from sp^3 to sp^2, typical of semiconductor surfaces, and charge transfer characteristic of ionic compounds (see e.g. Ref. [88]).

Upon formation of the surface, the top Zn and O atoms pass from being

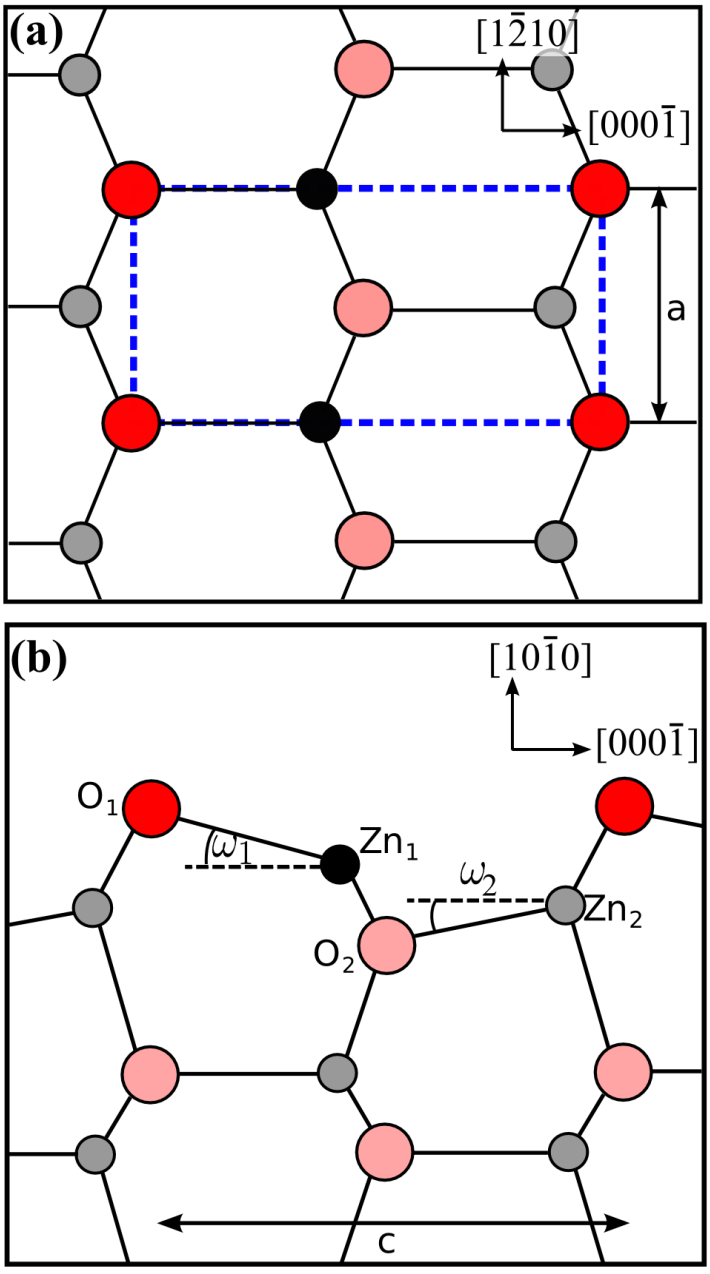

Figure 3.2: Illustration of the structure of ZnO(10$\bar{1}$0) in top (a) and side (b) views. Red and black circles are the O and Zn ions in the first layer, which are labelled as O_1 and Zn_1, respectively. The pink and grey circles are O and Zn ions in the second layer, labelled as O_2 and Zn_2. Also indicated is the tilt angle in the first two layers. The surface unit cell is indicated by dashed lines.

fourfold to threefold coordinated. In a predominantly covalent system the cation tends then to rehybridize from sp^3 to sp^2 and move towards the anions underneath, without significantly changing the bond length with the top anion (see *e.g.* Refs. [36, 88]). To compensate for the missing ions in a dominantly ionic compound instead, the attraction between the surface ions will be stronger compared to the bulk case, as is that towards the inner ions. This results in an overall relaxation towards the bulk and on a contraction of the surface bond-length, but without any tilting [36, 88]).

In ZnO we observe both a tilting of the top surface bond, (typical of covalently bound systems), and a surface relaxation towards the bulk with a contraction of the top Zn–O bond (typical of ionic systems). Only the GIXD work from Jedrecy *et al.* [93] has indicated a very small inward relaxation of the surface Zn atom (only -0.06 ± 0.02 Å), with the surface resulting in an almost bulk-like structure. In that study the surface oxygen is also predicted to lie 0.06 ± 0.06 Å below the zinc but this would be very unusual since, so far no wurtzite crystal in the $(10\bar{1}0)$ orientation has been reported to have a tilt with the cation above the anion.

From Table 3.1 it can be seen that PBE predicts a value of $\Delta d_{\perp}$(Zn) of -0.28 and -0.35 Å from CP2K and VASP, respectively. The value obtained from HSE06 is close to the PBE one, while PBE+U slightly overestimates the inward relaxation. Although PBE+U shows an inward oxygen relaxation of -0.24 Å, it is evident that the surface Zn-atom relaxes more towards the bulk, lying below the oxygen atom independent of the code or functional used. The net inward relaxation of the cation determines a pronounced tilting of the top

Zn–O bond with respect to the bulk-truncated surface of approximately 10° is indicated by ω_1 in Table 3.1 and displayed in Fig.3.2. We have also computed the quantity $\Delta(O_1-Zn_1)$ which is the difference along $[10\bar{1}0]$ between the position of the top oxygen and the top zinc atom, further illustrating that the oxygen atom lies between 0.3 and 0.4 Å above the zinc. As the top Zn and O atoms pass from being tetrahedrally coordinated to being three-fold coordinated, the surface Zn–O bond contracts of about 7% compared to the bulk, as illustrated by the bond length contraction $C_{B,\|}$.

An important quantity that measures the energetic cost needed to cut a bulk crystal into two semi-infinite ones is is the surface energy σ, defined as

$$\sigma = \frac{1}{2A}(E_{slab} - N_l E_{bulk}), \tag{3.1}$$

where E_{slab} is the total energy of a slab with N_l bilayers in the case of ZnO, E_{bulk} is the total energy of the bulk system per bilayer and A is the surface area exposed. The difference in total energy between a slab with $N_l + 1$ bilayers and N_l bilayers converges to the bulk total energy E_{bulk} provided that N_l is large enough (see *e.g.* Ref. [116]), so we decide to compute E_{bulk} as $E_{slab}(N_l+1)-E_{slab}(N_l)$ with $N_l = 6$. We obtain values of the surface energies which are around 52 meV/Å^2 with PBE, while PBE+U and HSE06 predict slightly larger values of 54.2 and 59.5 meV/Å^2, respectively. PBE and other GGA functionals are thought to underestimate surface energies of materials. In absence of experimental values of the surface energy we can compare with the LDA functional which is believed to perform better than GGAs from simple arguments based on jellium calculations and on experiments on simple

metals such as Pb or on simple oxides such as MgO [41–43]. Meyer *et al.* computed σ using LDA obtaining a larger value compared to PBE of 71.7 meV/Å^2 [88]. Using a fraction of exact exchange with the HSE06 functional we obtain an improvement on the surface energy, closer to the LDA value. It remains to be seen if the improvement of the surface energy with HSE06 is quite general and consistent with other systems, but overall more reliable experiments on the surface energies of materials would be welcomed for the benchmark of different functionals.

We mentioned that the surface relaxation and the surface energy are converged using 3 bilayer slabs to model the surface. We show that it is indeed the case by computing the quantities described in Table 3.1 as a function of the number of bilayers. Specifically, Fig. 3.3(a) illustrates that the distances between the atoms in the first bilayer projected along $[10\bar{1}0]$ are all converged using a 3 bilayer slab. This is also true for ω_1 and ω_2, which are the tilting angles of the Zn–O bonds in the first and second layer, respectively. The surface energy is also converged for a 3 bilayer slab as displayed in Fig. 3.4, where we also show a comparison with the different functionals used.

In order to estimate how much the surface relaxation and tilting propagates into the bulk we have computed the tilting angle and the parallel bond-length contraction $C_{B,\parallel}$ for an 18 layer slab as illustrated in Figs. 3.5(a) and 3.5(b), respectively. We only show the results obtained from PBE bulk Zn–O bond length and the surface ones – as the other functionals illustrate a very similar picture. It is clear that the the tilting propagates only $3-4$

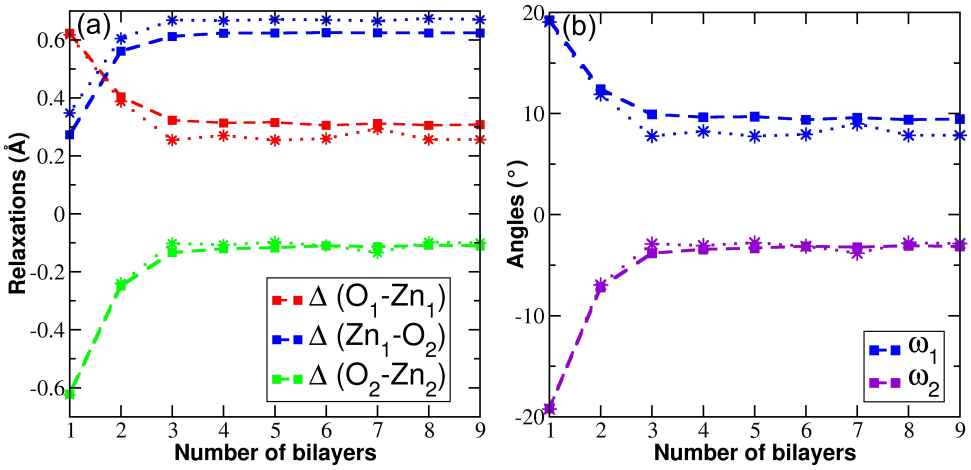

Figure 3.3: Structural relaxations (Fig. 3.3(a)) and tilt angles (Fig. 3.3(b)) relative to the coordinates as displayed in Fig.3.2 plotted against slabs with the reported total number of bilayers. The dashed lines (squares) refer to the VASP calculations obtained with PBE, the dotted (stars) lines refer to the CP2K ones. We keep this convention for the rest of the section.

layers towards the bulk as a consequence of the rehybridization of the top Zn cation. It is also clear from Fig. 3.5(b) how only the surface Zn–O bond is greatly affected by the missing ions in that a large bond-length contraction is observed only in the first layer, whereas subsequent bonds parallel to the (10$\bar{1}$0) display only minor contractions/expansions.

As a further evidence for the presence of a small inner relaxation, we illustrate the plot of the average inter-bilayer distance computed with PBE (Fig. 3.6) extracted as a percentage difference from the bulk value. The average for each bilayer has been taken by computing the mean value of the distances between each ion of the corresponding bilayer along the direction [10$\bar{1}$0]. The observed distance between the surface bilayers is reduced of $1-2\%$ from the bulk value, whereas the inner layers indicate very small displacements around $\pm 0.25\%$. Again, this same picture is observed also by

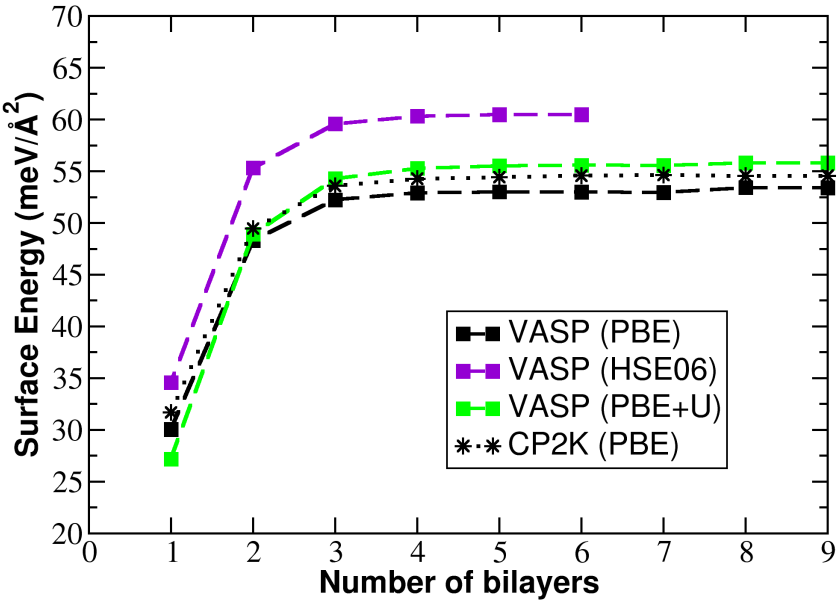

Figure 3.4: Surface energy computed for slabs with the indicated total number of bilayers and from different functionals. Convergence is achieved using 3 bilayer slabs.

the other functionals.

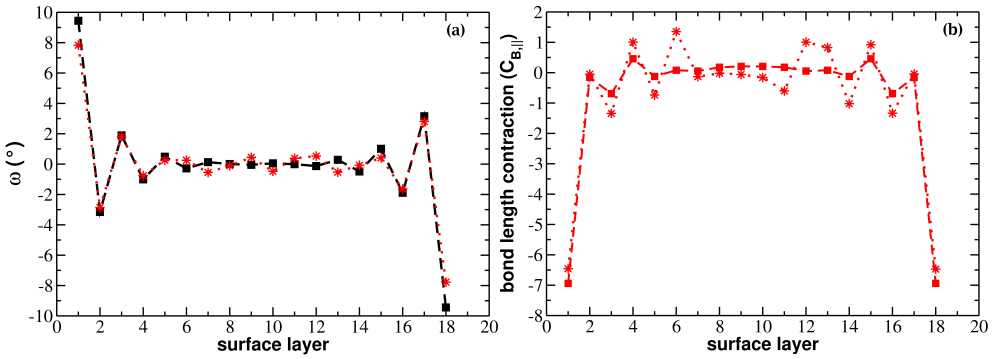

Figure 3.5: Deep-layer dimer tilting and bond-length contraction for an 18 layer slab. Figure 3.5(a) illustrates how deep in the bulk the buckling occurs and Fig. 3.5(b) shows the same phenomena for the surface bond-length contraction.

On the whole, the calculations of the structure of clean ZnO(10$\bar{1}$0) using

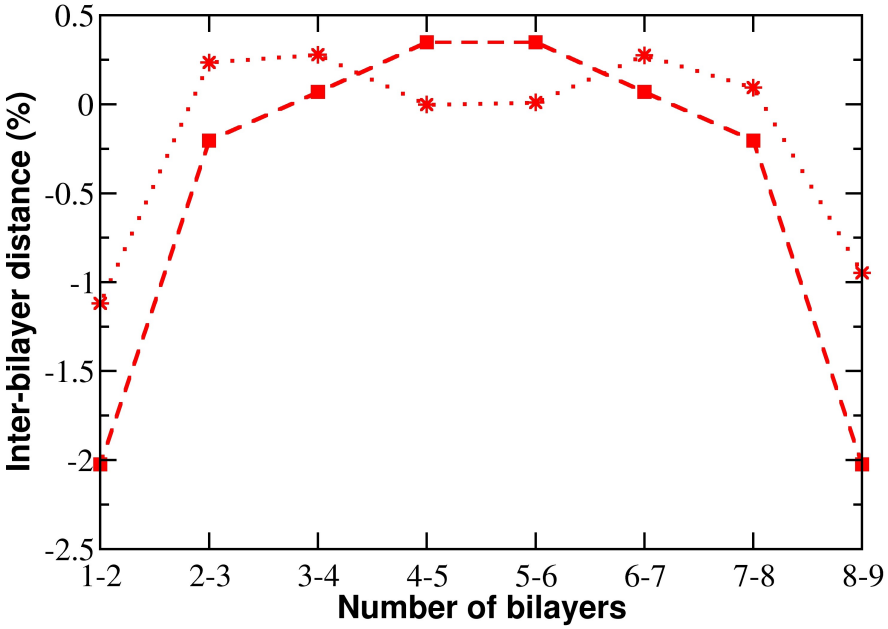

Figure 3.6: Inter-bilayer relaxation for an 18 layer slab, computed as the average distance along [10$\bar{1}$0] between the Zn and O ions belonging to the indicated surface bilayers.

two different DFT codes, with the standard PBE density functional and with PBE+U and HSE06 functionals have shown the same trends. We confirm that upon cleavage of the bulk the surface cation has an evident relaxation down towards the bulk of ≈ 0.3 Å, whereas the anion has a very small displacement from its bulk position. Overall, this gives rise to a tilting of the surface Zn–O bond of about 10°. Reducing the coordination of the top surface atoms from fourfold to threefold also gives gives rise to a contraction of the bond-length of $\approx 7\%$ from the bulk value. Further, we have demonstrated that inner layer reconstructions are not feasible for the studied surface and only very minor inner relaxations occur. Our study also shows that the predicted structural relaxations and reconstructions occurring in the first surface bilayer are in agreement with previous theoretical [88] and experimental

LEED [90] studies.

3.4 Water adsorption on ZnO$(10\bar{1}0)$

Having discussed the properties of the clean surface, we can now move on to the study of water adsorption on ZnO$(10\bar{1}0)$. Specifically, we examine the adsorption of an isolated water monomer and of water at ML coverage. The coverage θ is the number of adsorbates per adsorption sites. The number of adsorption sites per surface unit cell is 1 in the case of water on ZnO$(10\bar{1}0)$. We model the monomer adsorption by using a surface consisting of a 3 bilayer slab and with an H_2O molecule adsorbed at 1/6 ML (on a (3×2) surface unit cell). It has been shown in Ref. [102] that at 1/6 ML the interaction between neighbouring water molecules is negligible. We have also shown in Section 3.3 that the structure and energetics of the clean ZnO$(10\bar{1}0)$ are converged already using 3 bilayers, and also going from a 3 to a 4 bilayer slab gave rise to a change in the adsorption energy of the monomer of just 11 meV. We considered many possible adsorption structures and sites and we find that the most stable one is the one shown in Fig. 3.7(a) in agreement with Ref. [102]. Specifically, the water oxygen binds to the top-Zn atom and a H-bond is formed with the top O-atom and the overall water structure is in a key-lock configuration as discussed in Ref. [100]. We also compared the relative stability of water adsorbed at ML coverage in the M and PD states, as shown in Figs 3.7(b) and (c), respectively.

The adsorption energies of a water monomer and of water at ML coverage obtained with the CP2K and VASP codes using several functionals are shown

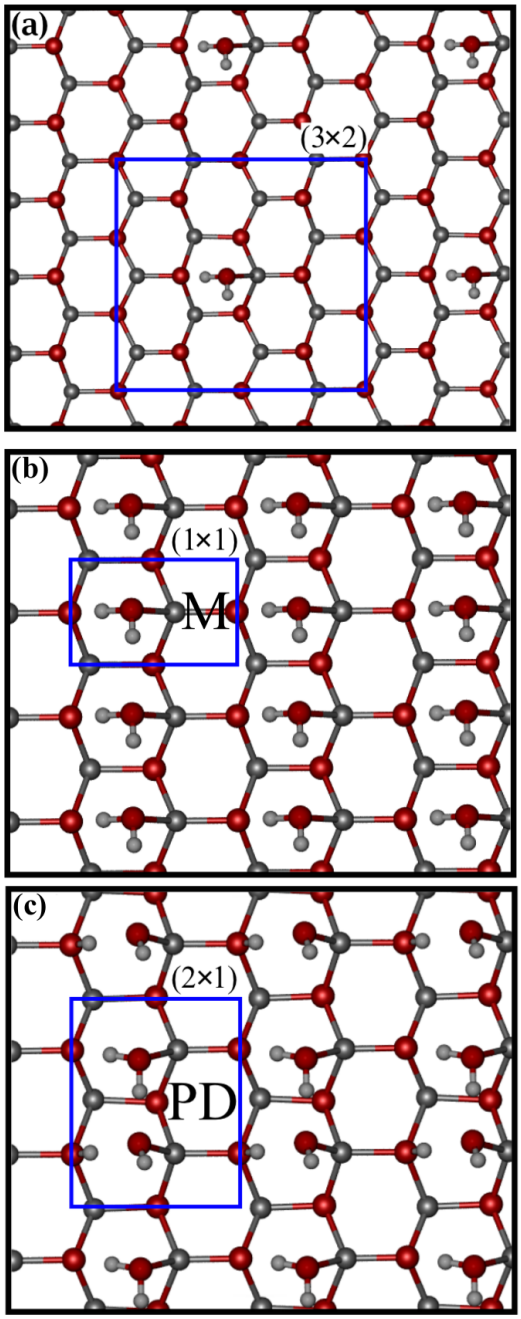

Figure 3.7: Top view of a water monomer on ZnO(10$\bar{1}$0) (a), of water at ML coverage in the molecular (M) state (b) and partially dissociated (PD) state (c). The solid boxes indicate the unit cell periodicity, specified on the top-right corner of the boxes.

in Table 3.2. The adsorption energy per water molecule E_{ads} is defined as $E_{ads} = [E_{H_2O/surf} - (E_{surf} + N \times E_{H_2O})]/N$, where $E_{H_2O/surf}$ is the total energy of the composite system with N adsorbed molecules, and E_{surf} and E_{H_2O} are the total energies of the clean surface and of a water monomer in gas phase, respectively. The table shows that water becomes more stable

Table 3.2: Adsorption energy of water on ZnO$(10\bar{1}0)$ predicted according to different functionals, in the case of monomer adsorption (at a coverage $\theta = 1/6$) and at monolayer coverage in the case of molecular ($\theta_M = 1$) and partially dissociated ($\theta_{PD} = 1$) states. Within brackets are adsorption energies corrected for zero point energy effects, obtained in the harmonic approximation from frequency calculations. Unless specified all reported values are obtained with VASP. All quantities are in eV/H_2O.

	$\theta = 1/6$	$\theta_M = 1$	$\theta_{PD} = 1$
PBE	-0.97	$-1.06(-0.99)$	$-1.17(-1.06)$
PBE^{CP2K}	-1.00	-1.09	-1.20
PBE-D2	-1.18	-1.35	-1.44
optPBE-vdW	-1.10	$-1.19(-1.12)$	$-1.32(-1.22)$
optB86b-vdW	-1.14	-1.23	-1.34
HSE06	-1.04	$-1.18(-1.09)$	$-1.30(-1.17)$
Other work	-0.94^a	-1.03	-1.13^b -1.02^c

[a] Reference [102] (DFT-PBE)
[b] Reference [100] (DFT-PBE)
[c] Reference [100] (Redhead analysis of temperature programmed desorption measurements)

upon increasing the coverage from 1/6 to 1 ML and that the PD state is slightly more stable than the M state (as noticed in Refs. [100, 102]). This holds regardless of the code used, or if dispersion is accounted for (with PBE-D2 [46] or optPBE-vdW and optB86b-vdW [50, 51]) and also if a fraction of exact exchange is used with the HSE06 functional [66]. The adsorption energy computed with CP2K is at most 10 meV/H_2O more stable than the one obtained from VASP, indicating that the basis set superposition error in our CP2K calculations is small. Adding a dispersion correction with any of the schemes used or the inclusion of 1/4 exact exchange with the HSE06

functional yields to further stabilization compared to PBE. On the whole, the energy difference between the PD and the M state is $\approx 0.1/H_2O$ eV with all functionals, with PBE being closer to the experimental value in Ref. [100], even if zero-point energy is accounted for. Indeed, Meyer *et. al.* performed a Redhead analysis on He thermal desorption spectroscopy (He-TDS) data and reported an adsorption energy of -1.02 eV for the PD structure, in close agreement with our zero-point energy corrected PBE value of -1.06 eV/H_2O.

The larger stability of the PD state can be easily understood by looking at the O–H bond length of the H_2O molecule in the different configurations. At $\theta = 1/6$ the O–H bond length is already stretched by 0.08 Å compared to an isolated water molecule in gas phase because of a hydrogen bond with the surface O atom. As the coverage increases so too does the stretching of the O–H bond. Indeed, the bond-length is stretched 0.04 Å more at ML coverage in the M state because of a hydrogen bond between neighbouring molecules. This further activates the O–H bond towards dissociation. A smaller stretching of 0.02 Å in the O–H bond length is observed in HSE06, This is another consequence of self-interaction, which causes in PBE a weaker O–H bond compared to HSE06.

To better understand the trends in the computed adsorption energies, we decompose the adsorption energy of the water ML in the M state into the contribution given by the binding energy of the water ML in the gas phase ($E_b^{\mathrm{wat-wat}}$) and water-surface interactions ($E_{inter}^{\mathrm{wat-surf}}$), namely $E_{ads}^{M} = E_{inter}^{\mathrm{wat-surf}} + E_b^{\mathrm{wat-wat}}$. Table 3.3 reports the results of such analysis, together with a further decomposition of the water ML binding energy into contribu-

Table 3.3: Decomposition of the adsorption energy of the water monolayer in its molecular state E_{ads}^{M}, into water-water binding $E_b^{wat-wat}$ and water-surface interaction $E_{inter}^{wat-surf}$. Further decomposition of $E_b^{wat-wat}$ into water-water interactions ($E_{inter}^{wat-wat}$) and water relaxation energy (E_{rel}^{H2O}). Within brackets are the contributions coming from exact exchange (E_{HFX}) for HSE06 and non local correlation (E_{nlc}) for optPBE-vdW and optB86b-vdW. All quantities expressed in eV/H_2O.

	PBE	HSE06 (E_{HFX})	optPBE-vdW (E_{nlc})	optB86b-vdW (E_{nlc})
E_{ads}^{M}	−1.06	−1.18(−0.49)	−1.19(−0.53)	−1.23(−0.52)
$E_{inter}^{wat-surf}$	−1.19	−1.29(−0.74)	−1.23(−0.47)	−1.33(−0.46)
$E_b^{wat-wat}$	+0.13	+0.05(+0.25)	+0.02(−0.06)	+0.10(−0.06)
$E_{inter}^{wat-wat}$	−0.14	−0.15(−0.02)	−0.17(−0.05)	−0.15(−0.05)
E_{rel}^{H2O}	+0.27	+0.20(+0.27)	+0.19(−0.01)	+0.25(−0.01)

tions coming from water-water interactions ($E_{inter}^{wat-wat}$) and from the relaxation of a water molecule in gas phase (E_{rel}^{H2O}), *i.e.* $E_b^{\mathrm{wat-wat}} = E_{inter}^{wat-wat} + E_{rel}^{H2O}$. All functionals predict a large attractive interaction of water to the surface ($E_{inter}^{wat-surf}$) between ≈ -1.2 eV with PBE to ≈ -1.3 eV/H_2O with optB86b-vdW. They also all indicate that a water ML in the adsorption (*i.e.* unrelaxed) configuration and without the substrate underneath is not stable compared to the relaxed water monomer in gas phase (i.e. $E_b^{wat-wat}$ is a positive number). However, the interaction energy between the water molecules in the free standing water monolayer ($E_{int}^{wat-wat}$) shows an attractive contribution to the binding between -0.17 and -0.15 eV/H_2O due to the hydrogen bond between neighbouring molecules.

We may now briefly compare the values obtained from the energy decomposition for each functional:

- PBE predicts a lower attraction of water to the surface compared to all other functionals with a water-surface interaction energy of -1.19 eV;
- The HSE06 functional predicts a stronger binding of water because of

a more attractive water-surface interaction, where more than half the value of $E_{inter}^{wat-surf}$ comes from Hartree-Fock exchange;

- The water-surface interactions computed with the vdW-functionals are also stronger than the PBE ones, because of a large contribution arising from the non-local correlation, which amounts to about 1/3 of the overall $E_{inter}^{wat-surf}$.

Finally, to elucidate whether or not dissociation of water is feasible at ML coverage, we compute the energy profile along the dissociation reaction from the M state to the PD state using PBE and HSE06, as shown in Fig. 3.8. Specifically, we plot the energy profile as a function of the distance between the water O-atom (O_w) and its active proton (H), while keeping the distance between O_d and O_w fixed to the equilibrium value in the M case. O_d represents the O-atom of the water that donates a H-bond to O_w. The particular procedure we applied for computing the dissociation barriers was to perform AIMD simulations at 10 K in the NVT ensemble with constraints on O_w-H and on O_w-O_d. Single point total energy calculations have then been performed on the structures resulting from the AIMDs. ΔE refers to the total energy difference from the initial (molecular) state obtained from these. The barrier obtained with PBE is only of 5 meV/H_2O. This is a tiny barrier and it can be seen that using the HSE06 functional only increases its value by less than 2 meV/H_2O. This is in contrast to the prediction of reaction barrier in gas phase, which represents a pathological example of the self-interaction error in DFT [62, 117]. Reaction barriers in gas phase systems are indeed severely underestimated using standard density functionals because electrons

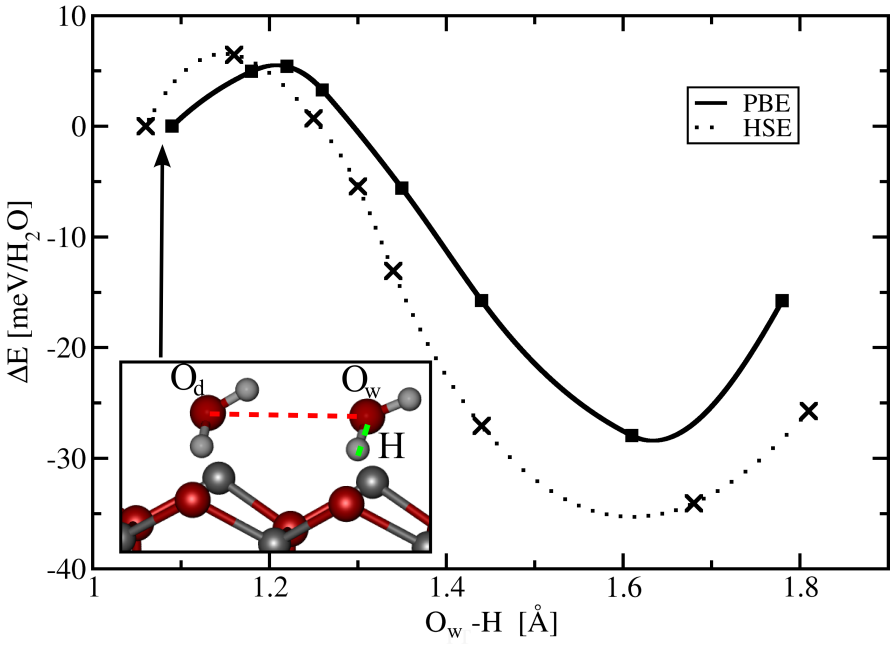

Figure 3.8: Energy pathways along the O_w-H bond-length for the transition from molecular water adsorption to partially dissociated adsorption. ΔE is the total energy difference from the initial (molecular) state resulting from single-point calculations. The distance O_w-O_d is kept fixed at 3.3 Å, which is the equilibrium value in the case of the initial molecular state. The barrier computed with HSE only increases of $\approx$ 2 meV/H_2O. The snapshot indicates the structure of the initial (molecular) state with the labels on the corresponding atoms.

are naturally more localized than in the condensed phase [118]. In condensed phase systems on the other hand, bands are generally more dispersed and therefore we argue that the delocalization error is not as critical for the calculation of barriers as it is in gas phase.

3.5 Conclusions

We can draw some important conclusions from the analysis performed in this chapter. First, we have demonstrated that the structure of the clean ZnO($10\bar{1}0$) presents a tilt of the top Zn–O bond of $\approx 10°$, resulting from a relaxation of the top cation of ≈ 0.3 Å towards the bulk, while the anion essentially does not move. This is in line with previous theoretical and experimental LEED work (see Refs. [88, 90]). Secondly, we confirm that water adsorbs strongly on ZnO($10\bar{1}0$), with a value of the adsorption energy around -1.0 eV/H_2O. There are two almost degenerate states, in which water can adsorb, one where water adsorbs intact and one where water is partially dissociated, with a difference between the two of ≈ 0.1 eV/H_2O. Whilst it stands to reason that water-surface interactions are the most dominant contribution to the adsorption energy, hydrogen bonding between neighbouring water molecules at ML coverage is a further cause of stabilization. It is the hydrogen bond between the neighbouring waters that favours dissociation and the formation of a (2×1) partially dissociated overlayer. The resulting degeneracy of the molecular and partially dissociated states along with the very small dissociation barrier of the order of a few meV, hint at a potentially very interesting dynamics of the protons at room temperature that we discuss in detail in Chapter 4.

Chapter 4

Proton hopping at the water/ZnO interface

4.1 Introduction

Proton transfer in water is a process of central importance to a number of fields in science and technology. Consider for example proton conduction across polymeric membranes used in fuel cells [119] or through protein channels in cells [120]. Proton transfer reactions are also key to many processes in catalysis such as the production of hydrogen from methanol or biomass [20, 121], or water formation [122]. Whilst it is notoriously difficult to characterize proton transfer under industrial or biological conditions, considerable insight and understanding has been gained by examining well-defined model systems. One such model system is the example of the solvated proton in pure liquid water [13, 123–125]. Another model system is water adsorbed

on atomically flat solid surfaces. Indeed, whereas traditionally most work on well defined water/solid interfaces has focused on structure characterization (e.g. Ref. [10] and references therein), increasingly the focus is turning to proton transfer and related properties such as surface acidity and water dissociation [126–132].

Of the various water-solid interfaces that have been examined, water on ZnO($10\bar{1}0$) plays a central role in heterogeneous catalysis [20, 100, 133] and light harvesting [84]. We mentioned in Chapter 3 that water on ZnO($10\bar{1}0$) is also a well-defined system that has been the focus of a number of studies under UHV conditions [100, 101] which have hinted at potentially interesting dynamical behavior. Specifically, Meyer *et al.* found that at ML coverage one out of every two water molecules is dissociated, forming the partially dissociated (PD) overlayer [100]. Subsequently they found that this PD overlayer could coexist with an overlayer of molecular (M) water [101]. Moreover, they suggested that the two states may rapidly interchange such that an average configuration, intermediate between the two, is at times observed in their scanning tunneling microscopy images. These findings prompted a number of follow up studies that focussed on the structure of water on the surface or on the level of dissociation [102, 134–137]. This previous work, along with the observation of a very small barrier from the M to the PD state of the order of a few meV (see Chapter 3), indicates that water on ZnO($10\bar{1}0$) might be a highly suitable system for investigating proton hopping in interfacial water. However, the key issue of how proton hopping occurs in this system and how it relates to the aqueous water environment is still not understood. Indeed, this is true for most water/solid interfaces where major gaps in our

understanding of the mechanisms of proton motion at interfaces remain.

This Chapter focuses on understanding proton transfer at the liquid water-ZnO($10\bar{1}0$) interface. Although techniques for characterization of well-defined aqueous interfaces have emerged (e.g. Refs. [126, 127]), probing the microscopic nature of proton transfer at interfaces remains a formidable challenge for experiment. On the other hand, AIMD as we use here, has reached such a state of maturity that it is now possible to simulate bond making and bond breaking events at complex solid-liquid interfaces (see e.g. Refs. [129, 130, 138, 139]). Here, we find that upon going from a water ML – characteristic of UHV – to a liquid film (LF) – characteristic of ambient conditions – changes in the structure and in the proton transfer dynamics of interfacial water are observed. Although moderate alterations in the structure of the contact layer are found, the proton transfer rate increases more than tenfold. Analysis reveals that H-bond fluctuations induced by the liquid are responsible for the structural change and for the substantial increase in proton transfer. This effect is unlikely to be specific to water on ZnO, implying that proton transfer may be significantly faster under aqueous conditions than at the low coverages typical of UHV-style studies. This fast proton transfer may also affect the chemical activity of a surface, being particularly relevant to heterogeneous catalysis under wet conditions [140–142].

4.2 Computational details

We have performed a series of AIMD simulations within the Born-Oppenheimer approximation using the CP2K/QUICKSTEP package [69], with the elec-

tronic structure computed at the DFT level. Most of the results that we present in the next sections have been obtained with the PBE exchange-correlation functional [38], although we will show a comparison with an AIMD simulation of the LF obtained using the "D2" correction of Grimme to include van der Waals dispersion interactions [46]. Molecularly optimized double-ζ valence polarized (m-DZVP) basis functions are used for the Gaussian basis set [109] in CP2K and a 320 Ry cut-off for the plane wave expansion as described also in Section 3.2. The surface model is made of (6×3) primitive unit cells and a 3 bilayer slab.

There is one water molecule per primitive cell at ML coverage, whereas the LF is comprised of 144 molecules, resulting in a $\approx$ 2 nm thick overlayer. The initial structure of the AIMD of the water ML was for water in the optimized M state, whereas the initial structure of the LF simulation has been obtained by running a 2 ns long classical MD simulation using a shell model for ZnO$(10\bar{1}0)$ [143], a polarizable SPC water model [144] and by using a Lennard-Jones potential to model the water-ZnO interactions. The parameters for the Lennard-Jones potential have been obtained by a fitting to our DFT-PBE data for water monomer adsorption. The trajectories have been obtained by propagating the dynamics in the canonical ensemble at a target temperature of 360 K. 360 K has been used to partially compensate for the lower diffusivity of water using the PBE functional [145]. The AIMD trajectories are 40 ps long with a 1 fs timestep, and we use deuterium masses for the hydrogens. This enables stable AIMD simulations to be performed with a 1 fs timestep. Specifically, the energy drift for the AIMD of liquid water on ZnO$(10\bar{1}0)$ is < 0.01 meV/(atom$\times$ps). The first 5 ps of the simulation

are used for equilibration and the remaining 35 for analysis. Equilibration in all the AIMD simulations has been performed for the initial 3 ps using the Bussi-Donadio-Parrinello thermostat [146], while for the remaining time the target temperature has been maintained with the Nosé-Hoover chain thermostat [80]. Overall we find that compared to other interfacial water systems this one is rather benign and none of our main conclusions are affected by the specific details of the DFT set-up. In particular, although the importance of van der Waals dispersion forces between water molecules and water on surfaces is being increasingly recognised (see e.g. Refs. [44, 114, 147, 148]) we will show that they do not have a significant impact on the dynamics of this system.

4.3 Structure of water on ZnO$(10\bar{1}0)$

Let us first consider the adsorption of water on ZnO$(10\bar{1}0)$ at ML coverage. Fig. 4.1(a) shows the spatial probability distribution function of the O and H atoms adsorbed on the surface at ML coverage. This illustrates the average structure of the overlayer projected onto the surface. Only the PD structure is observed, and it has a similar structure (bond lengths differ by < 0.05 Å) to the zero temperature geometry optimized structure. Figs. 4.1(c) and (d) show snapshots of the PD state in top and side views, respectively. The OHs and the H_2Os sit in the trenches and are covalently bound to the surface-Zn atoms. A H-bond is formed between the surface-Os and the H_2Os and also between the surface OHs and the dissociated water. In addition, the H_2Os donate a H-bond to the neighbouring OHs and lie essentially flat on

the surface, whereas the OHs are tilted up and point away from the surface.

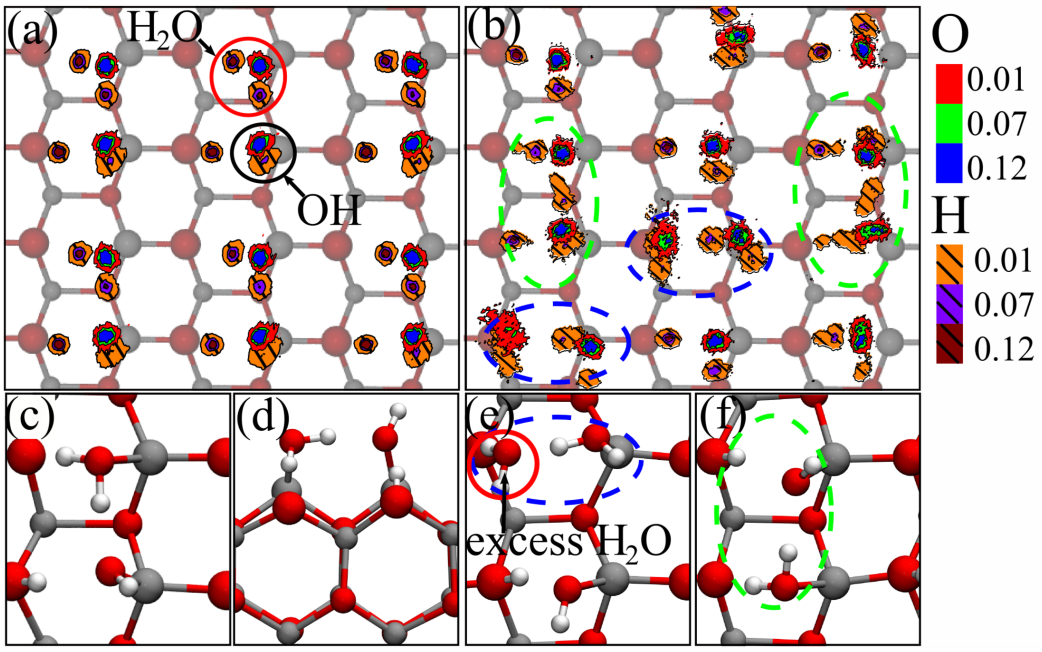

Figure 4.1: Spatial probability distribution function of the O and H atoms projected on ZnO(10$\bar{1}$0) for (a) the water monolayer and (b) the contact layer of the liquid film. Gray, red and white spheres are Zn, O, and H atoms, respectively. The topmost Zn and O surface atoms are shown using larger spheres. In (a) a H_2O and a OH that are connected via a H-bond are circled in red and black, respectively. (c) top and (d) side view of the partially dissociated water dimer, which is the basic building block of the (2×1) overlayer structure. Snapshots of the liquid film showing water in a new type of structure enclosed in a blue oval (e) and partially dissociated dimer structure enclosed in a green oval (f).

A snapshot of the LF is illustrated in Fig. 4.2(a) and in Fig. 4.2(b) the planar averaged density profile as a function of distance from the surface is reported, which has been obtained by averaging over an interval of 0.1 Å along the surface normal direction. The density profile shows a pronounced layering, as previously reported for other liquid/solid interfaces [132, 149–154]. For convenience we discuss the density profile in terms of the regions

observed, and label them from 0 to 3. Region 0 shows up as a small peak close to the surface and this corresponds to the chemisorbed Hs. These are the Hs that bond to the surface as a result of dissociation of some of the H_2Os. The large peak of ≈ 3.2 g/cm^3 in region 1 at about 2.0 Å corresponds to a mixture of OHs and H_2Os in immediate contact with the surface. The second peak in region 1 of about 0.7 g/cm^3 also arises from a mixture of OHs and H_2Os, that however sit on top of the surface-O atom. Between regions 1 and 2 there is a depletion of H_2Os, then in region 2 the oscillations are damped until in region 3 the density decay, characteristic of the liquid-vacuum interface, is observed [155].

The structure of the contact layer in the LF differs from the ML in a number of ways (*c.f.* Figs. 4.1(a) and (b)). First, although there are remnants of the (2×1) structure (see green ovals in Figs. 4.1(b) and (f)), the symmetry present at ML coverage is now broken. Second, the proton distribution is more delocalized in the contact layer of the LF than in the ML. Third, and most notably, the coverage in the LF has increased to 1.16 ± 0.03, with excess waters sitting in a new configuration on top of a surface-O (circled in red in Fig. 4.1(e)). At this new site adsorption can happen either molecularly or dissociatively and in either case the adsorbate accepts a H-bond from a H_2O sitting on the top-Zn site. Analysis of the overlayer reveals that H-bonding with the liquid above stabilizes the excess H_2O at the top-O site which gives rise to the higher coverage [156]. Despite the structural change between the ML and the contact layer of the LF, we did not observe any exchange of water.

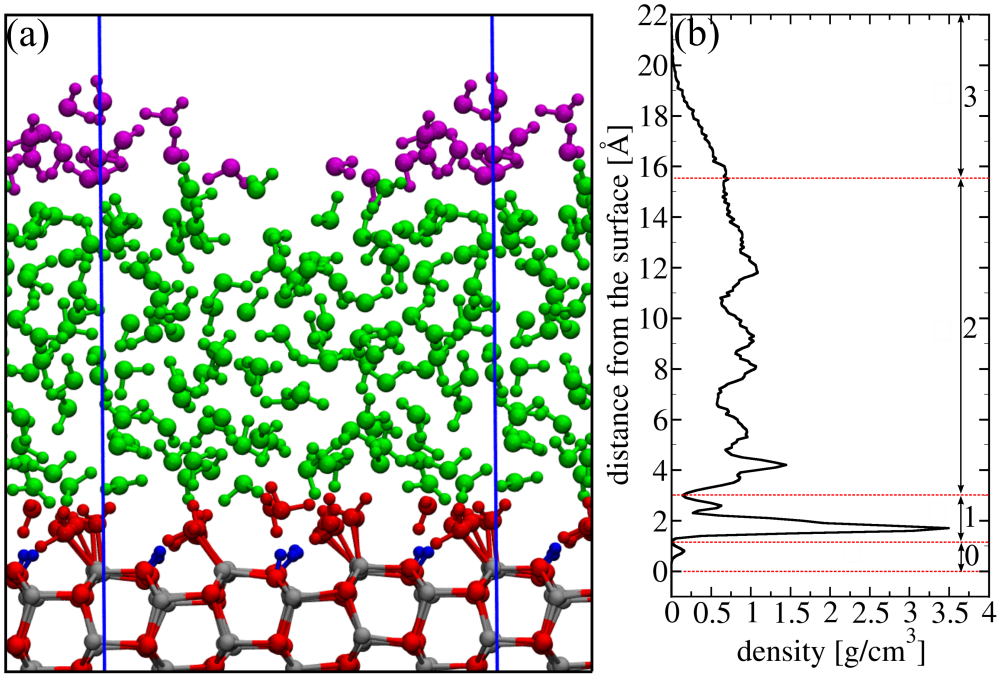

Figure 4.2: (a) Snapshot of a liquid water film on ZnO($10\bar{1}0$)(a). (b) Planar averaged density profile as a function of the distance from the surface, where different regions are identified and labelled from 0 to 3. In (b) the zero in the distance is the average height of the top surface ZnO layer and the density reported is the planar averaged density of adsorbed species. In (a) the top four surface layers are shown and the water overlayer is colored according to the regions shown in the density profile (b). Regions (going from 0 to 3) correspond to chemisorbed H atoms, H_2Os/OHs adsorbed on the surface, mainly bulk-like liquid water, and water in the liquid vapor interface.

4.3.1 Structure of liquid film from PBE-D2

Given the importance of van der Waals interactions to the structure of liquid water (see *e.g.* Ref. [148], we investigate the effect of van der Waals dispersion forces on the structure of the LF. Specifically, we have performed another AIMD simulation of the LF on ZnO($10\bar{1}0$), using the "D2" Grimme's correction [46]. A typical structure of the LF on ZnO($10\bar{1}0$) from PBE-D2 is shown in Fig. 4.3(a). Fig. 4.3(b) shows a comparison between the planar

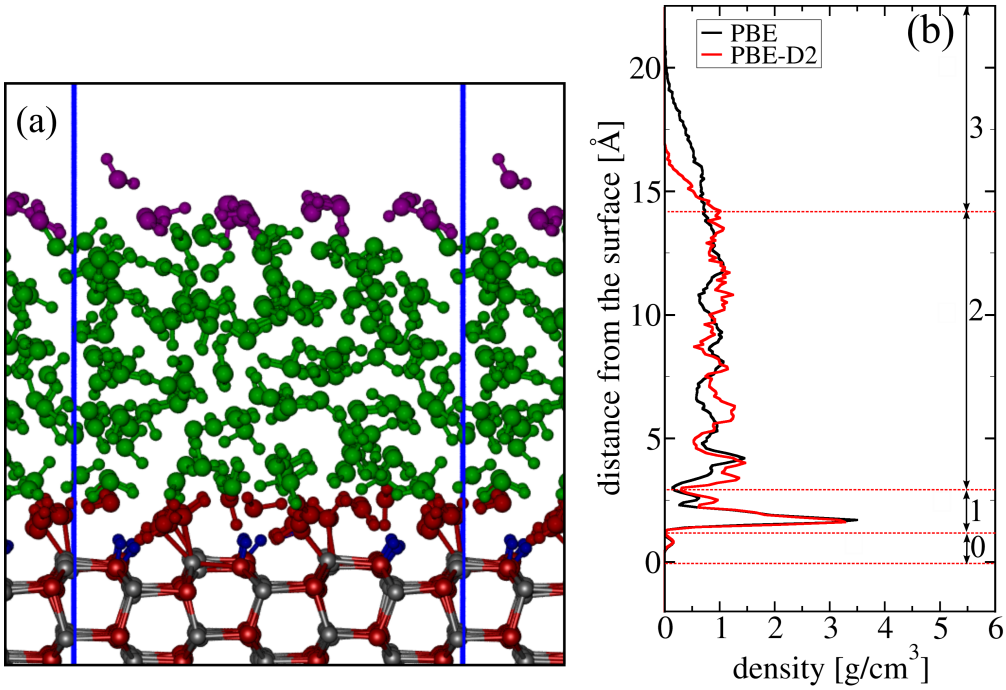

Figure 4.3: Snapshot of a liquid water film on ZnO(10$\bar{1}$0) taken from the AIMD PBE-D2 simulation(a). Planar average density profiles as a function of the distance from the surface for the PBE-D2 and PBE functionals in (b), where different regions are divided from 0 to 3. The zero in the distance is set as the average height of the top surface layer in (b). In (a) the top four surface layers are shown and the water overlayer is coloured according to the regions shown in the density profile (b). Each region corresponds (going from 0 to 3), to chemisorbed H atoms, water/hydroxyls adsorbed on the surface, bulk liquid water, water in the liquid vapour interface. The bin width along the surface normal in (b) is 0.1 Å.

average of the PBE-D2 and the PBE density profiles. Because of dispersion forces the density in the contact layer obtained from PBE-D2 has seen a slight increase in the first two peaks in region 1 at 2.0 and 2.5 Å. This results in an increase in the coverage from 1.16 ± 0.03 to 1.29 ± 0.04 of a ML. The density of PBE-D2 bulk liquid water (region 2) is 0.85 ± 0.14 g/cm^3, slightly larger than the PBE value of 0.75 ± 0.12 g/cm^3. Further, the decay at the liquid-vacuum interface is more rapid in the PBE-D2 density. Overall, we

have only seen a small change in the structure of the LF upon inclusion of dispersion. We will see in Section 4.4 if the increase in the coverage of 1.29 ± 0.04 affects the proton dynamics at the contact layer.

4.4 Proton dynamics at the water/ZnO interface

The level of dissociation is not altered in the ML and in the LF. This can be seen in Figs. 4.4(a) and (b) where the trajectory of the percentage of adsorbed H atoms is reported for the two systems. At an average of 50% dissociation in the case of the ML and $55 \pm 5\%$ for the contact layer of the LF the difference is not significant.

Nevertheless, remarkable differences in the proton transfer dynamics are observed. Fig. 4.4 shows that the hopping frequency of the protons has increased by more than an order of magnitude in the LF simulation compared to ML. This is the most important result of this work. The difference in the proton transfer dynamics between the ML and the LF is partly shown by the fluctuations in the percentage of adsorbed H atoms, which represent proton transfer events to and from the surface (Figs. 4.4(a) and (b)) We consider as adsorbed Hs those which are within 1.2 Å of a substrate O atom. Clearly by comparing Figs. 4.4(a) and (b) it can be seen that the fluctuations are much more pronounced in the LF than in the ML. However, proton transfer to and from the surface is only part of the story as proton hopping between the H_2Os and OHs is also observed in the contact layer of the LF. Indeed this is already clear by looking at the proton distribution within the green

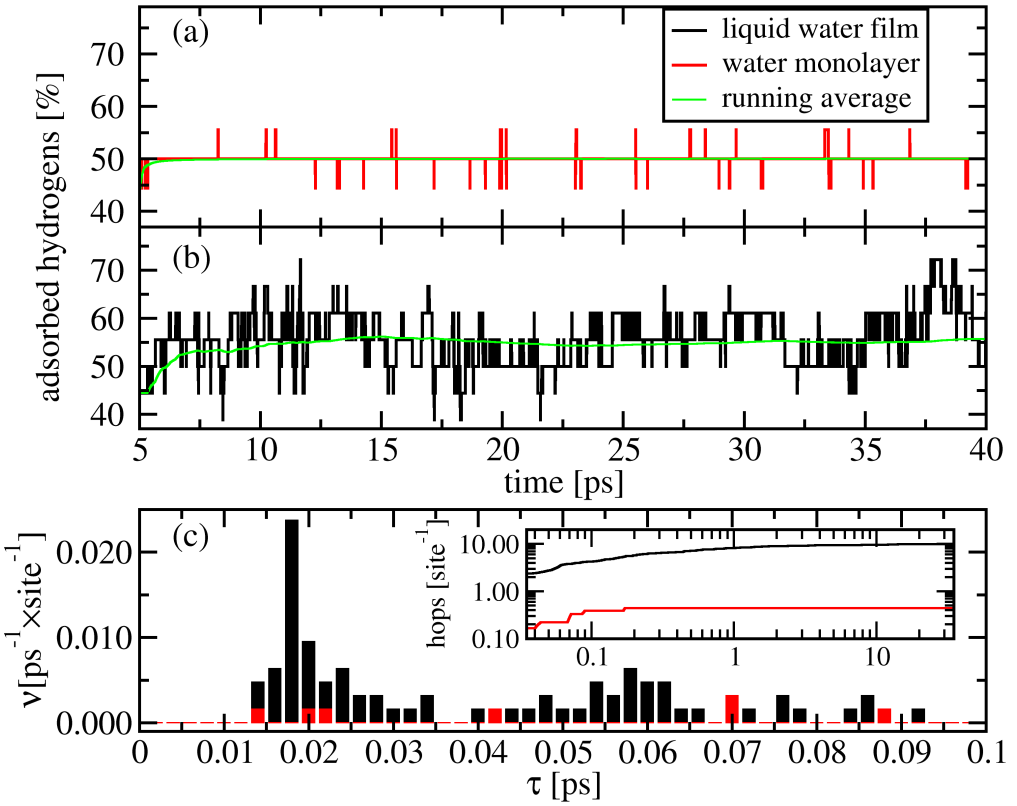

Figure 4.4: Time evolution of the percentage of H atoms adsorbed on the surface for (a) water monolayer and (b) liquid water overlayer. (c) Proton hopping frequency $\nu(\tau)$ as a function of the residence time τ for the liquid film (black) and the monolayer (red). The inset is a log-log plot of the total number of hops as a function of τ, obtained as $\int_0^\tau \nu(\tau')d\tau'$. The full 35 ps of analysis are shown in the inset.

ovals in Fig. 4.1(b). In the analysis reported in Fig. 4.4(c) all events are included and the hopping of each proton is monitored. Specifically, we plot the hopping frequency (ν = number of hops/(time×sites)) against τ. τ is defined as the time a proton takes to return to the O it was initially bonded to, and therefore measures the lifetime of a proton hopping event, with larger values of τ corresponding to longer lived events. Fig. 4.4(c) thus reveals that proton transfer is more frequent in the LF than in the ML. Specifically, in the

LF there are more events at all values of τ, with a maximum in the frequency distribution of about 0.02/(ps×site) at $\tau \approx 20$ fs. In contrast in the ML the ν distribution never reaches values larger than 0.005/(ps×site).

The ≈ 20 fs lifetime of the hopping events observed here is similar to the timescale of interconversion between Zundel-like and Eigen-like complexes in liquid water (< 100 fs) obtained from femtosecond spectroscopy [157]. It is also in the same ballpark as other theoretical estimates of proton transfer lifetimes obtained from work on proton transport in liquid water or on other water/solid interfaces [125, 158]. The total number of hops (inset in Fig. 4.4(c)) is ≈ 0.4/site in the ML but about 10/site in the LF. While only proton hopping between the overlayer and the surface is observed in the ML, in the LF $\approx 1/4$ of the hops are within the contact layer with the remaining 3/4 of all hops being to and from the surface. Proton hopping events are also longer lived in the LF than in the ML. This is demonstrated by the long tail in the frequency distribution of the LF and more clearly by the inset in Fig. 4.4(c), which shows that the longest hopping events are only about 0.2 ps in the ML but as long as ≈ 4 ps in the LF. Events with a lifetime on the order of the picosecond are characteristic of Grotthus-like diffusion [13] in liquid water or in other water/solid interfaces [130, 132, 158, 159], which are however not observed here, although such a process may occur at longer timescales than we can simulate [135].

4.4.1 Proton transfer from PBE-D2

In order to determine if dispersion has an effect on the proton transfer dynamics observed in Fig. 4.4(b), we also plot the percentage of adsorbed

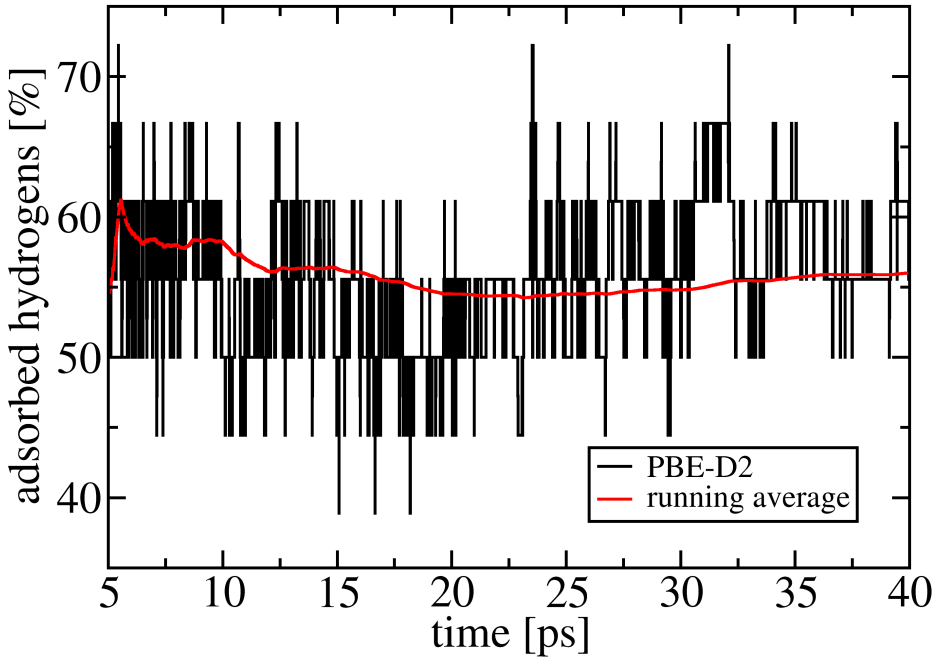

Figure 4.5: Time evolution of the percentage of H atoms adsorbed on the surface for the liquid water film simulation shown after 5 ps of equilibration. The inclusion of dispersion does not alter the proton transfer dynamics significantly nor does it produce a statistically relevant increase in the percentage of adsorbed Hs compared to the PBE simulation (see Fig 4.4(b)).

Hs as a function of the simulation time for the PBE-D2 LF simulation, as shown in Fig. 4.5. First we note that the level of dissociation does not change significantly compared to the PBE simulation (Fig. 4.4(b)). Indeed, there is a statistically insignificant increase in the percentage of adsorbed Hs to $56 \pm 5\%$ using PBE-D2, compared to $55 \pm 5\%$ with PBE. Above all, it can be seen that the rapid fluctuations in the number of adsorbed Hs is also seen in the PBE-D2 study, which show that the proton transfer dynamics is consistently

observed in our AIMD simulations with different levels of theory.

4.4.2 Comparison with previous force field work

Although we observed an increase in the coverage, the level of dissociation has not changed significantly with the presence of the LF. Accounting for dispersion forces with the empirical PBE-D2 [46] approach also does not alter our conclusion (see Fig. 4.5). In addition, our low coverage PBE results agree with previous work [100, 102] and the use of other dispersion corrections (with the optPBE-vdW and optB86b-vdW functionals [50, 51]) or of hybrid functionals (HSE06 [66]) does not change the stability between the M and the PD state at ML coverage (see Table 3.2 in Chapter 3). Further, the barrier to dissociation at ML coverage with HSE06 is not increased significantly compared to PBE (see Fig. 3.8). However, Raymand *et al.* [135] reported an increase in the level of dissociation to 80% in their reactive force field (ReaxFF) molecular dynamics simulations. The discrepancy has likely arisen from the different methods used. It is somewhat difficult to establish how reliable the ReaxFF method is also because details of the H and O parameters used have not been reported [135, 160]. We note that Holtaus *et al.* [136] have compared the level of dissociation of liquid water on ZnO($1\bar{2}10$) predicted by DFT-PBE, tight binding and ReaxFF and found a similar discrepancy between DFT-PBE and ReaxFF. They attributed the discrepancy between the two to a change in the charges in the contact layer upon increasing the

coverage that is not accounted for in the ReaxFF.

4.4.3 Explanation of the proton transfer mechanism

To gain further insights into the mechanism driving the increase in the proton transfer rate in the two systems we plot in Fig. 4.6 free energy (ΔF) surfaces ΔF for the various distinct proton transfer events considered here. The free energy surfaces have been obtained in a standard manner from $\Delta F = -k_B T \log P(\text{O-O},\delta)$. The probability distribution $P(\text{O-O},\delta)$ is a function of O-O distances and of δ, the position of the H with respect to the two Os. With reference to Fig. 4.6 $\delta_{1\text{-}2}$ is defined as the difference in the distances between H and two oxygens, O_1 and O_2, i.e. $\delta_{1\text{-}2} = O_1\text{-H} - O_2\text{-H}$. Looking at Fig. 4.6 we can see that there are some clear differences between the free energy surfaces of the ML and the LF. First, the single minimum in Fig. 4.6(a) shows that in the ML protons do not hop between adsorbed H_2O and OHs. In contrast in the LF two clear minima are identified revealing that hopping between adsorbed H_2Os and OHs occurs readily. The approximate free energy barrier of this process is ≈ 100 meV. Second, proton hopping to and from the surface happens both in the ML (Fig. 4.6(b)) and in the LF (Fig.4.6(d)), but the free energy barrier is noticeably lower in the LF (≈ 70 meV) than it is for the ML (≈ 160 meV).

In order to understand why hopping increases so much upon going from ML to multilayer we have examined the time dependence of the H-bonding network at the interface. This reveals an intimate connection between the local H-bonding environment of a molecule and its proclivity towards proton transfer. From the AIMD trajectory we see this connection between H-

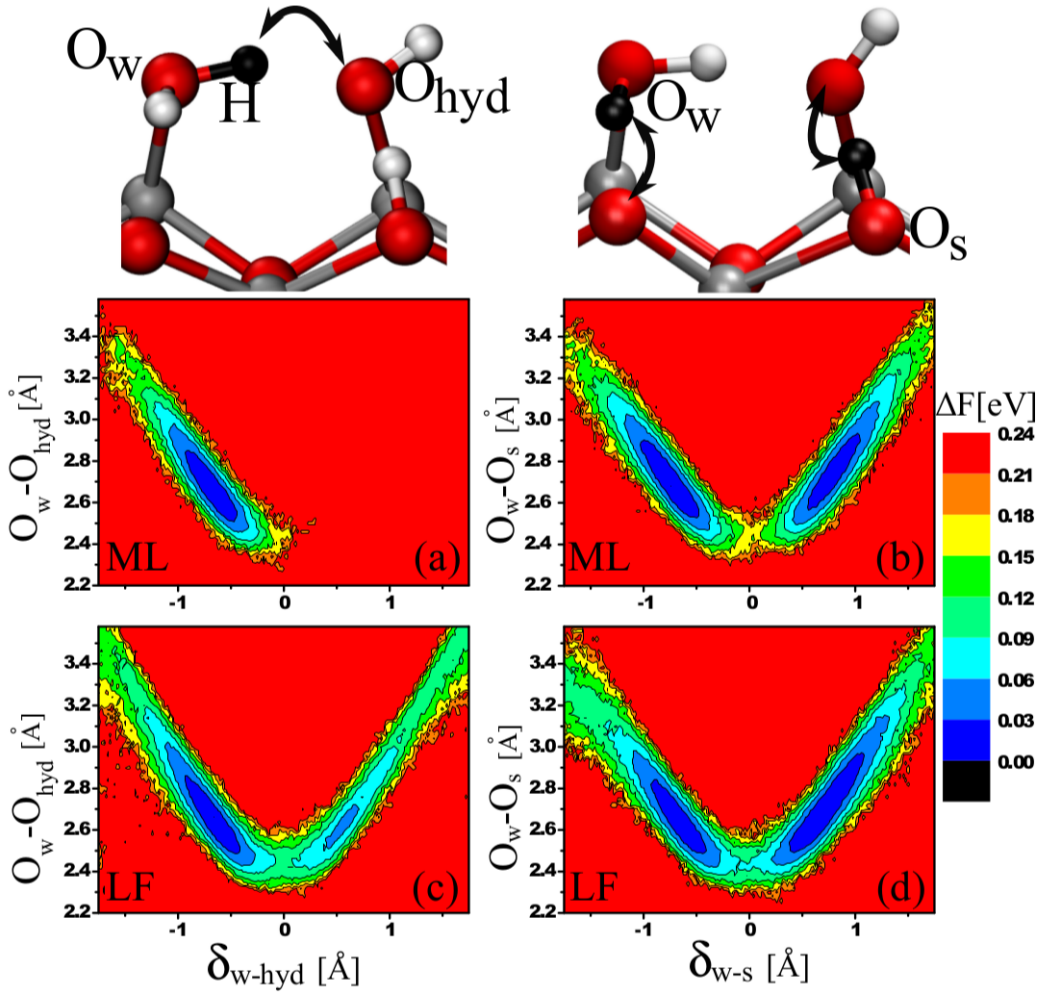

Figure 4.6: Free energy, ΔF contour plots for protons hopping between two Os as a function of the O-O distance and of the location of the protons between the two Os, δ. (a) and (b) show the free energies for the protons hopping in the water monolayer (ML) simulation, while (c) and (d) illustrate free energies in the liquid film (LF) simulation. As illustrated by the structures at the top of the figure, (a) and (c) refer to hopping between the Os in the contact layer and (b) and (d) refer to hopping of protons to and from the surface. The contour lines and colours are shown on the same scales.

bonding environment and the hopping of individual protons and we demonstrate in Fig. 4.7(a) that this holds on average for the entirety of all water-to-surface proton hopping events. Specifically, Fig. 4.7(a) shows the mean

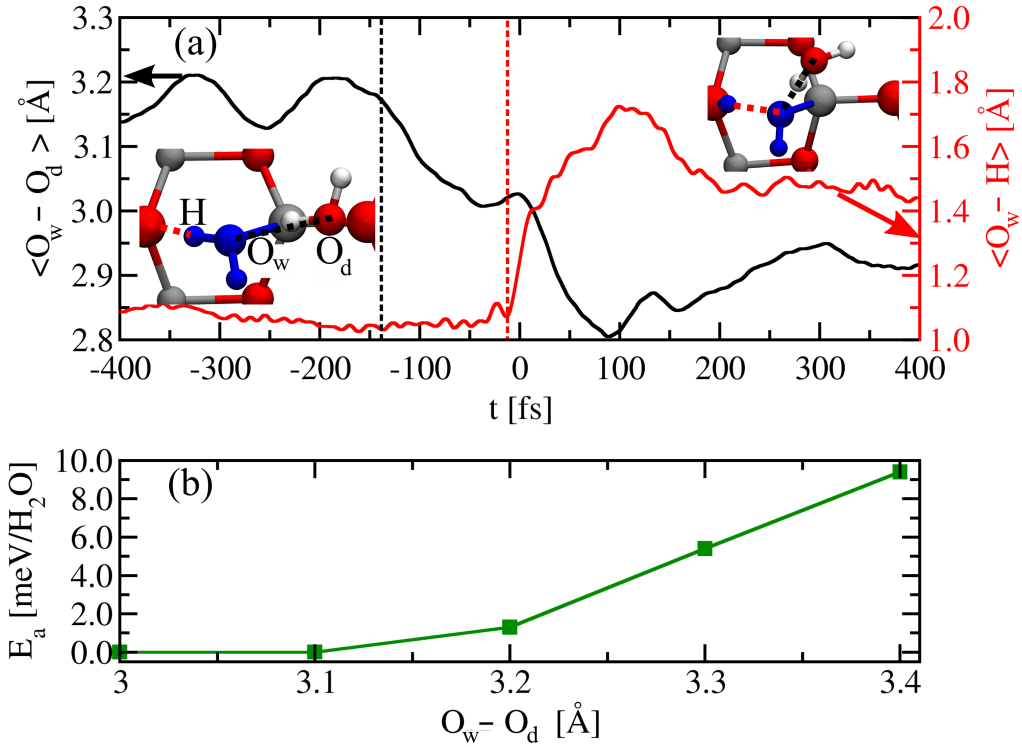

Figure 4.7: Analysis of the role of H-bond fluctuations on proton transfer. (a) Average O-O distance and average O-H distance as a function of time for all proton transfer events to the surface. The O-O distance plotted (black line) is the distance between the O of the molecule involved in the proton transfer event (O_w) and the O of the nearest molecule from which it accepts a H-bond (O_d). The O-H distance (red line) is the distance between O_w and the H that is involved in proton transfer. The black and red vertical lines indicate the approximate moment where there is a significant change in the $\langle O_w\text{-}O_d \rangle$ distances, respectively. The insets show snapshots of specific molecules before and after dissociation. (b) Activation energy (E_a) for water dissociation at ML coverage as a function of the O_w-O_d distance (calculated using VASP [104, 105], see Appendix A.1).

length of the O-H bonds that break in a proton transfer event ($\langle O_w\text{-}H \rangle$) as a function of time. We find that this is correlated with $\langle O_w\text{-}O_d \rangle$, the mean distance between O_w and O_d, where O_d is the O of the nearest molecule donating a H-bond to O_w. At time $t < 0$ water is intact at a distance $\langle O_w\text{-}H \rangle \approx 1.0$ Å. Just before $t = 0$, the point at which the $\langle O_w\text{-}H \rangle$ bond breaks,

there is a sharp increase in the $\langle O_w\text{-}H\rangle$ distance and then it levels off at $\approx$ 1.4 Å, about 200 fs after dissociation. Accompanying these changes in the $\langle O_w\text{-}H\rangle$ distance are changes in $\langle O_w\text{-}O_d\rangle$ distances. Crucially about 150 fs before proton transfer there is a net decrease in the intermolecular separation $\langle O_w\text{-}O_d\rangle$ that shortens from about 3.1 to 2.9 Å. It can be seen clearly that this change in intermolecular separation occurs before the $\langle O_w\text{-}H\rangle$ bonds start to break revealing that rearrangement in H-bonding is required prior to proton transfer. Similar behavior has recently been reported for the liquid water/InP(001) interface [132]. Further, O-H bond lengthening due to the presence of additional water was reported for water on Al_2O_3 [131]. Here, we illustrate that an increase in the O-H bond length occurs before the O-O distance decreases. Not only are the two distances correlated but it is the decrease in the O-O distance which produces an increase in the O-H distance.

Through a careful series of additional calculations in which an individual proton transfer event was examined we established that the proton transfer barrier depends critically on the intermolecular distance. As shown in Fig. 4.7(b) for relatively large distances of 3.4 Å there is a small $\approx$ 10 meV barrier. As the $O_w\text{-}O_d$ distance decreases, so too does the barrier until at $\approx$ 3.1 Å where there is no barrier and the intact water state is not stable. Given that fluctuations in the H-bond distances are more pronounced in the LF than in the ML and lead at times to relatively short $O_w\text{-}O_d$ separations, it is this that causes the more frequent proton transfer. An estimate of the H-bond distance fluctuations is obtained by computing the root mean square displacement the O-O distances in the contact layer, which gives 0.43 Å in the LF compared to the much smaller value of 0.15 Å in the ML. This increase

is also the reason why hopping does not occur between neighbouring H_2Os and OHs in the ML while it does in the LF. H-bond distance fluctuations are also responsible for a proportion of events having a lifetime of ≈ 1 ps or more (see inset of Fig. 4.4(c)), although actual hydrogen bond forming and breaking may participate in this case. While we never observe H-bond forming or breaking in the ML, the H-bond lifetime is of the order of the picosecond in the LF and this correlates well with the long lived proton transfer events.

4.5 Discussion and conclusions

We have shown that there are clear differences in the properties of water in contact with ZnO($10\bar{1}0$) upon going from UHV-like to more ambient-like conditions. Changes in the adsorption structure upon increasing the coverage above 1 ML have previously been predicted for a number of substrates including ZnO($10\bar{1}0$) [126, 131, 135, 161, 162]. The specific observation here is that the liquid water film leads to a $\approx 16\%$ increase in the water coverage and a breaking of the (2×1) periodicity observed at ML. This arises because of H-bonding between the molecules in the contact layer and the molecules above it. It should be possible to verify this increased capacity for water adsorption using a technique such as *in situ* surface X-ray diffraction.

We have demonstrated that there is a substantial increase in the proton transfer rate in the contact layer of the LF and that this is caused by H-bond fluctuations that lower the proton transfer barrier. A H-bond induced lowering of the dissociation barrier upon increasing the water coverage has been discussed before [100, 126, 131, 159, 163–165]. Here, however, we have

demonstrated that the barriers to dissociation and recombination are lowered in general because of the presence of the liquid. As in the case of liquid water and water on other substrates we show (Fig. 4.6) that there is a strong dependence between the proton transfer barrier and the distance between the Os on either side of the hopping proton [13, 123, 130, 166]. However, we have also identified a connection between the molecule involved in the proton transfer and the molecules in its first solvation shell (Fig. 4.7). This observation is somewhat similar to the structural diffusion of the excess proton in liquid water [13, 124]. The key difference between the two is that concerted H-bond breaking and making is required for proton diffusion in liquid water [125], while only fluctuations in the H-bond distance are needed for proton transfer (but not diffusion) to occur. Because fluctuations of the solvent provide the mechanism for the increased proton transfer rate, a similar effect is expected also on other substrates, e.g. on reactive metal surfaces upon which water dissociates [126, 163].

Finally, since the barrier to proton transfer is sensitive to changes in specific H-bond distances it is likely that implicit solvent models will be inadequate for this class of system as they do not account for H-bond fluctuations. A solvent induced increase in the proton transfer rate may also affect the chemical activity of the substrate and therefore have important consequences for heterogeneous catalysis under wet conditions [140–142, 167]. Given that the O-O distance correlates with the barrier height and that H-bond distances of adsorbed H_2Os/OHs are related to the lattice constant of the substrate, it might be possible to tailor the proton hopping rate through e.g. strain or doping of the substrate.

4.5. DISCUSSION AND CONCLUSIONS

In conclusion, we have reported on a detailed AIMD study of water on ZnO. In so doing we have tried to bridge the gap between studies of proton transfer in liquid water and low coverage UHV-style work. This has revealed a substantial increase in the rate of proton transfer upon increasing the coverage from a monolayer to a liquid multilayer. We have tracked down the enhanced proton transfer rate to specific solvent induced fluctuations in the H-bond network, which yield configurations with relatively short intermolecular distances wherein the barrier to proton transfer is lowered. These findings are potentially relevant to the modelling of wet interfaces in general and to heterogeneous catalysis.

Chapter 5

Friction of liquid water on graphene and hexagonal BN from *ab initio* methods

5.1 Introduction

Nanofluidics is an exciting field that offers alternative and sustainable solutions to problems relating to energy conversion, drug delivery, water filtration and desalination [21, 22, 24, 25, 168–173]. Miniaturization towards nanofluidic devices inevitably leads to an enhanced influence of surface and interface properties as opposed to those of the bulk. Friction is the most important interface property that limits fluid transport at the nanoscale, and its understanding is therefore crucial for the design of more efficient membranes, nanotubes and pores that exhibit low liquid/solid friction. The

behavior of liquid flow at scales on the order of a few tens of nanometres departs from continuum fluid dynamics and desirable transport properties emerge at such small scales [174]. For instance, carbon nanotubes have a very high water permeability as compared to the prediction of macroscopic fluid dynamics [168]. Further, a vanishing friction has been found, giving rise to superlubric behavior of water chains inside tubes of sub-nanometre radii [83].

Besides carbon, boron nitride (BN) nanostructures have recently been explored for the development of nanofluidic devices for fast water transport and efficient power generation [21, 175, 176]. Recent interest has been fueled by the demonstration that salinity concentration gradients across BN nanotube membranes can leed to the generation of very large electric currents [21]. It has also very recently been shown that there is a very large inter-layer friction between in multiwalled BN nanotubes [177], as opposed to the superlubric behavior of the (homopolar) carbon nanotubes [178]. This suggests that the frictional properties of BN and C nanostructures might be quite different. However, to the best of our knowledge there has been no attempt to measure or compute the friction of water at the interface with BN sheets or nanotubes. Given that *ab initio* results have shown very similar contact angles of water droplets on graphene and BN sheets [179], it remains to be seen if transport properties on these two systems are also similar.

The rise of the atomic force microscope and the surface force apparatus has advanced our understanding of nanoscale liquid/solid friction substantially [180]. Yet, it remains extremely hard to relate friction and dynamics

to structure and wetting of solid surfaces from experiment. This is especially true for the case of graphene where there is even controversy over the water contact angle (see *e.g.* Refs. [181, 182]). Molecular simulations, and especially force field molecular dynamics, have proved extremely useful in investigating structural and dynamical properties of confined liquids elucidating molecular level information that is challenging for experiments to obtain. Because of the dependence of simulation results on the parametrization of force fields, it is interesting to investigate the dynamics of interfacial water using electronic structure methods so that two different materials such as graphene and BN can be compared on an equal footing. Accordingly, *ab initio* molecular dynamics (AIMD) offers an interesting alternative that has been widely used to study complex liquid/solid interfaces (see *e.g.* Refs. [150, 179, 183]). Although transport properties in liquids have been computed before using AIMD (see *e.g.* Refs. [184–186]), we show for the first time that it is possible to compute a converged friction coefficient from AIMD.

In this work we compare the structure and dynamics of water in contact with BN and carbon nanostructures from AIMD. Specifically, we study liquid water in contact with graphene and hexagonal BN sheets, which is relevant to understanding flow at membranes based on these materials and also inside large nanotubes. The effect of nanotube curvature on the dynamics becomes negligible for a tube radius $R > 10\,\text{nm}$. [83, 187]. We find a striking similarity between the structure of water in contact with the two sheets. Nevertheless, there is a three-fold increase in the friction coefficient on BN because of a more corrugated free energy surface on BN compared to graphene. This work illustrates the complexity of nanoscale friction where subtle electronic

effects, with no detectable consequences on the structure of the interface, may however have a dramatic impact on water transport at the nanoscale.

5.2 Computational details

We performed a series of extensive AIMD simulations of a thin liquid water film on graphene and on a single layer of hexagonal BN, using a similar approach as the one in Chapter 4. Again, we used the CP2K/QUICKSTEP [69] package to perform AIMD simulations with the electronic structure computed at the DFT level.

5.2.1 Electronic structure Set-up

Specifically, we used the optB88-vdW exchange-correlation functional [50, 51], which has been shown to predict accurate interlayer binding and interlayer distances in graphite and bulk hexagonal BN [188], to give a good description of the structure of bulk liquid water [148] and also to correctly describe the relative stability of water-ice structures on metals compared to the bulk ice lattice energy [114]. We also performed a careful comparison between the results obtained with CP2K and VASP (v.2.3.2) [104, 105] for the calculation of the adsorption of a water monomer in gas phase. In CP2K we used short range molecularly optimized double-ζ valence polarized (m-DZVP) Gaussian basis functions, which exhibit a small basis set superposition error, comparable to traditional quadruple-ζ valence doubly polarized (QZV2P) basis functions [109]. Also a 460 Ry cut-off was used for the auxiliary plane wave expansion. The calculations with VASP have been performed using a cut-off of 600 eV for the plane wave expansion and with

six valence electrons for oxygen ($2s^2 2p^4$), four for carbon ($2s^2 sp^2$), three for boron ($2s^2 sp^1$) and five for nitrogen ($2s^2 sp^3$). The graphene and BN sheets are modelled using orthorhombic cells with C–C and B–N bond-lengths of 1.422 and Å, respectively, in agreement with Ref. [188]. Calculations in VASP have been performed on 3×5 orthorhombic cells with a k-point density of $2 \times 2 \times 1$ centered at the Γ point. In VASP, using a k-point density of $4 \times 4 \times 1$ changes the adsorption energy of a water monomer on graphene of only 0.3 meV/H_2O. In CP2K we reproduced the same k-point density by using 6×10 orthorhombic cells. A vacuum region of at 20 Å was used. A dipole correction along the direction of the vacuum has been used in VASP while in CP2K the sheets have been decoupled from their periodic images along the vacuum according to the method by Martyna and Tuckerman [111].

5.2.2 *Ab initio* and force field MD simulations set-up

The main results that we present in the next sections have been obtained performing AIMD simulations of water/graphene and water/BN sheets modelled using 6×10 orthorhombic cells about 25×25 Å^2 wide, with ≈ 20 Å thick liquid water films. There is a vacuum gap between the liquid-vacuum interface and the next periodic image of ≈ 15 Å. Each film contains 400 water molecules and in total each system consists of 1440 atoms. As an illustration, snapshots from the AIMD simulations for the water/graphene and water/BN interfaces are shown in Fig. 5.1(c) and (d), respectively.

Upon these systems we performed 40 ps long AIMD simulations with the last 35 ps of each trajectory used for analysis. We use 1 fs timestep and deuterium masses for the hydrogens in the AIMD to enable stable simulations

to be performed with a 1 fs timestep. This results in an energy drift of at most 0.011 meV/(ps×atom). The AIMD simulations are in the canonical ensemble with a target temperature of 330 K which is used to partially compensate for the lower diffusivity of water with the optB88-vdW functional under ambient conditions [148]. The first 5 ps of AIMD are used for equilibration and the remaining time for analysis. Equilibration has been performed for the initial 4 ps using the Bussi-Donadio-Parrinello thermostat [146], after which we switched to the Nosé-Hoover chain thermostat [80]. We also performed a number of additional AIMD and force field molecular dynamics (FFMD) simulations to explore the sensitivity of our results to the use of a different ensemble and to issues such as finite size effects, different initial conditions and time scales. We will show the results of these tests, which agree with those presented therein.

Specifically, we performed additional AIMD simulations, both in the canonical and in the microcanonical ensemble, on 3×5 BN and graphene cells containing 100 water molecules. The canonical runs are 70 ps long while the microcanonical runs are longer than 40 ps and their initial conditions have been obtained from equilibrated position and velocities of the canonical runs. Further, we computed the friction coefficient obtained from FFMD trajectories which are up to 10 ns long. We also use FFMD to obtain equilibrated configurations for the AIMD runs. FFMD have been performed using the GROMACS 4.5 [189] package where the electrostatic interactions have been accounted for using the particle mesh Ewald method. The rigid SPC/E [190] model for water and a Lennard-Jones potential to describe the water-surface interactions have been employed according to the works of

Werder *et al.* [191] on a water droplet on graphene and Won et al. [175] for the study of water transport in BN nanotubes. The Lennard-Jones parameters from Refs. [175, 191] are $\sigma_{OO} = 3.166$ Å, $\varepsilon_{OO} = 0.6502$ kJ/mol, $\sigma_{CC} = 3.214$ Å, $\varepsilon_{CC} = 0.2363$ kJ/mol, $\sigma_{BB} = 3.453$ Å, $\varepsilon_{BB} = 0.3971$ KJ/mol, $\sigma_{NN} = 3.365$ Å, $\varepsilon_{NN} = 0.606$ kJ/mol, where the water-surface interaction parameters are obtained using the standard mixing rules.

5.3 Very similar liquid film structure

We begin our analysis by illustrating in Fig. 5.1(a) the planar average density

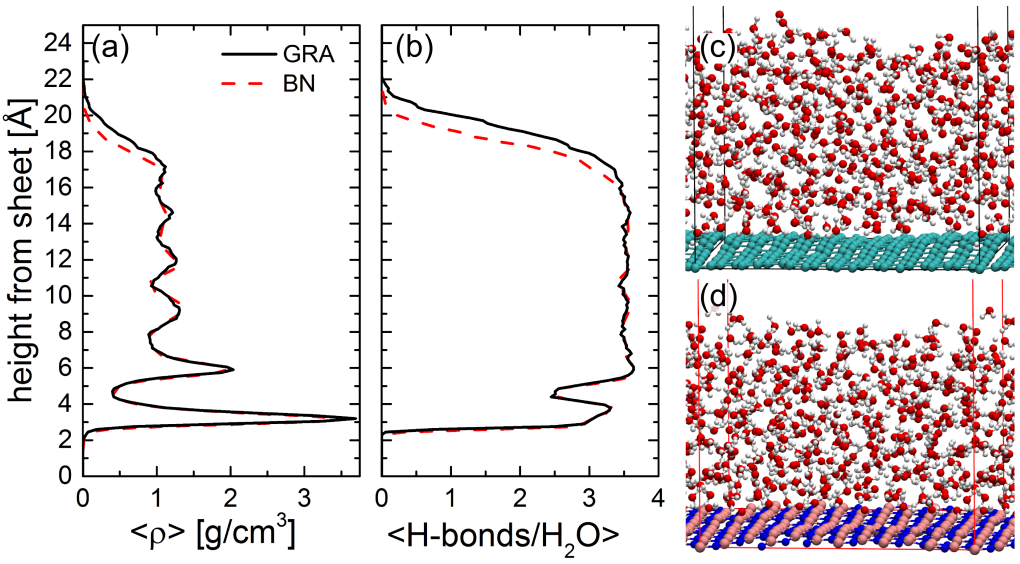

Figure 5.1: Structure of the liquid water film on graphene (GRA) and BN. Average density profile $\langle\rho\rangle$ (a) and number of hydrogen bonds $\langle$H-bonds/$H_2O\rangle$ (b) as a function of the height from the sheet. In (b) the geometric criterion from Luzar and Chandler was used to define a H-bond [192]. Snapshots of the liquid film on GRA (c) and on BN (d). In (c) and (d) O and H atoms are coloured in red and white, while C atoms are in light blue, and B and N atoms are in pink and purple, respectively.

profile $\langle\rho\rangle$ as a function of the height from the sheets. The graphene and BN

sheets exhibit oscillations in the heights of the atoms within them of up to 1.2 Å. To account for this, we compute the height of an atom in the liquid water overlayer as the height difference to the closest atom in the sheet. By computing the density profile in this way we fully account for the layering of the liquid film, which would otherwise be partially hidden behind the oscillations of the sheets. The two density profiles on graphene and BN overlap for most of the film height, which is the first signature of the apparent similarity of the structure of liquid water on the two sheets. Perturbation from the bulk liquid induced by the surface is most significant within the first 10 Å of the surface. This is consistent with previous reports on liquid water/solid interfaces (see *e.g.* Refs. [150, 183, 193, 194]), which extends in this case to about 8 Å from the sheets. Within this region there are two evident peaks for each of the two density profiles. The first at a height of about 3.0 Å hits a density maximum of ≈ 3.7 g/cm^3. After this first peak there is a depletion of water with a minimum at about 4.5 Å with a density of 0.4 g/cm^3. We define the contact layer as the region delimited by this minimum in the density profile. At ≈ 6.0 Å the second peak appears with a density of ≈ 2 g/cm^3. Further away from the sheets, density oscillations are gradually suppressed and the density of liquid water is recovered with an average value of 1.12 ± 0.16 g/cm^3. Finally, the density decays as it is characteristic of the liquid-vapor interface [155]. The decay in the density on BN starts off at about 17 Å, slightly before than on graphene simply because the BN unit cell is $\approx 3.5\%$ larger.

As further confirmation of the striking similarity between the structure of liquid water on graphene and BN, we compare the profile of the average

number of H-bonds per molecule, $\langle$H-bonds/$H_2O\rangle$ in Fig. 5.1(b). Also in this case the two curves essentially lie on top of each other for all of the film height apart from the liquid-vapour interface region. The steep increase in the $\langle$H-bonds/$H_2O\rangle$ starting at about 2 Å shows that already in the contact layer water molecules engage in a large number of H-bonds of $\approx 3/H_2O$. Shortly after this initial increase, there is a drop to ≈ 2.5 H-bonds/H_2O corresponding to the depletion region around 4.5 Å from the sheet. The pronounced fluctuations in the number of water molecules in this region partly penalizes H-bonding with neighboring waters. After the depletion region, at a height of 5 Å, the number the $\langle$H-bonds/$H_2O\rangle$ rises to the bulk value of ≈ 3.5. It remains constant until the liquid-vapour region is approached, at a height of 17 Å, where there is a rapid decay to zero in the $\langle$H-bonds/$H_2O\rangle$ within 3 to 4 Å.

Finally, other structural characteristics of the two systems exhibit striking similarities, such as the orientations of the water molecules within the films. Specifically, we computed the probability distributions of the angles between the water dipole moment and the vertical direction from the sheets as shown in Fig. 5.2. Again the similarity between the two systems, as evinced from Fig. 5.2(a) and (b) is striking. Water in the contact layer orients with its dipole predominantly tangential to the sheets, as previously reported for water on hydrophobic surfaces or for water confined between graphene sheets or for water droplets on graphene and BN [150, 179, 195]. Indeed, the majority of molecules in the contact layer orient their dipoles around 60° and 100°, while there is a scarce probability of molecules pointing up opposite to the sheets ($\varphi = 0°$) or down, towards them ($\varphi = 180°$). In the depletion region,

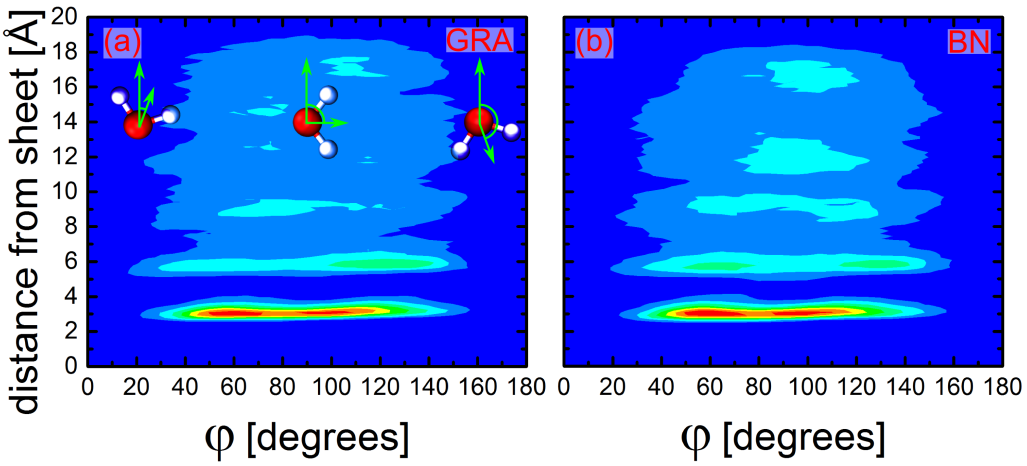

Figure 5.2: Probability distribution of the angle φ between the water dipole and the vertical direction as a function of the height from the sheet for (a) graphene (GRA) and (b) BN. The colour scale goes from red (large probability) to blue (low probability). The same criterion as in Fig. 1 in the main text is used for the distance of a water molecule from the sheet. The snapshots in (a) illustrate three different possible orientations of a water molecule.

at a height of about 5 Å, there is instead a uniform distribution of the dipoles. Affected by the pronounced reorientation of waters in the first layer, molecules in the second layer orient with their dipoles between 30° and 150°. After the second layer the distribution of angles becomes more homogeneous. Yet, because of the presence of the two interfaces (*i.e.* with the sheets and the vacuum) within just a 2 nm thick film, a region where the distribution is completely homogeneous and bulk-like is not observed.

5.4 Very different friction coefficient

Having compared the structure of liquid water on the two sheets we now turn our discussion to investigate its dynamics. Specifically, we focus on the friction coefficient λ, defined as the ratio between the friction force parallel to the

sheet F_p per unit area ($\mathcal{A}$) and v_{slip}, the velocity jump at the interface [174], namely $\lambda = F_p/(\mathcal{A}\, v_{slip})$. In the framework of linear response theory, λ can be obtained from the equilibrium fluctuations of the friction force, using a Green-Kubo relation [196, 197]:

$$\lambda = \lim_{t\to\infty} \lambda_{GK}(t), \tag{5.1}$$

with

$$\lambda_{GK}(t) = \frac{1}{\mathcal{A} k_{\mathrm{B}} T} \int_0^t \langle F_p(t') F_p(0) \rangle \, \mathrm{d}t' \tag{5.2}$$

where k_{B} is the Boltzmann constant and T the temperature. We show in Fig. 5.3 $\lambda_{GK}(t)$ for the case of water on graphene and on BN, which for sufficiently long time intervals (here approximately > 0.3 ps) plateaues to the value of λ. The key result is that the friction coefficients on the two sheets differ significantly, with the friction on BN being approximately 3 times larger than on graphene. Specifically, while $\lambda = (10.3 \pm 3.3) \times 10^4\,\mathrm{N\,s\,m^{-3}}$ for graphene, we obtain a value on BN of $\lambda = (27.5 \pm 6.9) \times 10^4\,\mathrm{N\,s\,m^{-3}}$. Whilst liquid/solid friction is the relevant microscopic property that quantifies the dynamics of a fluid at the nanoscale, a length scale characteristic of the flow is often measured experimentally. This is the so called slip length b, defined as the distance relative to the surface where the linear extrapolation of the tangential flow velocity vanishes. We can relate the slip length b to the friction coefficient via the shear viscosity of bulk liquid water η: $b = \eta/\lambda$ [174]. Using the experimental bulk water viscosity $\eta = 10^{-3}\,\mathrm{Pa\,s}$, the corresponding slip lengths for graphene and BN are 9.7 ± 3.1 and 3.6 ± 0.9 nm, respectively. In the absence of experiments on graphene or BN we compare

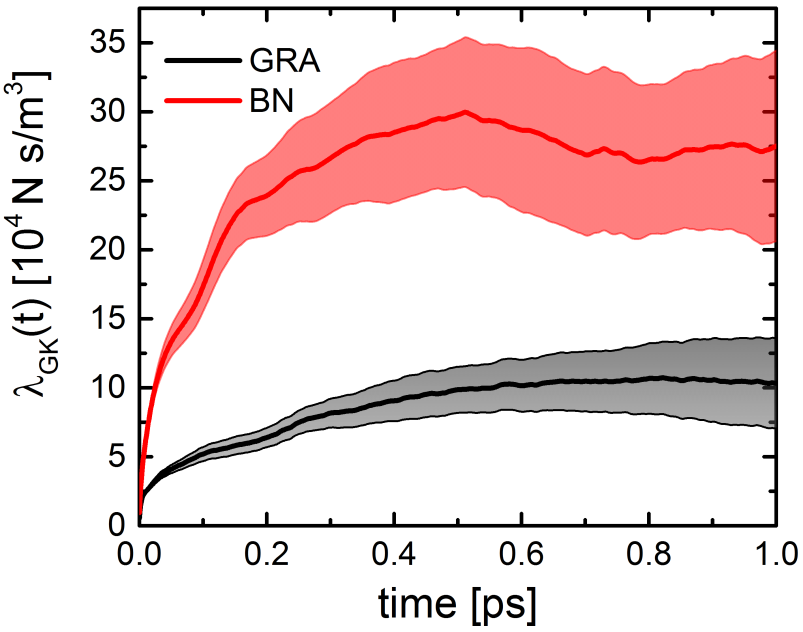

Figure 5.3: Comparison between the Green-Kubo estimate of the friction coefficient of liquid water on graphene (GRA) and on BN. The shaded areas represent the uncertainties obtained by performing a block average. The friction coefficient λ is given by the plateau value at long times. There is an evident increase in the friction coefficient on BN.

our results to those obtained from atomic force microscopy measurements of water droplets on atomically smooth highly ordered pyrolitic graphite which have given slip lengths of between 8 and 12 nm [198, 199]. These values are within the error bars of our estimate for the graphene slip length and in better agreement than previous force field work reporting about 83 nm [83, 187]. Although on graphene water transport may differ from that on graphite due to *e.g.* screening effects that may influence the binding on the two systems [200], we do not expect the friction to change between graphene and graphite by more than a few percent. Overall water slippage on graphene and

BN is characteristic of hydrophobic surfaces with an extremely low friction coefficient, while on hydrophilic surfaces such as mica, silicon, or graphene oxide slippage is significantly inhibited with sub-nm slip lengths [199, 201].

5.4.1 Validation results on the friction coefficient

The increase of about three times in the friction on BN compared to graphene

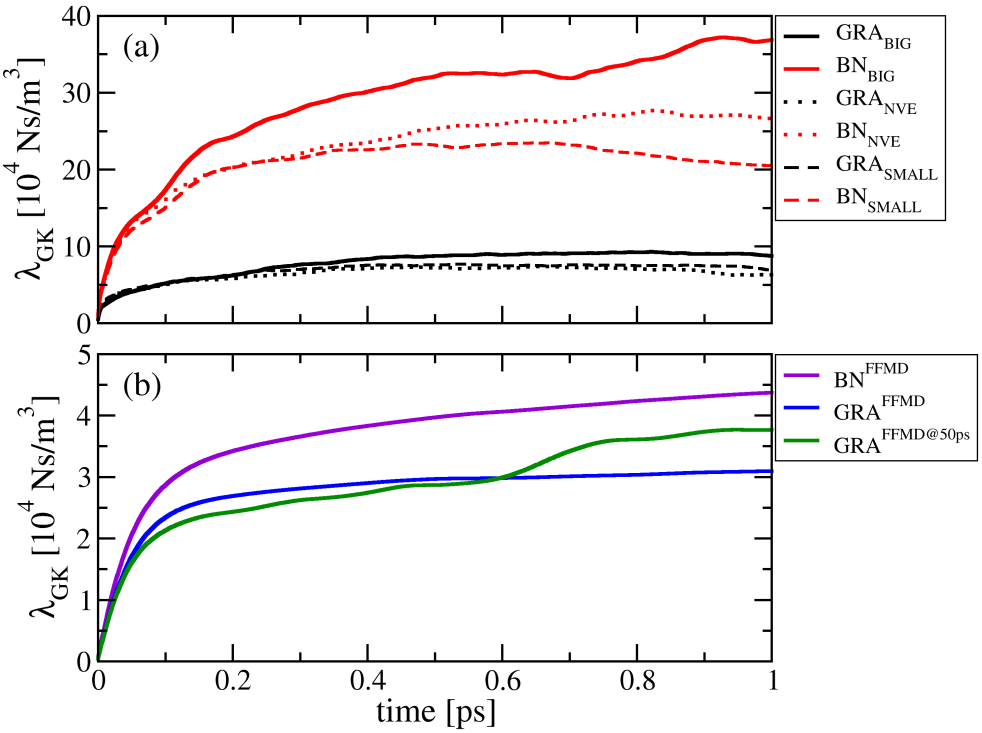

Figure 5.4: Validation results on the friction coefficient λ_{GK} of liquid water on graphene (GRA) and on BN computed using different ensembles and system sizes (a), and over different time scales (b). In (a) GRA$_{\mathrm{BIG}}$ and BN$_{\mathrm{BIG}}$ refer to λ_{GK} extracted from the simulations performed on the large 6×10 cells (as reported in the main text), GRA$_{\mathrm{SMALL}}$ and BN$_{\mathrm{SMALL}}$ refer to simulations performed in the smaller 3×5 cells and GRA$_{\mathrm{NVE}}$ and BN$_{\mathrm{NVE}}$ refer to simulations on the "small" cell performed in the NVE ensemble. In (b) we show the value of λ_{GK} obtained from FFMD simulations and computed over 50 ps of trajectory (GRA $^{\mathrm{FFMD@50\ ps}}$) and over the full 10 ns trajectory (GRA$^{\mathrm{FFMD}}$).

is consistently observed, regardless of the type of ensemble used, time scales, or different system sizes. As a validation of the results on the friction coefficient illustrated in Fig. 5.3 we show in Fig. 5.4(a) the values of $\lambda_{GK}(t)$ obtained from different simulation set-ups and models of the two interfaces. It can be seen that the increase in the friction coefficient on BN is consistent even if it is computed on a system consisting of a 3×5 cell (in Fig. 5.4(a) denoted as "SMALL") instead of the "BIG" 6×10 cell discussed so far, and even if the AIMD simulations are performed in the microcanonical ensemble (NVE) instead of the canonical one. Given that the AIMD simulations performed in the 3×5 cells are 70 ps long, *i.e.* 30 ps longer than the larger 6×10 cells, we have also demonstrated that the friction coefficient is already converged for trajectories which are ≈ 35 ps long. As a further demonstration of the convergence of the friction from our AIMD simulations we have compared the values of $\lambda_{GK}(t)$ for graphene with FFMD in Fig. 5.4(b). Indeed, the friction coefficient is already converged if it is computed over a trajectory of 50 ps as opposed to the full 10 ns. Most importantly it is clear from Fig. 5.4(b) that FFMD cannot reproduce the 3-fold increase in the friction coefficient on BN.

5.5 Why is the friction coefficient different?

To rationalize the difference in the two friction coefficients in terms of structural and energetic contributions, we compute the free energy profile of water within the contact layer $\Delta G(x, y)$, defined as $\Delta G(x, y) = -k_B T \ln P_O(x, y)$. Here, $P_O(x, y)$ is the spatial probability distribution function of the O atom

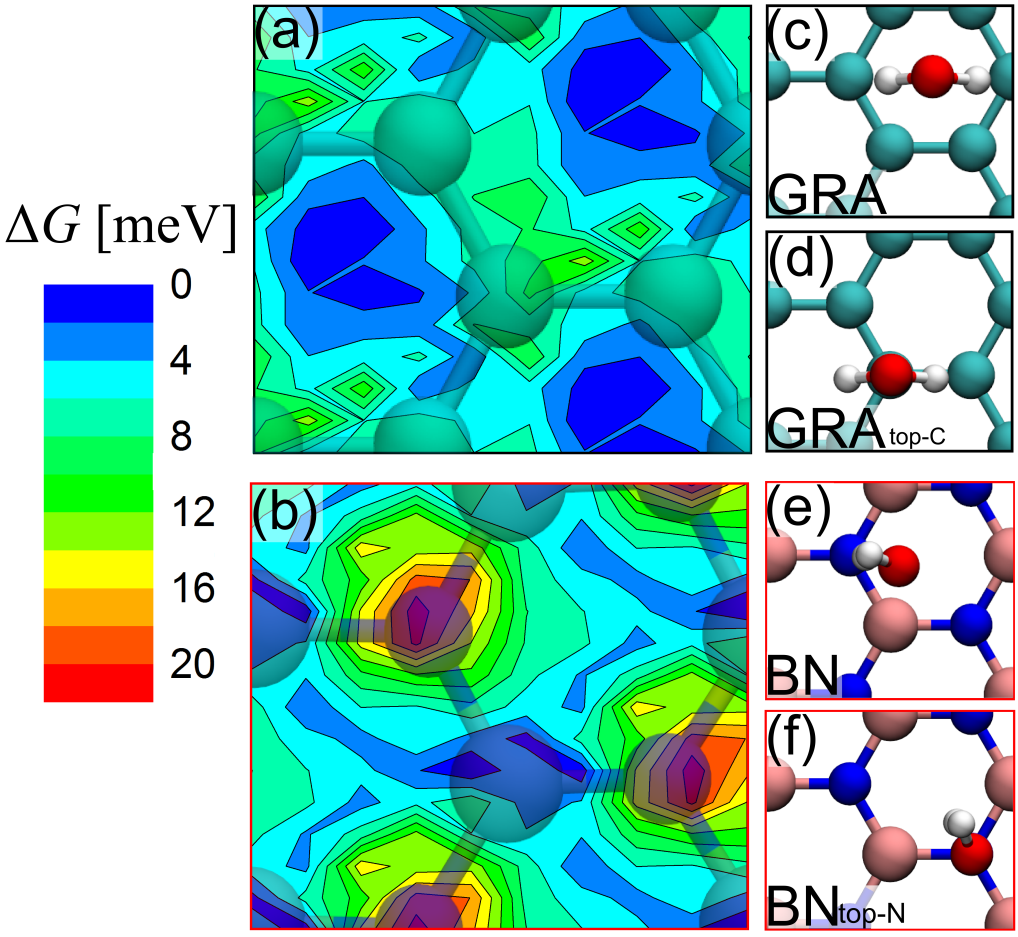

Figure 5.5: Free energy profile of water within the contact layer of the liquid projected onto the graphene (a) and BN (b) primitive unit cells. Although the free energy profiles are relatively smooth, a larger corrugation is present on BN and some differences are also observed in the topology. Transparent C and BN atoms are superimposed on the contour plots. Most stable (c) and less stable (d) configuration for a single water monomer adsorbed on graphene. Most stable (e) and less stable (f) configuration for a single water monomer adsorbed on BN. Only a small part of the unit cells used for the calculation of the monomer adsorption calculations is shown in figures (c) to (f).

of water within the contact layer at a point (x, y) projected onto the primitive graphene and BN unit cells. A similar approach based on the 2-D spatial probability distribution function has been used previously to under-

stand water slippage on model MgO surfaces [202]. Fig. 5.5 illustrates the free energy profiles resulting from this analysis. We notice the very small energy scale within k_BT at room temperature indicating a mobile contact layer. Although, as we have seen the average liquid structures in the two systems are very similar, the free energy profiles for the motion of water in the contact layer exhibit some clear differences. First, the free energy minimum on graphene is around the hollow site with the maximum around the top-C site, in agreement with previous work [150]. The minimum on BN is for the oxygens to sit around the B-site, as well as on the hollow site, while the maximum is on the N site. Second, and more importantly, the BN free energy profile (Fig. 5.5(b)) is more corrugated than that of graphene: the maximum corrugation of the free energy is only 13 meV on graphene, but it is 21 meV on BN. Although we are discussing very small energies, this $\approx 0\%$ increase in the corrugation is observed consistently in all our various AIMD simulations of these systems. As we now discuss, this increased corrugation is the main reason for the observed increase in the friction coefficient on BN.

It is interesting that such small energy differences, less than 10 meV can contribute to a three fold increase in the friction coefficient and it is worth looking into this more in detail. It is known that the leading term in the friction depends quadratically on the corrugation of the potential energy surface felt by the water in the contact layer ΔV, such that $\lambda \sim \Delta V^2$ (see *e.g.* [172, 203]). We can approximate the corrugation of the potential energy ΔV with the corrugation in ΔG as obtained from the maximum value in free energy profiles in Fig. 5.5, such that $\lambda \sim \Delta G^2$. To test the validity of this scaling relation we computed the ratio between the friction of water on

BN and on graphene, $\lambda_{BN}/\lambda_{GRA}$ and compared it with the ratio between the square of the free energy extracted from Fig. 5.5(a) and (b). From the ratio between the friction coefficients we obtain $\lambda_{BN}/\lambda_{GRA} = 2.7 \pm 0.8$. The corrugation of the free energy on BN is 21 meV, while it is 13 meV on graphene, such that the ratio $(\Delta G_{BN}/\Delta G_{GRA})^2 \approx 2.6$, is within the error of the ratio between the two values of the friction.

5.5.1 Connection with the monomer potential energy surface

The free energy corrugation depends on the atomic and electronic structure of the surface and on the H-bonds that form at a specific interface. It will differ but be related to the monomer potential energy surface. In an attempt to track down the difference between the corrugation of the two free energy profiles (and thus in the friction) to the nature of the water/surface interactions, we performed a series of structure relaxations at 0 K for a single water monomer on the two sheets. The most stable structure on graphene is for water on the hollow site with its dipole pointing down towards the sheet (Fig. 5.5(c)). On BN water preferentially adsorbs with the dipole moment parallel to the sheet and with one of the O–H bonds pointing towards the N atom (Fig. 5.5(e)).

Table 5.1 shows the adsorption energy of a water monomer on graphene and on BN for the two most stable structures. The adsorption energy E_{ads} is defined as $E_{ads} = E_{H_2O/sheet} - E_{sheet} - E_{H_2O}$, where $E_{H_2O/sheet}$ is the total energy of the composite system and E_{sheet} and E_{H_2O} are the total energies of the isolated sheet and water monomer in gas phase, respectively. Compared

Table 5.1: Adsorption energies (in meV) for a water monomer on graphene (GRA) and on BN from VASP (E_{ads}^{VASP}) and from CP2K (E_{ads}^{CP2K}) along with the adsorption energy computed at a less favourable adsorption site with the O atom of the water on the top C atom for graphene (GRA_{top-C}) and on the top N atom for BN (BN_{top-N}). Also shown is the decomposition of the adsorption energy obtained from CP2K into contributions from van der Waals (E_{ads}^{vdW}), local correlation (E_{ads}^{lc}), exchange (E_{ads}^{x}), electrostatic interactions (E_{ads}^{es}). The larger difference between the two adsorption energies on BN compared to graphene arises from the exchange and electrostatic terms (≈ 40 meV for BN against ≈ 10 meV for graphene), and not from the van der Waals and the local correlation which differ by only 3 meV at most.

	E_{ads}^{VASP}	E_{ads}^{CP2K}	E_{ads}^{vdW}	E_{ads}^{lc}	E_{ads}^{x}	E_{ads}^{es}
GRA	-148	-159	-253	-37	$+22$	$+109$
GRA_{top-C}	-138	-148	-254	-38	$+14$	$+130$
BN	-163	-171	-246	-41	-9	$+125$
BN_{top-N}	-130	-136	-249	-39	$+13$	$+139$

to graphene, BN binds water about 10 meV more strongly, with adsorption energies obtained with CP2K of -171 and -159 meV, for BN and graphene, respectively. A difference of ≈ 10 meV between the adsorption energy on BN and graphene is consistent with the results obtained from the VASP code.

Upon considering water monomer adsorption at less favourable sites (see Figs. 5.5(d) and (f)) we find that the potential energy surface of the water monomer on BN is more corrugated than that on graphene. As shown in Table 5.1, the adsorption energy difference between the most stable water structure on graphene and the less stable one is 11 meV/H_2O, while in the case of BN this difference is larger of 35 meV/H_2O. This indeed indicates that the potential energy surface of a water monomer on BN is more corrugated than that on graphene.

To understand why this is the case we performed the following decomposition of the adsorption energies obtained for the most stable adsorption

configurations and for the less stable ones:

$$E_{ads} = E_{ads}^{vdW} + E_{ads}^{lc} + E_{ads}^{x} + E_{ads}^{es}, \tag{5.3}$$

where E_{ads}^{vdW}, E_{ads}^{lc}, E_{ads}^{x} and E_{ads}^{es} the contributions to the adsorption energy coming from the van der Waals dispersion, the local correlation, the exchange and electrostatic interactions, respectively; here, E_{ads}^{es} is expressed as the sum of the contribution from the Hartree energy, the ion-ion term, and of the one-electron term coming from the core Hamiltonian (see Ref. [69]). The results of this decomposition are shown in Table 5.1. The most important point is that the larger difference between the two adsorption energies on BN compared to graphene arises from the exchange and electrostatic terms, and not from the van der Waals and the local correlation which differ by only 3 meV at most. This reveals that larger exchange and electrostatic interactions between water and the BN sheets are the origin of the increased corrugation. Overall, this explains the larger corrugation of the free energy on BN and thus the three-fold increase in the friction.

5.6 Final discussion

We have seen that, although the structures of the liquid films are very similar and the contact layer is mobile on both systems, slight changes in the water/sheet interactions may bear important consequences for the friction between water and the sheets. There is in general some uncertainty over the slippage of water on graphene obtained from force field MD, with values for the slip length between 1 and 80 nm [204]. The friction on graphene com-

puted from AIMD is $(10.3 \pm 3.3) \times 10^4\,\mathrm{N\,s\,m^{-3}}$, larger than the value obtained from force field MD of $\approx 3 \times 10^4\,\mathrm{N\,s\,m^{-3}}$ (see Fig. 5.4(b)). This is because the optB88-vdW functional predicts a larger corrugation of the free energy compared to the force field used [191]. Since optB88-vdW overestimates the absolute adsorption energy of a water monomer on graphene when compared to benchmark diffusion Monte Carlo and Random Phase Approximation results [205], we cannot expect optB88-vdW to capture the corrugation of the free energy with absolute precision. However, as explained earlier, because this functional successfully captures various other properties of water, graphite, BN and water at interfaces we expect it to predict the correct relative water/graphene and water/BN interaction strengths and hence the correct increase in the friction on BN. Since the increase in friction is not captured by force field molecular dynamics (see Fig. 5.4(b)), the findings here stress the importance of accounting for electronic structure effects when investigating transport properties at complex liquid/solid interfaces. Nevertheless, it is possible that improving the description of the force fields to include polarizable models and partial charges on B and N may reproduce the observed friction increase. For instance, it has been found that including polarization effects in force field molecular dynamics studies has an effect on the diffusion of liquid water on charged graphene [194].

Finally, there has been increasing interest in connecting wetting properties to the friction coefficient (see *e.g.* Ref. [201]) and a relation between the slip length and the contact angle has been found to hold for a wide number of liquid/solid interfaces. Previous work has suggested that this relation does not hold for water slippage on graphene [83]. Further, it has been found

that the partial slip boundary condition may hold also for water on hydrophilic surfaces [202]. Here, we have seen that the structure of liquid water on graphene and on BN is strikingly similar and previous *ab initio* work reported also contact angles of 86° and 87° on graphene and BN, respectively [179]. Yet, friction is about three times larger on BN, highlighting that a simple dependence on the wetting properties cannot be established for these two systems. Instead, we have demonstrated a dependence of the friction on the free energy of the water contact layer. In systems like graphene and BN, where the corrugation of the potential felt by the water is not directly proportional to the water/solid interaction strength, the free energy profile provides a closer estimate of the potential energy landscape corrugation. Possible other examples are carbon nanotubes, which like graphene, have been shown to depart from the scaling law that relates the friction to the water contact angle [83]; and most likely BN nanotubes and other van der Waals layered materials [206]. With the aim of designing nanofluidic devices which exhibit frictionless fluid transport, materials may be engineered to favour a smooth potential energy landscape independently of the fluid/solid interaction strength. In this manner for instance, the friction may be tailored whilst maintaining the same wetting properties. We have shown that because of subtle exchange and electrostatic interactions, friction is larger on BN. Limiting the magnitude of such interactions between the liquid and the substrate using for instance homopolar surfaces and avoiding the presence of H-bonds is beneficial for the design of smooth interfaces. Further, compressive or tensile stress can be applied to a substrate to favor a smooth contact layer [207].

5.6. FINAL DISCUSSION

In conclusion, we have reported on extensive *ab initio* molecular dynamics studies of liquid water on graphene and BN. In so doing we have tried to bridge the gap between the molecular structure and energetics of water on layered materials and the complex transport of water at the nanoscale fully from *ab initio* methods. A comparison between the two systems reveals that while the structure of the liquid film is very similar, slight differences in the water contact layer not related to the wetting properties of the interfaces give rise to a remarkably different water slippage on the two sheets. The three-fold friction increase on BN is induced by a larger corrugation of the energy landscape compared to graphene, because of more pronounced electrostatic and exchange interactions. Overall, this work paves the way for the study of transport properties in yet more complex liquid water/solid interfaces using *ab initio* methods. For example, systems where water is liable to dissociate or where ions, defects, or external electric fields are present could all be examined.

Chapter 6

Structure of the $TiO_2(110)$ photocatalytic interface

6.1 Introduction

Photocatalysis has seen a surge of research activity over the past ten years due to interest in water splitting [3], self-cleaning and self-sterilizing surfaces, and air and water purification [4]. Titania is the most studied photocatalyst and understanding its interaction with water is of great importance for the development of more efficient photocatalytic applications. Specifically, water on rutile $TiO_2(110)$ represents a model oxide interface for surface science studies aimed at better understanding fundamental features of photocatalytic interfaces [208, 209].

Despite the vast body of work on the water/$TiO_2(110)$ interface, there is still an open debate on one of the most basic questions for any water

adsorption study: does water adsorb in a molecular or in a dissociated state on a defect-free surface and under UHV conditions [161, 162, 210–213]? The answer to this question is of great importance because the photocatalytic activity of the interface depends on the concentration of OH radicals that may result (or not) from H_2O dissociation [214].

According to the most up to date photoelectron diffraction spectroscopy experiments, a fraction of water dissociates at coverages up to 1 ML [211, 212] (ML coverage is defined as one water per top five-fold coordinated Ti atom). However, there is new experimental evidence (from Geoff Thornton's group) coming from surface X-ray diffraction and photoelectron spectroscopy on the formation of a (2×1) overlayer made of terminal OHs (O_tHs), which suggests an overlayer of dissociated water [26]. Perhaps, more striking is the debate on the most stable water adsorption state from DFT, which started with the first report by Goniakowski and Gillan almost 20 years ago [215] and is not yet solved (see *e.g.* Refs. [162, 213]).

Despite the apparent difficulties in understanding the structure of water on defect-free TiO_2(110) under UHV atomistic studies on more realistic and complex interfaces have emerged. For instance, it has been shown that the presence of a liquid water film under aqueous conditions does not alter the level of dissociation [161, 162]. Instead, there is ample evidence for the existence of water dissociation channels associated with the presence of oxygen vacancies and with step edges along $\langle 1\bar{1}1\rangle$ [216–218]. Further, it has been proposed that water adsorption on TiO_2(110) is not affected by the presence of Ti-interstitials (Ti_{int}) [219]. In contrast to the case of water adsorption,

charge transfer from the defective substrate stabilizes the adsorption of O_2 by several eV/molecule [220]. So far, charge transfer has been reported as the only mechanism for the stabilization of the adsorbates in the presence of a surface with Ti_{int} or other point defects [217, 220].

In this Chapter, results are first presented from static DFT calculations using the PBE and the screened hybrid HSE06 functionals to provide insight into why modelling adsorption of water on defect-free TiO_2(110) remains challenging for theory. Secondly, we investigate the adsorption of H_2O, OH, and O_2 to understand the formation of a (2×1) O_tH overlayer observed in the new experiment in Ref. [26]. We suggest it arises from from a sequence of reaction steps involving the dissociation of O_2 on TiO_2(110) in the presence of defects, here represented by Ti_{int} and bridging OH (O_bH) groups. Finally, we propose a new mechanism for the stabilization of dissociated water that involves the presence of subsurface Ti_{int} and the competition between polaronic and dissociation-induced lattice distortions.

6.2 Computational details

Spin polarized static DFT calculations at zero K have been performed to investigate the adsorption of H_2O, OH and O_2 on stoichiometric and defective TiO_2(110) under UHV-like conditions using a similar approach as in the previous chapters (*e.g.* Section 4.2). We used the VASP code, with six valence electrons for oxygen ($2s^2 2p^4$) and twelve for titanium ($3s^2 3p^6 4s^2 3d^2$) and a cut-off of 400 eV for the plane wave expansion. We have employed a k-point mesh density of $4 \times 2 \times 1$ per primitive surface unit cell with the

Monkhorst-Pack scheme centered at the Gamma point [110]. We will show the results obtained using the PBE exchange-correlation functional, with PBE+U (U= 4.2 eV, applied to the $3d$ electrons of Ti) and with the hybrid functional HSE06. Both PBE+U and HSE06 have been shown to improve the band-gap of TiO_2 and to reproduce the $3d$ band-gap states on reduced as well as on hydroxylated surfaces [221, 222]. Throughout this study we have used the PBE lattice parameters, $a = 4.65$ Å and $c = 2.97$ Å, obtained from previous work [161]. The PBE lattice constant is only 0.3% larger than the HSE06 one (see *e.g.* Ref. [223]), so the effect of using the PBE value for the calculations with HSE06 should be negligible. We modelled adsorption on TiO_2(110) using cells of varying size ranging from (2×1) to (4×2). All the species were adsorbed only on one side of the slab, which is four tri-layers thick, while the other side was kept fixed at its bulk-truncated position. A dipole correction along the [110] direction has been used to avoid spurious electrostatic interactions arising from the asymmetry of the system along the direction of the vacuum, which is of $\approx$ 15 Å. This set-up has been shown to give rise to converged results for the adsorption of water on TiO_2(110) [161, 162].

6.3 Water adsorption on stoichiometric TiO_2(110)

We begin our discussion by showing the results for water adsorption on ideal defect-free TiO_2(110) at coverages (θ) in a range between 1/8 ML and 1 ML. Water adsorbs on TiO_2(110) by forming a covalent bond with the terminal five-fold coordinated Ti atom. Fig. 6.1 shows the possible configurations

for the adsorption of an isolated water monomer (θ = 1/8 ML) and of a water ML. Specifically, Figs. 6.1(a) and (b) show a water monomer in the dissociated (D) and molecular (M) states, respectively. In the D state a proton hops to a bridging oxygen atom resulting in the formation of an O_bH and of an O_tH, while in the M state the water adsorbed on the five-fold coordinated Ti atom is hydrogen bonded to the bridging oxygen. At ML coverage, besides the D and M states (shown in Fig. 6.1(c) and (e)), water can adsorb in a mixed molecular-dissociated mode. Specifically, water can adsorb in a (2×1) arrangement where one out of every two water molecules is dissociated to form a so-called partially dissociated (PD) overlayer (see Fig. 6.1 (d)).

Table 6.1 shows the adsorption energies (E_{ads}, defined in Section 3.4) of a water monomer and of a water monolayer along with the corresponding bond-lengths between the top-most Ti atom and the oxygen of the water (Ti–O_w), as obtained with the PBE, PBE+U and the HSE06 functionals. PBE predicts the water monomer to be more favourable in the M state than in the D state, with values for the adsorption energy of -0.71 eV/H_2O and -0.62 eV/H_2O respectively. On the other hand, PBE+U predicts that water is 50 meV/H_2O more favourable in the D state, with an adsorption energy of -0.98 eV/H_2O, compared to that of the M state of -0.93 eV/H_2O. While we did not compute the adsorption energy of a water monomer with HSE06, previous work (using the same surface model) showed that at a coverage of 1/2 ML the M state ($E_{ads} = -0.74$ eV/H_2O) is more stable than the D state ($E_{ads} = -0.54$ eV/H_2O) [161].

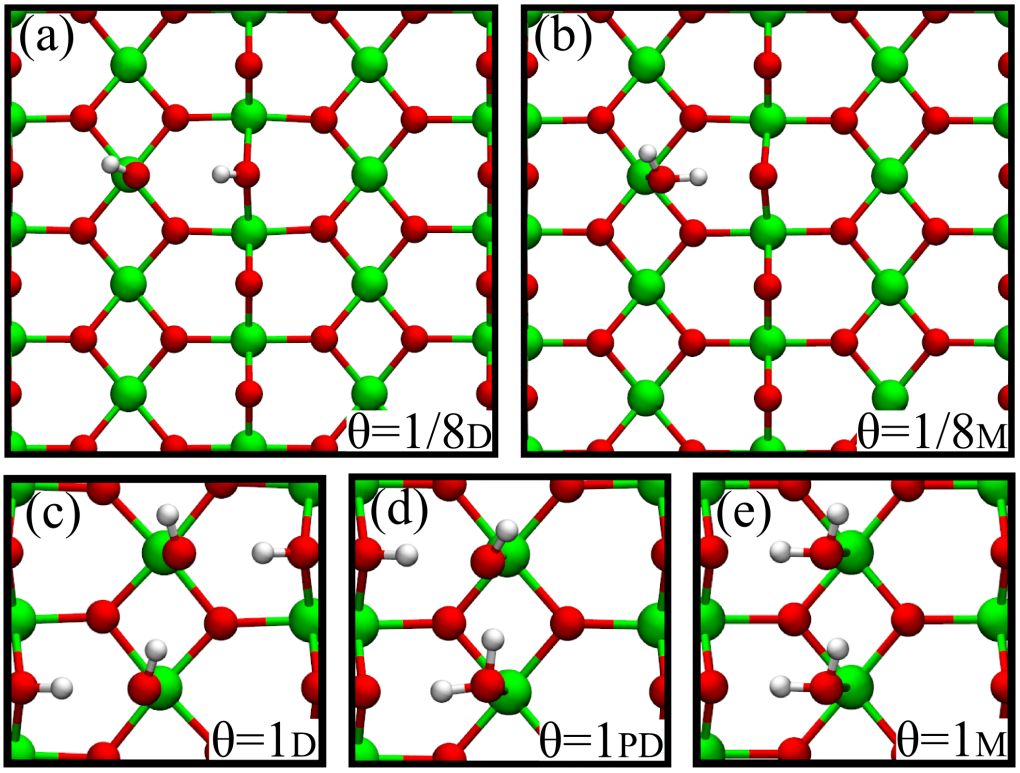

Figure 6.1: Structure of water on TiO_2(110) at coverages $\theta = 1/8$ ML and at $\theta = 1$ ML. Water adsorption at $\theta = 1/8$ ML in (a) dissociated (D) state and (b) molecular (M) state. Water adsorption at $\theta = 1$ ML in (c) dissociated state, (d) partially dissociated (PD) state and (e) molecular state. Titanium atoms are coloured green, oxygen in red and hydrogen in white.

At ML coverage there is at least one thing all three functionals agree on, that is the D state is significantly less stable (0.2 to 0.3 eV/H_2O) than the M and PD states. Both PBE and HSE06 predict that the most stable configuration is for water in the M state, with values for the adsorption energy of -0.78 and -0.85 eV/H_2O, respectively. Instead, the results obtained from PBE+U show that the M and the PD state are almost degenerate with only a difference of 30 meV/H_2O in favour of the PD state, in agreement with a

Table 6.1: Adsorption energy (E_{ads}) and bond-lengths between the top-most Ti atom and the oxygen of the water O_w (Ti–O_w) for water on TiO_2(110). The results shown have been obtained from different functionals in the case of monomer adsorption (at a coverage $\theta = 1/8_D$) and at monolayer coverage in the case of molecular ($\theta_M = 1$), partially dissociated ($\theta_{PD} = 1$) and fully dissociated ($\theta_D = 1$) states. The adsorption energies are expressed in eV/H_2O and bond-lengths in Å. The values for the adsorption energy and bond-lengths for the most stable state at $\theta = 1$ are in bold.

	$\theta = 1/8_D$		$\theta = 1/8_M$		$\theta = 1_D$		$\theta = 1_{PD}$		$\theta = 1_M$	
	E_{ads}	Ti–O_w	E_{ads}	Ti–O_w	E_{ads}	Ti–O_w	E_{ads}	Ti–O_w	E_{ads}	Ti–O_w
PBE	−0.62	1.83	**−0.71**	**2.26**	−0.43	1.93	−0.70	2.26[a] 1.99[b]	**−0.78**	**2.34**
PBE+U	**−0.98**	**1.86**	−0.93	2.21	−0.79	1.95	**−1.02**	**2.21[a] 2.02[b]**	−0.99	2.28
HSE06	-	-	-	-	−0.55	1.90	−0.77	2.22[a] 1.96[b]	**−0.85**	**2.29**

[a] bond-length between top-Ti and oxygen of molecular water
[b] bond-length between top-Ti and oxygen of dissociated water

recent report [213].

It is useful to compare the Ti–O_w bond-lengths with experimental data. Photoelectron diffraction experiments at a water partial pressure of the order of 10^{-9} mbar report a Ti–O_w bond length of 2.21 ± 0.02 Å [210], in quite good agreement with our calculated values for water in the M state, while the Ti–O_w bond for the D state is about 0.4 Å shorter. The bond-length for the M state predicted from PBE+U agrees very well with experiment, with a value of 2.21 Å. The PBE value for the M state instead is of 2.26 Å, 0.05 Å larger than the experimental one and slightly off the error bar. It comes somewhat as a surprise that PBE+U is in better agreement with experiment than PBE, although the D state is more favourable than the M state with PBE+U.

More recent photoelectron diffraction studies indicate that about 30% of the water molecules are dissociated at a coverage of 1/4 ML [211]. At ML coverage water participates in hydrogen bonding with neighbouring mo-

lecules and the resulting Ti–O_w bond lengths are elongated compared to lower coverages, as can be seen from Table 6.1. It is therefore better to compare the experimental value obtained at 1/4 ML with our results at 1/8 ML. The experimental Ti–O_w bond length for the fraction of dissociated water is 1.85 ± 0.08 Å, in good agreement both with the PBE+U and the PBE values for the D states obtained at 1/8 ML. Overall, the results at submonolayer coverage obtained from PBE+U seem to be in better agreement with experiment than PBE.

In a recent study a combination of photoelectron spectroscopy measurements and static DFT calculations was used to show that at ML coverage a fraction of water between 1/4 and 1/3 of a ML is dissociated [212]. While our PBE and HSE06 results indicate that water is more favourable in the M state than in the PD state, the PBE+U values suggest that a fraction of 50% of dissociated water is feasible. We thus performed additional calculations at 1 ML using PBE and PBE+U to verify whether indeed a fraction of water corresponding to 1/4 ML does dissociate. The adsorption energy in this new state obtained from PBE is of -0.73 eV/H_2O, which is only 50 meV/H_2O less stable than the M state shown in Table 6.1. The PBE+U value for the adsorption energy is -0.99 eV/H_2O, almost degenerate with the PD and M states. While with PBE we cannot discard for certain that at ML coverage a fraction of water up to 25% is dissociated, the PBE+U results indicate that a level of dissociation up to 50% is possible.

Our results already indicate that water on TiO_2(110) is a challenging system for DFT. To try and shed some light on such a complicated system,

we compare in Fig. 6.2(a) the values of the adsorption energy in the M and D states at coverages ranging from 1/8 to 1 ML as obtained with PBE+U. The figure shows that the D state is favoured over the M state at coverages

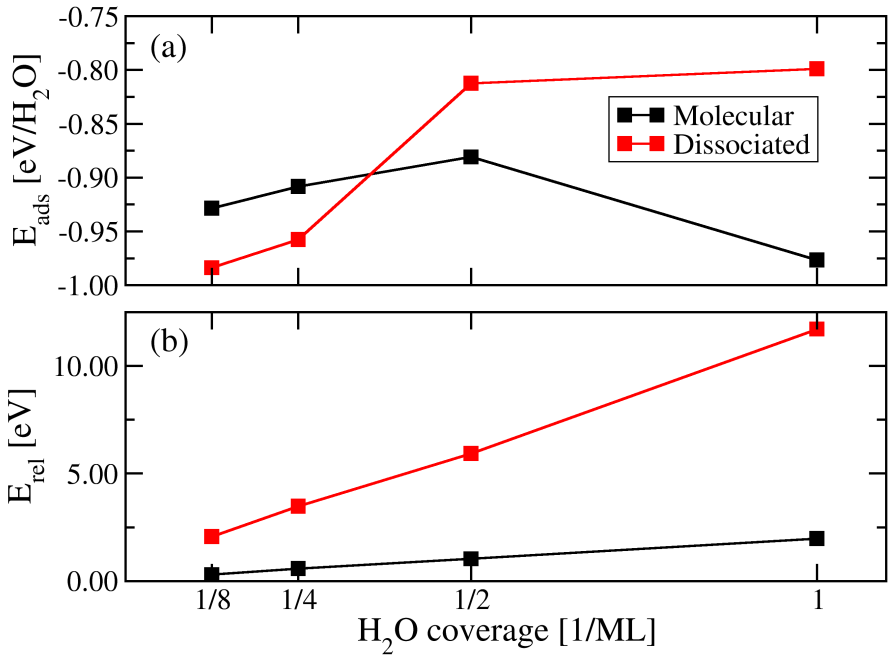

Figure 6.2: Adsorption energies (a) of molecular and dissociated water on TiO_2(110) for different coverages and (b) the relaxation energy (E_{rel}) of the surface in the two cases. It may be seen that the surface relaxation energy is significantly larger in the case of the dissociated water, which is why at coverages higher than 1/4 ML molecular adsorption is preferred. The results were obtained from PBE+U (U= 4.2 eV) using a (4×2) unit cell.

up to 1/4 ML. However, as the coverage is increased the D state becomes progressively less stable, until at a coverage $\geq$ 1/2 ML the molecular adsorption is favoured. In general water adsorption becomes less favourable as the coverage is increased, except for the M state at ML coverage. At ML

coverage the M state becomes more stable than at lower coverages because of the formation of a hydrogen bond between molecules about 2.9 Å from each other.

We now illustrate that as the coverage is increased, water dissociation produces a much larger distortion of the TiO_2(110) lattice than water in the M state, which is why molecular water is favoured at coverages $\geq 1/2$ ML. We plot in Fig. 6.2(b) the surface relaxation energy which is defined as the difference between the energy of the relaxed TiO_2(110) slab (E_{surf}) and that of the unrelaxed surface without the adsorbates (E_{surf}^{unrel}), namely $E_{rel} = E_{surf} - E_{surf}^{unrel}$. It can be seen that the cost to distort the lattice arising from dissociation rises from $\approx$ 2.0 eV to more than 10.0 eV per unit cell at ML coverage. The increase is much more modest in the case of molecular adsorption, with values going from $\approx$ 0.3 eV to just below 2.0 eV. This clearly explains why a fully dissociated overlayer is not feasible at coverages larger than about 1/4 ML.

Although the scattering of our results in Table 6.1 demonstrates that this system is very challenging for theory, we can provide some guidelines to improve its description from a modelling point of view. Firstly, we have seen that the relative stabilities between the M and D states at various coverages depend strongly on the surface relaxation energy. In the case of water dissociation, pronounced inner lattice distortions of up to 0.3 Å extend up to 2 tri-layers towards the bulk and provide a significant contribution to the overall adsorption energy (see Fig. 6.2(b)). Therefore, it is crucial to use a model for the TiO_2(110) which is thick enough to encompass such large

relaxation effects. In the case of an asymmetric slab model (as the one used here) where water is adsorbed only on one side, it has been demonstrated that using four tri-layers is enough to give converged results on the relative stability of molecular versus dissociated adsorption [161]. It stands to reason that if water is adsorbed on both sides more tri-layers are needed. We regard as critical for any future study on the adsorption of water on TiO_2(110) to demonstrate that the adsorption energy is converged with respect to the thickness of the slab.

We note that even if the stability between in the M, D or PD states differs by only about $\approx$ 0.1 eV/H_2O, water adsorption on other transition metal-oxides where the M and D or PD states are almost degenerate are not as challenging for theory. The most prominent example is perhaps ZnO($10\bar{1}0$), where *e.g.* at ML coverage the PD state is more stable than the M state, independent of the functional or slab thickness, although the difference between the two states is of the same order as TiO_2(110) (see *e.g.* Chapters 3 and 4). Also on MgO(100) a proportion of water is known to dissociate, a result that is not apparently affected by the functional or slab model used (see *e.g.* Refs. [164, 165, 224, 225]). It is not as difficult for theory to describe water adsorption on these materials because there is a modest effect of the surface relaxation in contrast to TiO_2(110).

Secondly, whether water does dissociate or not at lower coverages also depends on the strength of the interactions between water and the surface as obtained from a specific exchange-correlation functional. For instance, PBE+U predicts stronger water/surface interactions than both PBE and

HSE06. This is why water dissociates with PBE+U, while it does not in the other two cases. Nevertheless, it is not straightforward to establish the reliability of the Hubbard-U method given the dependence of the results on the specific value of U [213].

It seemed so far that experiments were reaching a consensus over the level of dissociation on TiO_2(110) [211, 212]. Nevertheless, the experimental evidence for the formation of the (2×1) O_tH overlayer has changed this view [26]. We devolve our attention to try and interpret this new result in the following section.

6.4 Hydroxyl adsorption on TiO_2(110)

Very recent surface X-ray diffraction and photoelectron spectroscopy experiments suggest the formation of a (2×1) overlayer made of O_tHs instead of 1 ML of water molecules in a M or PD state [26]. Here, we investigate the stability of terminal O_tH groups on TiO_2(110) at various coverages in a range between 1/8 and 1 ML, where the (2×1) arrangement observed in the experiment corresponds to 1/2 ML.

We illustrate the results of this analysis in Fig. 6.3. At each value of the coverage we find the most stable state of the O_tH species on TiO_2(110) and we compute the adsorption energy using as reference systems OH species in gas phase and a clean TiO_2(110). There can be essentially three different scenarios for the adsorption of O_tH groups on TiO_2(110) depending on the charge of the composite system, on that of the reference O_tH in the gas phase

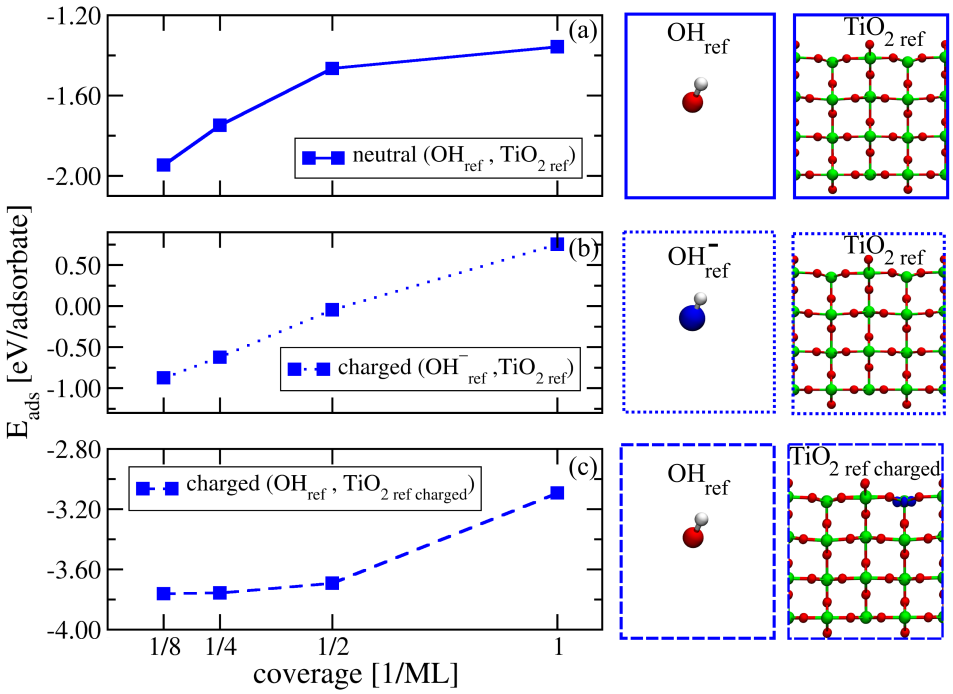

Figure 6.3: Adsorption energies of OH species on TiO_2(110) as a function of coverage for different charge states of the composite or reference systems. In (a) both the composite and the reference systems (labelled OH_{ref} and $TiO_{2\,ref}$) are neutral. In (b) and (c) the composite system is charged and in (b) the reference states are a charged OH (OH^-_{ref}) and a neutral surface ($TiO_{2\,ref}$), while in (c) they are a neutral OH (OH_{ref}) and a charged surface ($TiO_{2\,ref\,charged}$). Snapshots of the reference systems and their charges are shown on the right of the graphs. The electron density for the OH^-_{ref} and for the $TiO_{2\,ref\,charged}$ is in blue and in the specific case of $TiO_{2\,ref\,charged}$ we show one excess electron. The surface is modelled using a (4×2) unit cell and PBE+U, with U= 4.2 eV.

and of the clean TiO_2(110). In Fig. 6.3(a) we concentrate on the case where the overall system is neutral using as reference states an OH radical in the gas phase and a neutral clean TiO_2(110), referred to in the figure as OH_{ref} and $TiO_{2\,ref}$, respectively. The plot shows that OH radicals bind strongly at 1/8 ML with an adsorption energy of about -2.0 eV/adsorbate and that as the coverage is increased adsorption becomes progressively less stable with a value

of about −1.4 eV/adsorbate at 1 ML. Adsorption becomes less favourable as the coverage increases because of pronounced lattice distortion upon forming O_tHs, as observed in Fig. 6.2(b) for the case of water dissociation.

Fig. 6.3(b) instead, illustrates the adsorption of OH species on an overall charged system, using a charged OH and a neutral TiO_2(110) as reference states. It can be seen that it becomes less favourable to adsorb OH^- on a neutral TiO_2(110) as the coverage increases, until at coverages > 1/2 ML their adsorption even becomes unstable.

Finally, in Fig.6.3(c) we show the results for a charged system where we model the adsorption of OH radicals on a charged surface, that is with a neutral OH and a charged TiO_2(110) slab ($TiO_{2\,ref\,charged}$) as reference systems. OH radicals bind very strongly on a charged TiO_2(110) with an adsorption energy that stays constant around −3.8 eV/OH at coverages up to 1/2 ML. At ML coverage there is a steep increase and the OH adsorption becomes significantly less stable with a value of about −3.0 eV/OH.

The trend observed in Figs. 6.3(a) and (b) is similar, suggesting that the surface relaxation effect is the reason for the progressive destabilization over the adsorption of both OH^- and OH radicals on a neutral surface as their coverage increases. Because the OH radical is more electronegative than the OH^-, adsorption of an OH radical is overall stronger. On the other hand, the scenario in Fig. 6.3(c) is somewhat different. In this case the very strong binding arises from the charge transfer from the surface to the more electronegative OH species (see *e.g.* Ref [220]). The increased stabilization caused by charge transfer is contrasted by the surface relaxation effects that

tend to destabilize the adsorption of OHs as the coverage increases above 1/2 ML.

Overall, the scenario presented in Fig. 6.3(c) is the most plausible one to explain the recent experimental data. It shows that indeed an overlayer of 1/2 ML of O_tHs in a (2×1) arrangement is feasible, assuming that adsorption occurs on a charged substrate. This is a sound assumption given the large body of work on the presence of excess $3d$ states in TiO_2 arising from point defects (see *e.g.* Ref. [214]).

6.5 Hydroxyl formation on defective TiO_2(110)

We address now the question as to how the (2×1) overlayer of O_tH can form, given that there is no abundance of OH radicals in the environment and that the samples are dipped in water [26]. The results in Fig. 6.3(c) have hinted at the role of a charged surface and therefore the presence of point defects. However, it has been demonstrated that charges arising from defects do not play a significant role on the adsorption of water because water has a low electronegativity [220, 226]. Instead, O_2 is highly electronegative and experimentally it is possible for adventitious O_2 from the environment to participate in reaction processes to form an overlayer of O_tHs.

Through an extensive series of calculations we have found that the most plausible mechanism for the formation of a (2×1) O_tH overlayer involves O_2 dissociation on TiO_2(110) which has point defects, consisting of O_bHs and subsurface Ti_{int}. Specifically, in Fig. 6.4 we show a series of potential energy diagrams for the dissociation process of O_2 on a hydroxylated TiO_2(110) at

different concentrations of Ti_{int} using both PBE+U and HSE06.

It can be seen from Fig. 6.4(a) that without any Ti_{int} the adsorption of O_2 or of a peroxy OOH species is ≈ 1.0 eV more stable than the dissociation to O_tH. The adsorption of O_2 or of the peroxy species is stabilized by the charge transfer of excess electrons provided by the bridging hydroxyls, without which O_2 adsorption would be unfavourable (see *e.g.* Ref. [220]). Nevertheless, the concentration of the excess electrons is not large enough to allow for dissociation of O_2 to O_tHs.

On the other hand, at a concentration of Ti_{int} corresponding to 1/4 ML there are enough extra electrons that can be transferred to the adsorbates to stabilize the formation of O_tHs. This can be seen in Fig. 6.4(b), where O_2 dissociation to O_tHs is about 2.0 eV more stable than molecular adsorption or that of OOH species. Further, at this concentration a minimum of the potential energy is clearly visible corresponding to the (2×1) overlayer of O_tHs. Indeed, a (1×1) and a (2×2) overlayer of O_tH are 0.4 eV and 1.0 eV less stable than the (2×1) overlayer, respectively.

Finally, in Fig. 6.4(c) it can be seen that the dissociation to O_tHs is about 3.0 to 4.0 eV more stable than the adsorption of molecular oxygen or of the peroxy. Only, this time the (1×1) and the (2×1) overlayer are almost degenerate as they differ by less than 0.1 eV. The reason why a minimum in the potential energy appears in the case of a Ti_{int} concentration corresponding to 1/4 ML while it does not at the larger concentration of 1/2 ML has to do with a balance between the repulsive interactions due to the lattice distortion and to the energy gain upon charge transfer. At a

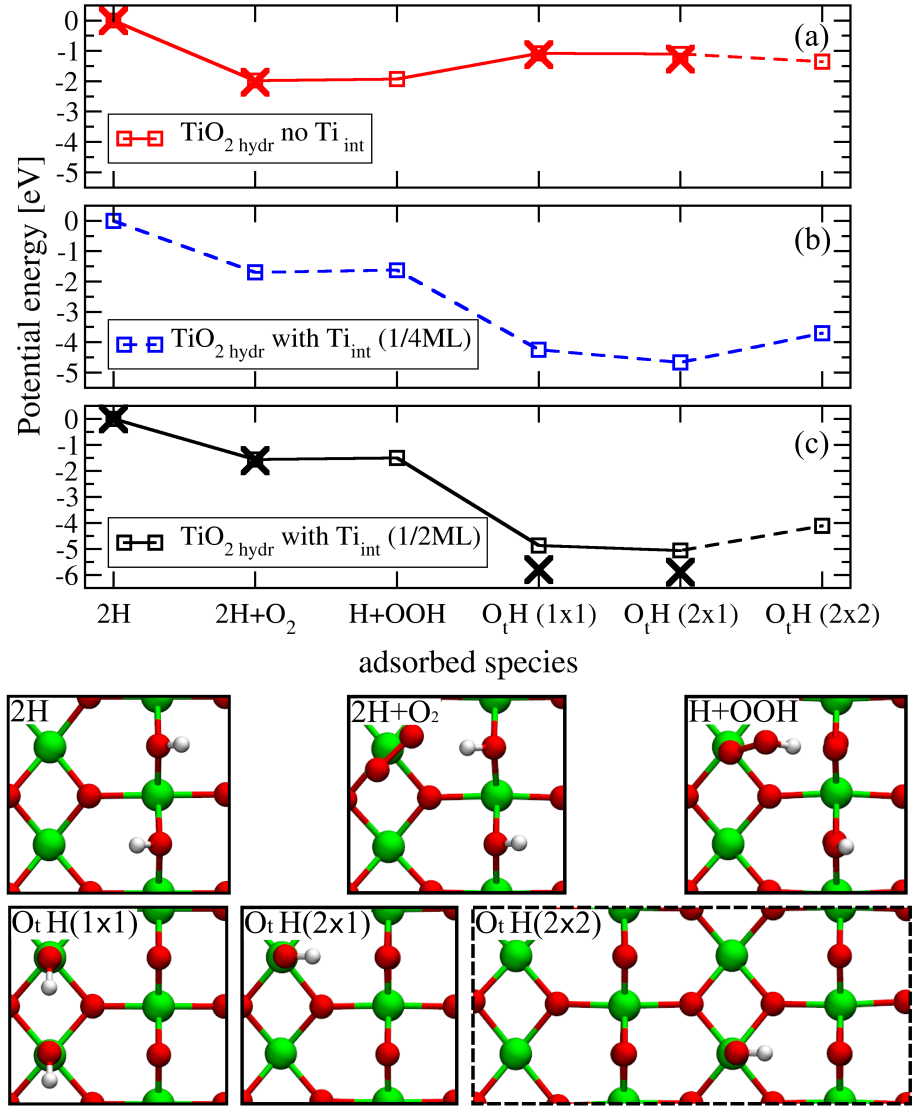

Figure 6.4: Potential energy diagram of O_2 adsorption and dissociation to terminal hydroxyls (O_tH) on a hydroxylated TiO_2(110) surface ($TiO_{2\,hydr}$) (a) without Ti-interstitials (Ti_{int}) and with a concentration of interstitials corresponding to (b) 1/4ML and (c) 1/2ML. The energy zero corresponds to the initial hydroxylated surface. Without interstitials (a) the adsorption of O_2 or of a peroxy group (OOH) is more favourable than O_tH adsorption. At a concentration of Ti_{int} corresponding to 1/4ML (b) a (2×1) overlayer of O_tH is most favourable (0.4 eV more stable than (1×1)). At a concentration of 1/2ML (b) the $O_tH(1\times1)$ and the (2×1) overlayers are almost degenerate. Lines with squares refer to PBE+U calculations (U= 4.2 eV), while crosses were obtained using the HSE06 functional. All the reported results were obtained using a (2×1) unit cell, except those with the dashed lines where a (2×2) cell was used. Snapshots corresponding to the structures indicated by the x-axis are shown in the bottom.

concentration corresponding to 1/4 ML of Ti_{int} there are not just enough excess electrons that can be transferred to the O_tHs to stabilize 1 ML of O_tHs. On the other hand, in Fig. 6.4(c) there are enough excess electrons to in principle favour a (1×1) O_tH overlayer. However, at this defect concentration and at this O_tH coverage, the gain in energy coming from the charge is compensated by the large energetic cost coming from the distortion of the lattice (see Fig. 6.2(b) and Fig. 6.3(c)), such that overall the (1×1) and the (2×1) become almost degenerate.

The scenario presented in Fig. 6.4(b) most closely reproduces the experiment in Ref. [26]. We note that our concentration of Ti_{int} and O_bHs may at first seem too high compared to experiment in which *e.g.* a concentration of 1/10 ML of O_bHs has been reported. Nevertheless, water dissociation may give rise to additional O_bHs providing the source of extra protons to form O_tHs from O_2. Further, the interplay between H_2O and O_2 might yield reaction pathways similar to those found in Ref. [217], through which a (2×1) O_tH overlayer might form. Also, the adsorption of O_2 might favour the diffusion of Ti_{int} from the bulk towards the surface, providing the source of extra electrons to favour O_2 dissociation [227].

All these different factors could come into play and provide marginally different mechanisms for the O_tH formation. Here, we have identified the main requirements: i) the presence of a hydroxylated surface; ii) a sequence of reactions involving O_2 dissociation; and iii) the presence of excess electrons in the TiO_2(110) lattice provided by defects (here Ti_{int}) to stabilize the dissociation of O_2 to O_tHs via charge transfer. Although we did not

compute the activation barriers for the processes shown in Fig. 6.4, previous work on a hydroxylated TiO_2(110) has reported that the *e.g.* the barrier for the dissociation from an OOH to two O_tHs is small, ≈ 0.2 eV [217].

We have seen so far that the presence of defects is crucial for the stabilization of an O_tH overlayer. Also in Section 6.3 we have noticed that PBE+U predicts a fraction of water dissociation on the stoichiometric surface, while both the PBE and HSE06 functionals point against this possibility. The results from HSE06 should be more reliable because with the Hubbard-U method the relative stability of the M state over the D state can be altered by simply changing the value of U [213]. Therefore, in the next Section we explore the possibility of water dissociation induced by the presence of defects.

6.6 The role of Ti-interstitials on water adsorption

We investigate the role of Ti_{int} on the adsorption of water at 1 ML. Specifically, in Fig. 6.5 we compare the adsorption energy of water in the M and PD states at different concentration of Ti_{int} as obtained using the PBE and HSE06 functionals.

According to PBE (see Fig. 6.5(a)) the increase in Ti_{int} concentration destabilizes only slightly the adsorption of water in both the M and PD states. The M state is ≈ 0.1 eV/H_2O more stable than the PD state at all Ti_{int} concentrations from 0 to 1/2 ML. On the other hand, Fig. 6.5(c) shows the striking result from HSE06 that a change in Ti_{int} concentration alters

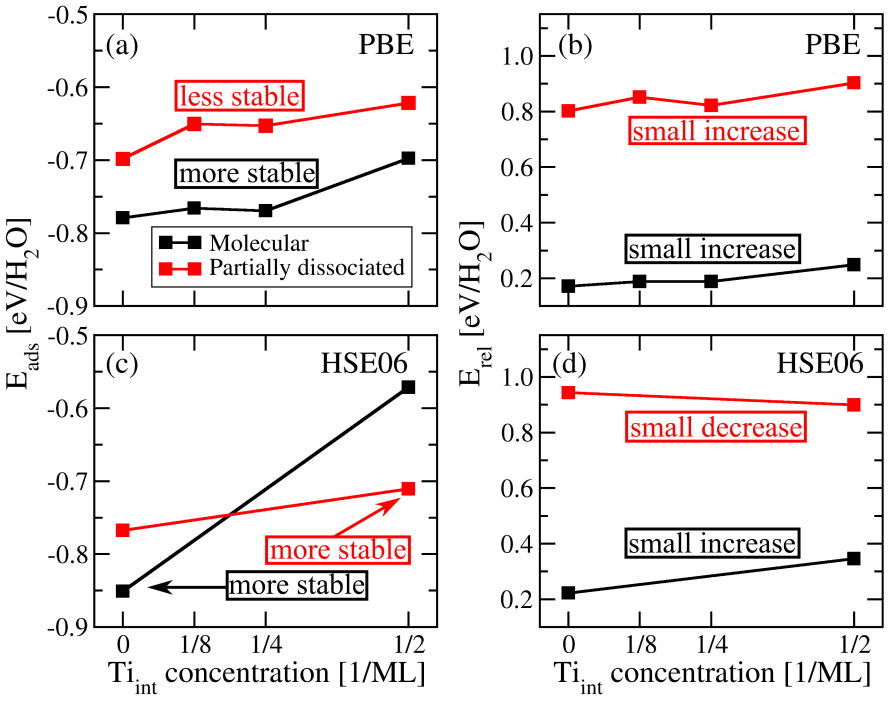

Figure 6.5: Adsorption energies of molecular and partially dissociated water on TiO_2(110) at monolayer coverage as a function of Ti_{int} concentration as obtained using the (a) PBE and (c) HSE06 functionals. Surface relaxation energies obtained with (b) PBE and (c) HSE06. Molecular adsorption is more stable with PBE at all Ti_{int} concentrations. The partially dissociated state becomes more stable than the molecular state with the HSE06 functional. Partially dissociated adsorption reduces the surface relaxation energy in (d) compared to the molecular adsorption.

the stability of the PD and M states. Indeed, without interstitials the M state is ≈ 0.1 eV/H_2O more stable than the PD state, but at a concentration of Ti_{int} corresponding to 1/2 ML the PD state becomes more stable with an adsorption energy of ≈ -0.7 eV/H_2O, compared to the value of -0.57 eV/H_2O for the M state.

We now rationalize the different behaviours of the two functionals in terms of the surface relaxation energy E_{surf} as we used before (see Fig. 6.2(b)).

Fig. 6.5(b) illustrates the surface relaxation energy with PBE for the two states, where it can be seen that there is only a very small increase of about 0.1 eV/H_2O across the range of Ti_{int} concentration with the E_{surf} for the M state being 0.6 eV/H_2O smaller than the one for the PD state. On the other hand, the HSE06 relaxation energy in Fig. 6.5(d) illustrates a different behaviour: E_{surf} for the M state increases from $\approx$ 0.2 eV/H_2O to 0.35 eV/H_2O, while it shows a decrease of about 50 meV/H_2O in the PD state. This overall change of about 0.2 eV/H_2O in favour of the PD state accounts for the change in the stability between the M and the PD state observed in Fig. 6.5(a).

The different behaviour observed in Figs. 6.5(b) and (d) raises the question as to why PBE and HSE06 predict different relaxation energies. We find that this has to do with the different way the two functionals describe the distortions induced by the Ti_{int}. Both functionals predict a large distortion induced by the interstitials. For instance, according to PBE at a Ti_{int} concentration of 1/2 ML, the most stretched Ti–O bond is about 2.74 Å long. This is much larger than the bulk Ti–O bond-length of about 1.96 Å. The PBE functional however, does not predict additional lattice distortions arising from the presence of excess electrons due to the interstitials. The HSE06 functional instead correctly captures these polaronic distortions arising from the localization of the excess electrons on Ti-3d states [228, 229]. For instance, the most stretched Ti–O bond with HSE06 is 2.84 Å, about 0.1 Å larger than the PBE value (the HSE06 bulk Ti–O bond-length is 1.91 Å). The different way the two functionals treat the polaronic distortions gives rise to the different behaviour observed in the surface relaxation energy plots

in Figs.6.5(b) and (d).

From this it is clear that the surface relaxation in the PD state as obtained from the HSE06 functional counterbalances the polaronic distortions, while this does not occur in the M state. This is why the PD state becomes more stable than the M state as the concentration of interstitials is increased. As an example of the compensating surface relaxation effect of water in the PD state, we compare in Fig. 6.6 the structure of the surface in the two cases. While the most stretched bond length in the case of M adsorption is 2.86 Å (Fig. 6.6(c)), in the PD state this bond is 0.3 Å less stretched, around 2.58 Å (Fig. 6.6(d)).

We stress that the change between the stability of the M and the PD state is due to the balance between the polaronic distortion and the distortion due to the adsorption of water in the PD state. Charge transfer effects, important for the stabilization of the O_tHs (see Section 6.5), do not play a role here again due to the low electronegativity of water [220, 226]. Indeed, the Bader charges on the adsorbates in the defective system change by a negligible amount ($\approx 0.02\,e$) compared to the case of stoichiometric adsorption.

The increase in the level of dissociation induced by the presence of interstitials may have important implications. First, the presence of O_tH introduces reaction channels important to photochemical processes [214]. Second, water dissociation might favour diffusion of bulk Ti_{int} towards the surface because of surface relaxation effects which compensate for the polaronic distortion induced by the interstitials. Also, interstitials produce $3d$ localized states appearing in the TiO_2 gap, and the presence of subsurface $3d$ electrons in

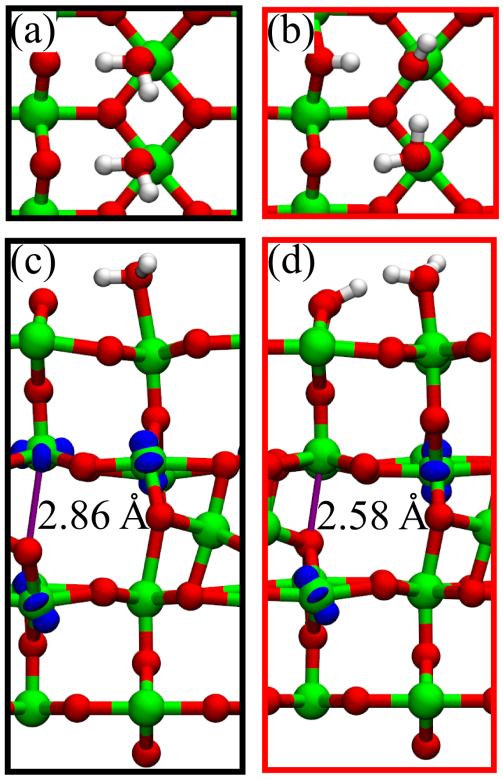

Figure 6.6: Structure of a water monolayer in the (a) M and (b) PD state on TiO_2(110) with a sub-surface Ti-interstitial as obtained using the HSE06 functional. Side view of water in the (c) M state and (d) PD state, where the interstitial atom along with the localized excess electrons can be seen. The excess electron density is shown in blue corresponding to a value of 0.2 e. A particularly stretched Ti–O bond is highlighted in purple and its bond-length is displayed. It can be seen that this bond is shorter in the PD state in (d), while it is longer in the M state in (d). Adsorption in the PD state counterbalances the polaronic distortion.

the gap may be crucial for the performance of photocatalytic application of TiO_2 [214]. Finally, with a sufficient proportion of sub-surface Ti_{int} the PD state can become more stable than the M state, and this could help to solve the discrepancy between theory and experiments on the level of dissociation.

We conclude this Section with a note of caution. We have seen in Section 6.3 that there is a very strong dependence on the simulation results on

the number of layers used to model the surface because of important surface relaxation effects. Although our model gives converged results for the adsorption of molecular versus dissociated water in a stoichiometric $TiO_2(110)$ model [161], the same may not be true in the presence of interstitials which produce such large lattice deformations. Careful tests against the number of layers, on the lattice constant and on the position of the Ti_{int} are all important to determine the validity of our results and they are currently ongoing. Particularly interesting will be the investigation of the transition from the M state to the PD state as a function of the concentration of the interstitials.

6.7 Conclusions

The surface science of $TiO_2(110)$ is as complicated as it is interesting. We have demonstrated that one of the underlying difficulties from theory in modelling water adsorption on the defect-free surface comes from the choice of a slab that is thick enough to account for pronounced inner lattice distortions. Another obvious difficulty is the choice of the exchange-correlation functional. For this purpose, more accurate calculations using the Random Phase Approximation, diffusion Monte Carlo or even Møller-Plesset perturbation theory would be desired.

Despite the inherent difficulties of DFT in modelling the surface chemistry of $TiO_2(110)$, useful insights have been provided into the recent experimental data that supports the presence of a (2×1) overlayer of terminal OHs [26]. We exclude that the (2×1) overlayer can result solely from H_2O adsorption and instead demonstrate that it can originate from dissociation of O_2 on to a

hydroxylated surface with subsurface Ti interstitials. We further investigated the role of Ti interstitials on the adsorption of water, showing that their presence increases the level of dissociation due to the competition between the polaronic distortion and the distortion induced by dissociating water.

Overall, while our calculations support the idea that water does not dissociate on the defect-free surface, we suggest new channels for the formation of terminal OHs, involving the presence of point defects such as bridging hydroxyls and Ti-interstitials. It would be interesting to see how doping of TiO_2(110) with *e.g.* surface Hs and Ti interstitials affects the concentration of terminal OHs and the TiO_2(110) photocatalytic activity.

Chapter 7

Conclusion

This thesis has focussed on understanding the structure and dynamics of water at a range of interfaces of current technological interest. Specifically, we have used static DFT and AIMD simulations to provide guidelines to help solving important problems relating to heterogeneous catalysis and power harvesting.

7.1 Summary

In Chapter 3 we have helped to solve a long standing debate concerning the structure of the ZnO($10\bar{1}0$) surface [88] by using exchange-correlation functionals that partially correct for the self-interaction in DFT (with the HSE06 functional) and that include van der Waals dispersion forces (with optB86b-vdW and optPBE-vdW). The clean ZnO($10\bar{1}0$) surface exhibits a modest relaxation with the top Zn lying below the O ion resulting in a tilting of about 7°. It is important to establish the microscopic details of the

surface relaxation because on that may depend the activity of industrial Al_2O_3/ZnO/Cu catalysts for the methanol synthesis [20]. We hope that in the near future higher order methods, such as quantum Monte Carlo or the random phase approximation, will be used to predict and design the structure of metal oxide catalysts. Quantum Monte Carlo studies on MgO(001) look promising [43], but oxides belonging to the transition metal series are certainly more challenging. In that chapter we also confirmed that at monolayer coverage a fraction of water equal to 50% is dissociated on ZnO($10\bar{1}0$), as obtained using HSE06 and van der Waals density functionals. The calculation of a small barrier to dissociation of the order of a few meV/H_2O suggested the existence of interesting proton dynamics under ambient conditions.

Results from AIMD simulations in Chapter 4 showed that fluctuations induced by the liquid water film make proton hopping extremely facile at the liquid water/ZnO($10\bar{1}0$) interface. In presence of the liquid phase (*i.e.* close to ambient conditions) the rate of proton transfer on ZnO($10\bar{1}0$) is $\approx$ 10 times larger compared to a water monolayer on the surface (that is close to ultra-high vacuum conditions). This result suggests that the activity of catalysts may in general increase under wet conditions. Important effects are therefore expected in electrochemical interfaces, *e.g.* in water splitting and fuel cells. DFT is establishing itself as a method to screen catalysts in gas-phase reactions [18], but screening catalysts under wet conditions poses additional challenges. One of the main problems is to be able to sample efficiently phase space for systems of hundreds to thousands of atoms and for several materials. Accelerated AIMD techniques can be in principle used for this purpose. Besides the sampling of phase space, additional problems that

have to be taken into account are the presence of electric fields and dissolved ions, both important in electrochemistry. These problems are increasingly being tackled (see *e.g.* Refs. [230, 231]).

In Chapter 5 we investigated liquid water transport at the interface with carbon and boron nitride nanostructures. The two most important results have been obtained by comparing the structure and friction of liquid water in contact with graphene and with an hexagonal boron nitride sheet: firstly, we demonstrated for the first time that a converged liquid/solid friction coefficient can be obtained from AIMD; secondly, there is a striking difference in the friction between water on graphene and water on BN, although the structure of the liquid is almost identical on the two sheets. The friction is ≈ 3 time larger on BN than on graphene because of the greater corrugation of the energy landscape on BN arising from stronger exchange and electrostatic interactions. We have suggested possible ways to modify the free energy of the contact layer so as to tailor liquid/solid friction. We hope this work will stimulate the study of friction at ever more complex liquid/solid interfaces using *ab initio* methods, directed towards the design of nanomaterials with desired friction properties. Osmotic gradients and electric fields are used to generate electric currents and liquid flow in energy applications where nano-membranes are used in aqueous solutions [21]. It will be interesting to use AIMD to explore mass as well as charge transport in nano-membranes to improve their efficiency for power harvesting.

Finally, in Chapter 6 we have made important advances in the understanding of water on rutile TiO_2(110). We have first traced down the prob-

lems of modelling water adsorption on TiO_2(110) to a delicate balance between water/surface interactions and surface relaxation effects. We have then explored the adsorption of H_2O, OH and O_2 on TiO_2(110) to interpret the recent in-house surface X-ray diffraction results from Geoff Thornton's group [26]. We find that an OH (2×1) overlayer arises from the dissociation of O_2 on a TiO_2(110) surface with point defects. A competition between charge transfer effects and surface relaxation effects is at the heart of the found mechanism. Using the HSE06 functional, we also find that sub-surface Ti interstitials favour the stabilization of a fraction of dissociated water. This arises from a competition between the surface relaxation due to water dissociation and the lattice distortion due to a polaron. Tests with different interstitials concentrations and different number of layers will tell if the presence of point defects effectively alters the stability of dissociative and molecular water adsorption. In this work we have bridged the gap between experiments under realistic conditions of the photocatalytic TiO_2(110) interface and the DFT studies on the surface chemistry of TiO_2(110). The use of more accurate methods and slab models will further narrow the gap between theory and experiments on this system. We hope that the use of techniques beyond DFT, such as GW and time-dependent DFT will be increasingly used to predict optical excitations in the photocatalytic TiO_2(110) interface to eventually provide guidelines so as to widen the light absorption spectrum of photoelectrochem-

ical cells based on TiO_2(110) [67, 232–234].

7.2 Outlook

In this final section we discuss possible developments in the modelling of liquid/solid interfaces using atomistic simulations, and in particular those based on density functional theory. Here, we propose developments that we believe feasible over about a ten years range. The main task is to perform more efficient and more accurate AIMD simulations of liquid/solid interfaces. There are three main goals that can be attained by performing faster and more accurate calculations: first, to improve the efficiency of processes occurring at liquid/solid interfaces, requiring high throughput screening of materials or the discovery of new materials; second, to explain processes that are not currently understood at the microscopic level, which may need the use of more accurate and/or efficient techniques; third, to explore properties of materials emerging from the use of more accurate methods and/or larger systems which are feasible to simulate only employing faster techniques than those currently available. While all three goals are of utmost importance, we discuss on the first one since the subjects covered in this thesis are most closely directed towards its achievement. However, an important example where the increase of speed and accuracy of computer simulations may improve current understanding of processes at liquid/solid interfaces concern for instance the problem of heterogeneous ice nucleation (see *e.g.* Ref. [235]).

In this thesis we focussed on three different water/solid interfaces. When studying each system our efforts were directed towards the understanding of

important problems at microscopic scales, to provide guidelines to improve the performance of energy applications and in heterogeneous catalysis. Specifically, the main goal of the study of proton transfer at the water/ZnO interface was devoted to improve the efficiency of current fuel cells and to develop cheaper fuel cell catalysts. Further, the study on the chemistry of TiO_2(110) was directed towards the development of more efficient photoelectrochemical cells for water splitting. Finally, we performed the work on water slippage at the water/graphene and water/BN interfaces with the idea of improving existing membranes for water desalination and for power harvesting from salinity concentration gradients [21].

We now wish to expand on each of these topics. We can start from the problem of designing more efficient and cheaper fuel cells. The main challenges for fuel cells are to find catalysts to split H_2 and O_2 that are more efficient and cheaper than current ones, mostly based on Pt, and that are resistant to poisoning by external impurities, mostly CO.

How can molecular simulations be used to improve the efficiency of fuel cells? There have already been significant developments on the understanding of the activity of transition metals and alloys for heterogeneous catalysis. This has led to the use of high through screening of materials using DFT calculations to design more efficient and cheaper catalysts. [18]. However, in fuel cells and electrochemistry in general, the presence of a liquid phase in contact with the surface, which is charged, poses additional challenges. Further, catalysts in contact with an electrolyte are often in a corrosive environment. This means that besides looking for catalysts that present a high

activity in the presence of an electric field and in contact with a liquid phase, one has to search for catalysts and electrolytes that are stable when they are in contact with each other.

Starting from the success of DFT in the design of catalysts for reactions under UHV conditions, we can envisage a future where we may use high throughput AIMD simulations of liquid/solid interfaces to identify efficient, stable and cheap catalysts that can be used in fuel cells or other electrochemical cells. It seems that the theoretical framework to address issues concerning the alignment of the electronic energy levels at liquid/solid interfaces has been laid out [236], as well as the problem of explicitly including the presence of electric fields into condensed phase AIMD simulations [230]. In practice, the HSE06 functional or other similar hybrid functionals describe the correct alignment of the electronic levels with respect to vacuum at model liquid/solid interfaces such as liquid water on TiO_2 or liquid water on Pt [236]. The use of hybrid functionals in AIMD simulations of liquid/solid interfaces seems therefore promising for the application to electrochemical interfaces. Further, modelling the explicit presence of electric fields in condensed phase requires the use of the modern theory of polarization expressed in terms of Berry phases (see Ref. [237] for a review). Recently this approach has been used to describe the dissociation of liquid water under an applied electric field with AIMD [230], opening the way to investigating more complex processes occurring at electrochemical cells where external electric fields are present.

We can imagine that in a foreseeable future we will be able to run a very large number of AIMD simulations of different liquid/solid interfaces to find

catalysts used for the hydrogen-evolution reaction that are more efficient, cheaper and more stable than those currently available. This will require to determine descriptors that include the cost of a given material, its activity and stability against corrosion, in a similar way as in the case of reactions of molecules on surfaces [18]. At present, the most challenging task seems the capability to perform high throughput AIMD simulations of liquid/solid interfaces, especially using hybrid functionals. However, recent developments have allowed to perform efficient hybrid functional DFT calculations for several hundreds to thousands of atoms [238, 239], and the first AIMD simulations of liquid/solid interfaces using hybrid DFT have emerged [240]. Although performing high throughput screening of liquid/solid interfaces using brute-force AIMD simulations may be a possible route to follow, one of the problems of brute-force AIMD is that important reaction steps may not be sampled. A possible alternative solution would be to apply accelerated sampling techniques to explore more efficiently phase space (see *e.g.* Ref. [139] to see how metadynamics has been used to understand how salt dissolves in water).

The problem of designing better photoelectrochemical cells for water splitting is closely related to that of designing better fuel cells, and we discuss this issue next. The interaction of light with matter adds an additional complexity to the case of thermal heterogeneous catalysis. In order to be able to design efficient photocatalysts using molecular simulations, for *e.g.* water-splitting, additional factors or descriptors have to be taken into account compared to the case of designing fuel cells, where we included a material's cost, its activity and stability against corrosion. Specifically, we have to include how light

absorption affects the activity of a given reaction.

In the case of TiO_2, which is *the* model photocatalyst, there is a vast body of work on how to modify the optical properties of TiO_2 surfaces and on the reaction mechanisms involving photoinduced electron-transfer events (see *Ref.* [214]). Specifically, one of the main goal for TiO_2 photocatalysis is to tune the band-gap to favour light absorption in the visible range, so that photoinduced electron transfer and the related reaction processes occur also for less energetic photons than *e.g.* UV ones. With the aim of using computer simulations for the design of photoelectrochemical cells one should try to optimize the following factors: i) the electronic band structure of a given interface to favour light absorption in the visible range; ii) the activity of photoinduced electron tranfer reactions that often involves the transport and/or trapping of charge carriers; iii) the stability of the interface with respect to external poisons (*i.e.* its resistance to photocorrosion); iv) the cost of the materials and the process to produce the given interface (perhaps at a later stage).

We can imagine that in the future we will be able to use a combination of AIMD and of excited states simulations such as GW or time-dependent DFT to perform a high-throughput screening of materials and interfaces in order to optimize the efficiency of photoelectrochemical cells for *e.g.* water splitting or for electrical current generation, such as in dye-sensitized solar cells. In order to optimize the points i) to iv) above we could perform AIMD simulations of liquid/solid interfaces to sample the phase space and investigate the electronic structure and stability of the interface, and on top of that

use excited states calculations on selected structures to investigate electron transport and electron transfer reactions.

Finally, in Chapter 5, we explored the nanofluidic properties of water on C- and BN-nanostructures with a view to design better desalination membranes or membranes for osmotic power harvesting. We focus for example to the problem of designing more efficient and stable membranes for osmotic power harvesting and stable using molecular simulations and specifically AIMD. Recently Siria *et al.* have reported on large electronic currents generated from salinity gradients through BN-nanotubes [21].

We can foresee in the future we will be able to run a very large number of AIMD simulations (possibly also using enhanced sampling techniques) with membranes made of a nanotube separated by two reservoirs of different salinity concentration gradients as done in the experiments [21] and to measure directly the osmotic current. It would then be possible to optimize the osmotic current using AIMD simulations. Factors that affect the osmotic current are the geometry and type of tube, the concentration and type of adsorbed species on the tube that produce the electric double layer and the salt concentration in the liquid solution. We may perform high-throughput AIMD simulations of nanofluidic membranes to optimize all these factors and generate a high electrical current. Further, we have to ensure that a given membrane with a certain concentration of surface adsorbates and at a given pH concentration is stable. Therefore, additional work may involve performing high-throughput DFT structure optimization or AIMD simulations to investigate the stability of the membrane will be required.

7.2. OUTLOOK

On the whole, we have explored the microscopic properties of a few water/solid interfaces. We have touched upon several areas of liquid water/solid interfaces, with problems going from electrochemistry, to heterogeneous catalysis and photocatalysis, to water transport and nanofluidics. By often going beyond the use of standard computational techniques and density functional approximations we provided useful insights into the structure and dynamics of water on solid surfaces. We believe that we are experiencing a shift where the predictive power of atomistic simulations will allow the design of catalysts also in wet conditions to improve the efficiency of fuel cells and of photoelectrochemical cells, and also of more efficient nanofluidic membranes for power harvesting. We hope to have contributed with our work to proceed in this direction and that in the future high-throughput AIMD simulations will be routinely used for a computational design of liquid/solid interfaces for heterogeneous catalysis and energy applications.

Appendices

Appendix A

Further details on proton hopping at the water/ZnO interface

Further details on the calculations of the dissociation barriers at ML coverage.

A.1 Dissociation barrier at ML coverage

In the Chapter 4.4.3 we reported results for the water dissociation barrier as a function of intermolecular distance. The energy profiles for each of these dissociation reactions are shown in Fig. A.1. Specifically what we report are energy profiles as a function of the O_w-H distance for specific values of the O_w-O_d distances (as defined in Section 4.4.3). In order to extract the dissociation barriers we performed AIMD simulations at 10 K in the NVT

ensemble with constraints on O_w-H and on O_w-O_d. Single point total energy calculations have then been performed on the structures resulting from the AIMDs. ΔE refers to the total energy difference from the initial (molecular) state obtained from these. Each line refers to a different value of the O_w-O_d distance. It may be seen that for O_w-$O_d \lesssim 3.2$ Å the dissociation process is barrierless, whereas the barrier increases from approximately 1 meV/H_2O to 10 meV/H_2O upon going from 3.2 to 3.4 Å. The barriers as a function of the O_w-O_d distance (Fig. 4.7) have been extracted from Fig. A.1.

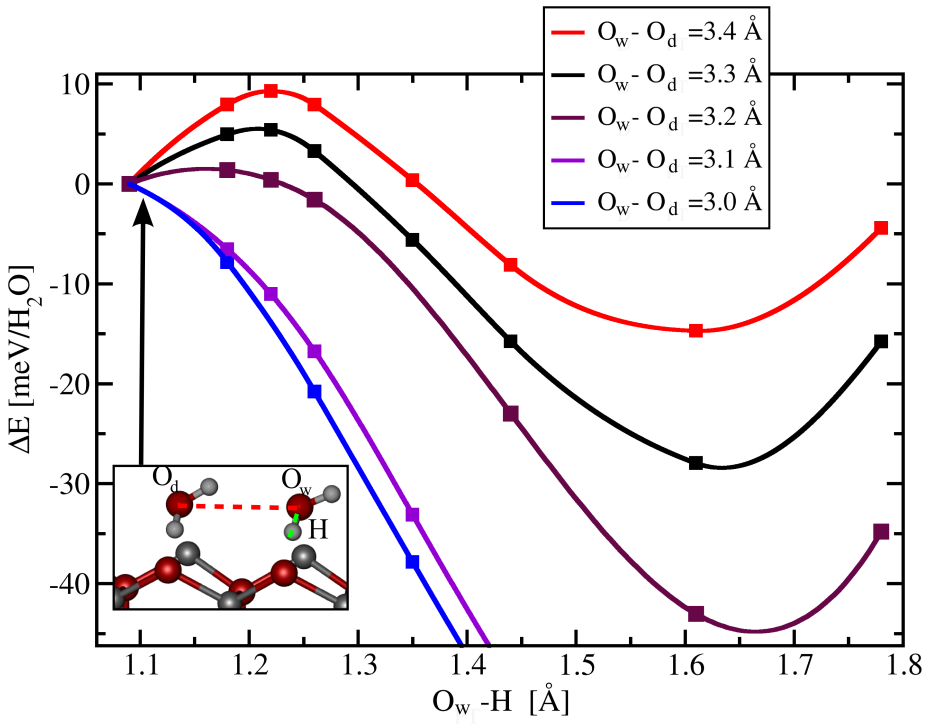

Figure A.1: Energy pathways along the O_w-H bond-length for the transition from molecular water adsorption to partially dissociated adsorption. ΔE is the total energy difference from the initial (molecular) state resulting from single-point calculations. Each line refers to a different constraint for the O_w-O_d distance. At an O_w-O_d distance below 3.2 Å the dissociation barrier is zero, whereas it increases as O_w-$O_d \gtrsim 3.2$Å. The snapshot indicates the structure of the initial (molecular) state with the labels on the corresponding atoms.

Bibliography

[1] P. Ball. *H_2O A biography of water*. Phoenix, Orion Books Ltd, 1999.

[2] P. Ball. Water–an enduring mystery. *Nature*, 452:291, 2008.

[3] A. Fujishima and K. Honda. Electrochemical Photolysis of Water at a Semiconductor Electrode. *Nature*, 238:37, 1972.

[4] Akira Fujishima, Xintong Zhang, and Donald A. Tryk. Tio_2 photocatalysis and related surface phenomena. *Surf. Sci. Rep.*, 63(12):515–582, 2008.

[5] R. M. Feynman. There's plenty of room at the bottom. *Engineering and Science*, 23:22–36, 1959.

[6] G. Binnig, H. Rohrer, Ch. Gerber, and E. Weibel. Tunneling through a controllable vacuum gap. *Appl. Phys. Lett.*, 40(2):178–180, 1982.

[7] G. Binnig, H. Rohrer, Ch. Gerber, and E. Weibel. Surface studies by scanning tunneling microscopy. *Phys. Rev. Lett.*, 49:57–61, 1982.

[8] Donald M Eigler and Erhard K Schweizer. Positioning single atoms

with a scanning tunnelling microscope. *Nature*, 344(6266):524–526, 1990.

[9] IBM Research, "A Boy And His Atom: The World's Smallest Movie.". http://www.research.ibm.com/articles/madewithatoms.shtml.

[10] J. Carrasco, A. Hodgson, and A. Michaelides. A Molecular Perspective of Water at Metal Interfaces. *Nature Mater.*, 11:667–674, 2012.

[11] Henderson, Michael A. The interaction of water with solid surfaces: fundamental aspects revisited. *Surf. Sci. Rep.*, 46:1–308, 2002.

[12] M. Salmeron and R. Schlögl. Ambient pressure photoelectron spectroscopy: A new tool for surface science and nanotechnology. *Surf. Sci. Rep.*, 63(4):169–199, 2008.

[13] D. Marx. Proton Transfer 200 Years after von Grotthuss: Insights from Ab Initio Simulations. *ChemPhysChem*, 7:1848–1870, 2006.

[14] O. F. Mohammed, D. Pines, J. Dreyer, E. Pines, and E. T. J. Nibbering. Sequential proton transfer through water bridges in acid-base reactions. *Science*, 310(5745):83–86, 2005.

[15] P. L. Geissler, C. Dellago, D. Chandler, J. Hutter, and M. Parrinello. Autoionization in liquid water. *Science*, 291(5511):2121–2124, 2001.

[16] C Cavazzoni, G. L. Chiarotti, S Scandolo, E Tosatti, M Bernasconi, and M Parrinello. Superionic and metallic states of water and ammonia at giant planet conditions. *Science*, 283(5398):44–46, 1999.

[17] Li-Chiang Lin, Adam H Berger, Richard L Martin, Jihan Kim, Joseph A Swisher, Kuldeep Jariwala, Chris H Rycroft, Abhoyjit S Bhown, Michael W Deem, Maciej Haranczyk, et al. In silico screening of carbon-capture materials. *Nat. Mater.*, 11(7):633–641, 2012.

[18] Jens Kehlet Nørskov, Thomas Bligaard, Jan Rossmeisl, and Claus Hviid Christensen. Towards the computational design of solid catalysts. *Nat. Chem.*, 1(1):37–46, 2009.

[19] Axel D. Becke. Perspective: Fifty years of density-functional theory in chemical physics. *J. Chem. Phys.*, 140:18A301, 2014.

[20] M. Behrens, F. Studt, I. Kasatkin, S Kühl, Michael Hävecker, F. Abild-Pedersen, S. Zander, F. Girgsdies, P. Kurr, B.-L. Kniep, Michael Tovar, R. W. Fischer, J. K. Nørskov, and Robert Schlögl. The Active Site of Methanol Synthesis over $Cu/ZnO/Al_2O_3$ Industrial Catalysts. *Science*, 336:893–897, 2012.

[21] A. Siria, Philippe Poncharal, Anne-Laure Biance, Rémy Fulcrand, Xavier Blase, S. T. Purcell, and L. Bocquet. Giant osmotic energy conversion in a single transmembrane boron nitride nanotube. *Nature*, 494:455, 2013.

[22] D. Cohen-Tanugi and Jeffrey C. Grossman. Water desalination across nanoporous graphene. *Nano Lett.*, 12(7):3602–3608, 2012.

[23] Patrice Simon and Yury Gogotsi. Materials for electrochemical capacitors. *Nat. Mater.*, 7(11):845–854, 2008.

[24] D. Konatham, J. Yu, T. A. Ho, and A. Striolo. Simulation insights for graphene-based water desalination membranes. *Langmuir*, 29(38):11884–11897, 2013.

[25] B. E. Logan and M. Elimelech. Membrane-based processes for sustainable power generation using water. *Nature*, 488:313–319, 2012.

[26] Hadeel Hussain, G. Tocci, T. Woolcot, X. Torrelles, C. L. Pang, D. S. Humphrey, C. M. Yim, D. C. Grinter, G. Cabailh, O. Bikondoa, R. Lindsay, A. Michaelides, and G. Thornton. Structure of the TiO_2 photocatalytic interface, *In preparation*.

[27] N. W. Ashcroft and N. D. Mermin. *Solid State Physics*. Saunders, 1976.

[28] R. M. Martin. *Electronic Structure. Basic Theory and Practical Methods*, volume 1. Cambridge University Press, 2005.

[29] Stefano Baroni, Stefano de Gironcoli, Andrea Dal Corso, and Paolo Giannozzi. Phonons and related crystal properties from density-functional perturbation theory. *Rev. Mod. Phys.*, 73:515–562, 2001.

[30] Even for the homogeneous electron gas an analytical solution exists only for the kinetic and exchange energy. Although an approximation of the correlation energy is provided by Thomas-Fermi theory, a more accurate numerical estimation has been obtained from quantum monte carlo calculations [35].

[31] Frank Jensen. *Introduction to Computational Chemistry*. Wiley, 2006.

[32] P. Hohenberg and W. Kohn. Inhomogeneous Electron Gas. *Phys. Rev.*, 136:B864, 1964.

[33] W. Kohn and L. J. Sham. Self-consistent equations including exchange and correlation effects. *Phys. Rev.*, 140:A1133–A1138, 1965.

[34] E. A Carter. Challenges in modeling materials properties without experimental input. *Science*, 321(5890):800–803, 2008.

[35] D. M. Ceperley and B. J. Alder. Ground state of the electron gas by a stochastic method. *Phys. Rev. Lett.*, 45:566–569, 1980.

[36] A. Michaelides and M. Scheffler. *Surface and Interface Science*, volume 1. Wiley-WCH, 2012.

[37] J. P. Perdew, J. A. Chevary, S. H. Vosko, K. A. Jackson, M. R. Pederson, D. J. Singh, and C. Fiolhais. Atoms, molecules, solids, and surfaces: Applications of the generalized gradient approximation for exchange and correlation. *Phys. Rev. B*, 46:6671–6687, 1992.

[38] J. P. Perdew, K. Burke, and M. Ernzerhof. Generalized gradient approximation made simple. *Phys. Rev. Lett.*, 77:3865, 1996.

[39] A. D. Becke. Density-functional exchange-energy approximation with correct asymptotic-behavior. *Phys. Rev. A*, 38:3098, 1988.

[40] C. Lee, W. Yang, and G. Parr. Development of the Colle-Salvetti correlation-energy formula into a functional of the electron density. *Phys. Rev. B*, 37:785–789, 1988.

[41] John P. Perdew, J. A. Chevary, S. H. Vosko, Koblar A. Jackson, Mark R. Pederson, D. J. Singh, and Carlos Fiolhais. Atoms, molecules, solids, and surfaces: Applications of the generalized gradient approximation for exchange and correlation. *Phys. Rev. B*, 46:6671–6687, 1992.

[42] V. N. Staroverov, G. E. Scuseria, and J. Tao. Tests of a ladder of density functionals for bulk solids and surfaces. *Phys. Rev. B*, 69:075102, 2004.

[43] D. Alfè and M. J. Gillan. The energetics of oxide surfaces by quantum monte carlo. *J. Phys.: Condens. Matter*, 18:L435, 2006.

[44] J. Klimeš and A. Michaelides. Perspective: Advances and Challenges in Treating van der Waals Dispersion Forces in Density Functional Theory. *J. Chem. Phys.*, 137:120901, 2012.

[45] S. Grimme. Accurate description of van der Waals complexes by density functional theory including empirical corrections. *J. Comp. Chem.*, 25:1463, 2004.

[46] S. Grimme. Semiempirical gga-type density functional constructed with a long-range dispersion correction. *J. Comp. Chem.*, 27:1787, 2006.

[47] Grimme, S. and Antony, J. and Ehrlich, S. and Krieg, H. A consistent and accurate ab initio parametrization of density functional dispersion correction (DFT-D) for the 94 elements H-Pu. *J. Chem. Phys.*, 132(15):154104, 2010.

[48] A. D. Becke and E. R. Johnson. A density-functional model of the dispersion interaction. *J. Chem. Phys.*, 123(15):154101, 2005.

[49] A. Tkatchenko and M. Scheffler. Accurate Molecular Van Der Waals Interactions from Ground-State Electron Density and Free-Atom Reference Data. *Phys. Rev. Lett.*, 102:073005, 2009.

[50] J. Klimeš, D. R. Bowler, and A. Michaelides. Chemical accuracy for the van der Waals density functional. *J. Phys.: Condens. Matter*, 22:022201, 2010.

[51] J. Klimeš, D. R. Bowler, and A. Michaelides. Van der Waals density functionals applied to solids. *Phys. Rev. B*, 83:195131, 2011.

[52] K. Lee, É. D. Murray, L. Kong, B. I. Lundqvist, and D. C. Langreth. Higher-accuracy van der waals density functional. *Phys. Rev. B*, 82:081101, 2010.

[53] P. L. Silvestrelli. Van der waals interactions in dft made easy by wannier functions. *Phys. Rev. Lett.*, 100:053002, 2008.

[54] O. Gunnarsson and B. I. Lundqvist. Exchange and correlation in atoms, molecules, and solids by the spin-density-functional formalism. *Phys. Rev. B*, 13:4274–4298, 1976.

[55] D. C. Langreth and J. P. Perdew. Exchange-correlation energy of a metallic surface: Wave-vector analysis. *Phys. Rev. B*, 15:2884–2901, 1977.

[56] J. F. Dobson and B. P. Dinte. Constraint satisfaction in local and gradient susceptibility approximations: Application to a van der waals density functional. *Phys. Rev. Lett.*, 76:1780–1783, 1996.

[57] F. Furche. Molecular tests of the random phase approximation to the exchange-correlation energy functional. *Phys. Rev. B*, 64:195120, 2001.

[58] Judith Harl and Georg Kresse. Accurate bulk properties from approximate many-body techniques. *Phys. Rev. Lett.*, 103:056401, 2009.

[59] Deyu Lu, Yan Li, Dario Rocca, and Giulia Galli. *Ab initio* calculation of van der waals bonded molecular crystals. *Phys. Rev. Lett.*, 102:206411, 2009.

[60] J. P. Perdew and A. Zunger. Self-interaction correction to density-functional approximations for many-electron systems. *Phys. Rev. B*, 23:5048, 1981.

[61] V. I. Anisimov, J. Zaanen, and O. K. Andersen. Band theory and Mott insulators: Hubbard U instead of Stoner I. *Phys. Rev. B*, 44(3):943–954, 1991.

[62] A. J. Cohen, P. Mori-Sánchez, and W. Yang. Insights into current limitations of density functional theory. *Science*, 321(5890):792–794, 2008.

[63] A. D. Becke. A new mixing of Hartree-Fock and local density-functional theories. *J. Chem. Phys.*, 98:5648, 1993.

[64] C. Lee, W. Yang, and R. G. Parr. Development of the Colle-Salvetti correlation-energy formula into a functional of the electron density. *Phys. Rev. B*, 37:785, 1988.

[65] J. P. Perdew, K. Burke, and M. Ernzerhof. Rationale for mixing exact exchange with density functional approximations. *J. Chem. Phys.*, 105:9982, 1996.

[66] J. Heyd, G. E. Scuseria, and M. Ernzerhof. Hybrid functionals based on a screened Coulomb potential. *J. Chem. Phys.*, 124:219906, 2006.

[67] G. Onida, L. Reining, and A. Rubio. Electronic excitations: density-functional versus many-body Green's-function approaches. *Rev. Mod. Phys.*, 74:601–659, 2002.

[68] G. Lippert, J. Hutter, and M. Parrinello. A hybrid Gaussian and plane wave density functional scheme. *Mol. Phys.*, 92:477, 1997.

[69] J. VandeVondele, M. Krack, F. Mohamed, M. Parrinello, T. Chassaing, and J. Hutter. QUICKSTEP: Fast and accurate density functional calculations using a mixed Gaussian and plane waves approach. *Comp. Phys. Comm.*, 167:103, 2005.

[70] D. Vanderbilt. Soft self-consistent pseudopotentials in a generalized eigenvalue formalism. *Phys. Rev. B*, 41:7892, 1990.

[71] E. Blöchl. Projector augmented-wave method. *Phys. Rev. B*, 50:17953, 1994.

[72] R. Car and M. Parrinello. Unified approach for molecular dynamics and density-functional theory. *Phys. Rev. Lett.*, 55:2471–2474, 1985.

[73] M. Sprik, J. Hutter, and M. Parrinello. *Ab initio* molecular dynamics simulation of liquid water: Comparison of three gradient-corrected density functionals. *J. Chem. Phys.*, 105(3):1142–1152, 1996.

[74] Pier Luigi Silvestrelli, M. Bernasconi, and Michele Parrinello. Ab initio infrared spectrum of liquid water. *Chem. Phys. Lett.*, 277(5-6):478 – 482, 1997.

[75] C. Molteni and M. Parrinello. Glucose in aqueous solution by first principles molecular dynamics. *J. Am. Chem. Soc.*, 120(9):2168–2171, 1998.

[76] Matthew P. Grumbach and Richard M. Martin. Phase diagram of carbon at high pressures and temperatures. *Phys. Rev. B*, 54:15730–15741, 1996.

[77] J. VandeVondele and J. Hutter. An efficient orbital transformation method for electronic structure calculations. *J. Chem. Phys.*, 118(10):4365–4369, 2003.

[78] J. Kolafa. Time-reversible always stable predictor–corrector method for molecular dynamics of polarizable molecules. *J. Comp. Chem.*, 25(3):335–342, 2004.

[79] M. E. Tuckerman. *Statistical Mechanics: Theory and Molecular Simulation*, volume 1. Oxford University Press, 2010.

[80] G. Martyna, M. L. Klein, and M. E. Tuckerman. Nosé-Hoover chains: The canonical ensemble via continuous dynamics. *J. Chem. Phys.*, 97:2635, 1992.

[81] S. Nosé. A unified formulation of the constant temperature molecular dynamics methods. *J. Chem. Phys.*, 81(1):511–519, 1984.

[82] William G. Hoover. Canonical dynamics: Equilibrium phase-space distributions. *Phys. Rev. A*, 31:1695–1697, 1985.

[83] K. Falk, F. Sedlmeier, L. Joly, R. R. Netz, and L. Bocquet. Molecular origin of fast water transport in carbon nanotube membranes: Superlubricity versus curvature dependent friction. *Nano Lett.*, 10:4067–4073, 2010.

[84] M. Law, L. E. Greene, J. C. Johnson, R. Sayakally, and P. Yang. Nanowire dye-sensitized solar cells. *Nature Mater.*, 4:455–459, 2005.

[85] Jinhui Song Xudong Wang, Jin Liu, and Zhong Lin Wang. Direct-current nanogenerator driven by ultrasonic waves. *Science*, 316:102, 2007.

[86] Zhong Lin Wang and Jinhui Song. Piezoelectric nanogenerators based on zinc oxide nanowire arrays. *Science*, 312:242, 2006.

[87] C. Wöll. The chemistry and physics of zinc oxide surfaces. *Prog. Surf. Sci.*, 82:55, 2007.

[88] B. Meyer and D. Marx. Density-functional study of the structure and stability of ZnO surfaces. *Phys. Rev. B*, 63:035403, 2003.

[89] A. R. Lubinsky, C. B. Duke, S. C. Chang, B. W. Lee, and P. Mark. Atomic geometry of the low-index surfaces of zinc oxide: LEED analysis. *J. Vac. Sci. Technol.*, 13:189, 1976.

[90] C. B. Duke, R. J. Meyer, A. Paton, and P. Mark. Calculation of low-energy-electron-diffraction intensities from ZnO($10\bar{1}0$). ii. influence of calculational procedure, model potential, and second-layer structural distortions. *Phys. Rev. B*, 18:4225–4240, 1978.

[91] C B Duke and Y.R. Wang. Surface structure and bonding of the cleavage faces of tetrahedrally coordinated II-VI compounds. *J. Vac. Sci. Technol. B*, 6:1440, 1988.

[92] W. Göpel, J. Pollmann, I. Ivanov, and B. Reihl. Angle-resolved photoemission from polar and nonpolar zinc oxide surfaces. *Phys. Rev. B*, 26:3144–3150, 1982.

[93] N. Jedrecy, S. Gallini, M. Sauvage-Simkin, and R. Pinchaux. Copper growth on the O-terminated ZnO($000\bar{1}$) surface: Structure and morphology. *Phys. Rev. B*, 64:085424, 2001.

[94] T. M. Parker, N. G. Condon, R. Lindsay, F. M. Leibsle, and G. Thornton. Imaging the polar (0001) and non-polar (1010) surfaces of ZnO with STM. *Surf. Sci.*, 415(3):L1046–L1050, 1998.

[95] J. E. Jaffe and A. C. Hess. Ab Initio Study of ZnO($10\bar{1}0$) Surface Relaxation. *Phys. Rev. B*, 49:11153, 1994.

[96] Schröer, Peter and Krüger, Peter and Pollmann, Johannes. Self-consistent electronic-structure calculations of the $(10\bar{1}0)$ surfaces of the wurtzite compounds ZnO and CdS. *Phys. Rev. B*, 49:17092–17101, 1994.

[97] A. Wander and N. M. Harrison. *Ab Initio* Study of ZnO$(10\bar{1}0)$. *Surf. Sci.*, 457:L342, 2000.

[98] Jan Wróbel, Krzysztof J. Kurzydłowski, Kerstin Hummer, Georg Kresse, and Jacek Piechota. Calculations of ZnO properties using the Heyd-Scuseria-Ernzerhof screened hybrid density functional. *Phys. Rev. B*, 80:155124, 2009.

[99] Alessio Filippetti, Vincenzo Fiorentini, Giancarlo Cappellini, and Andrea Bosin. Anomalous relaxations and chemical trends at III-V semiconductor nitride nonpolar surfaces. *Phys. Rev. B*, 59:8026–8031, 1999.

[100] Bernd Meyer, Dominik Marx, Olga Dulub, Ulrike Diebold, Martin Kunat, Deler Langenberg, and Christof Wöll. Partial Dissociation of Water Leads to Stable Superstructures on the Surface of Zinc Oxide. *Angew. Chem., Int. Ed.*, 48:6641–6645, 2004.

[101] O. Dulub, B. Meyer, and U. Diebold. Observation of the Dynamical Change in a Water Monolayer Adsorbed on a ZnO Surface. *Phys. Rev. Lett.*, 95:136101, 2005.

[102] B. Meyer, H. Rabaa, and D. Marx. Water Adsorption on ZnO$(10\bar{1}0)$: from Single Molecules to Partially Dissociated Monolayers. *Phys. Chem. Chem. Phys.*, 8:1513–1520, 2006.

[103] Karen Johnston, Jesper Kleis, Bengt I. Lundqvist, and Risto M. Nieminen. Influence of van der Waals forces on the adsorption structure of benzene on silicon studied using density functional theory. *Phys. Rev. B*, 77:121404, 2008.

[104] G. Kresse and J. Hafner. *Ab initio* Molecular Dynamics for Liquid Metals. *Phys. Rev. B*, 47:558–561, 1993.

[105] G. Kresse and J. Furthmüller. Efficient Iterative Schemes for *Ab Initio* Total-Energy Calculations Using a Plane-Wave Basis Set. *Phys. Rev. B*, 54:11169–11186, 1996.

[106] G. Kresse and J. Furthmüller. *Ab initio* molecular-dynamics simulation of the liquid-metal-amorphous-semiconductor transition in germanium. *Phys. Rev. B*, 49:14251, 1994.

[107] G. Kresse and D. Joubert. From ultrasoft pseudopotentials to the projector augmented-wave method. *Phys. Rev. B*, 59:1758, 1999.

[108] S. Goedecker, M. Teter, and J. Hutter. Separable dual-space gaussian pseudopotentials. *Phys. Rev. B*, 54:1703–1710, 1996.

[109] J. VandeVondele and J. Hutter. Gaussian basis sets for accurate calculations on molecular systems in gas and condensed phases. *J. Chem. Phys.*, 127:114105, 2007.

[110] H. J. Monkhorst and J. D. Pack. Special points for Brillouin-zone integrations. *Phys. Rev. B*, 13:5188, 1976.

[111] G. J. Martyna and M. E. Tuckerman. A reciprocal space based method for treating long range interactions in ab initio and force-field-based calculations in clusters. *J. Chem. Phys.*, 110:2810–2821, 1999.

[112] *CRC Handbook of Chemistry and Physics*, volume 88. CRC press, Boca Raton, 2007.

[113] A. Janotti, D. Segev, and C. G. Van de Walle. Effects of cation d states on the structural and electronic properties of III-nitride and II-oxide wide-band-gap semiconductors. *Phys. Rev. B*, 74(3):045202, 2006.

[114] J. Carrasco, B. Santra, J. Klimeš, and A. Michaelides. To Wet or not to Wet? Dispersion Forces Tip the Balance for Water-Ice on Metals. *Phys. Rev. Lett.*, 106:026101, 2011.

[115] J. Pollmann and P. Krüger and M. Rohlfing and M. Sabisch and D. Vogel. *Ab initio* calculations of structural and electronic properties of prototype surfaces of group IV, III-V and II-VI semiconductors. *Appl. Surf. Sci.*, 104-105:1–16, 1996.

[116] J. L. Da Silva, C. Stampfl, and M. Scheffler. Converged properties of clean metal surfaces by all electron first principles calculations. *Surf. Sci.*, 600:703, 2006.

[117] Yan Zhao and Donald G. Truhlar. Design of density functionals that are broadly accurate for thermochemistry, thermochemical kinetics, and nonbonded interactions. *The Journal of Physical Chemistry A*, 109(25):5656–5667, 2005.

[118] Roald Hoffmann. A chemical and theoretical way to look at bonding on surfaces. *Rev. Mod. Phys.*, 60:601–628, 1988.

[119] B. C. H. Steele and A. Heinzel. Materials for fuel-cell technologies. *Nature*, 414:345, 2001.

[120] F. Garczarek and K. Gerwert. Functional waters in intraprotein proton transfer monitored by FTIR difference spectroscopy. *Nature*, 439:109–112, 2006.

[121] R. D. Cortright, R. R. Davda, and J. A. Dumesic. Hydrogen from catalytic reforming of biomass-derived hydrocarbons in liquid water. *Nature*, 418:964–967, 2002.

[122] A. Michaelides and P. Hu. Catalytic Water Formation on Platinum: A First Principles Study. *J. Am. Chem. Soc.*, 123:4235–4242, 2001.

[123] M. E. Tuckerman, D. Marx, M. L. Klein, and M. Parrinello. On the Quantum Nature of the Shared Proton in Hydrogen Bonds. *Science*, 275:817–820, 1997.

[124] D. Marx, M. E. Tuckerman, J. Hutter, and M. Parrinello. The nature of the hydrated excess proton in water. *Nature*, 397:601, 1999.

[125] T. C. Berkelbach, H.-S. Lee, and M. E. Tuckerman. Concerted hydrogen-bond dynamics in the transport mechanism of the hydrated proton: A first-principles molecular dynamics study. *Phys. Rev. Lett.*, 103:238302, 2009.

[126] Klas Andersson, Guido Ketteler, Hendrik Bluhm, Susumu Yamamoto, Hirohito Ogasawara, Lars G. M. Pettersson, Miquel Salmeron, and Anders Nilsson. Autocatalytic Water Dissociation on Cu(110) at Near Ambient Conditions. *J. Am. Chem. Soc.*, 130:2793–2797, 2008.

[127] Yuki Nagata, Ruben E. Pool, Ellen H. G. Backus, and Mischa Bonn. Nuclear quantum effects affect bond orientation of water at the water-vapor interface. *Phys. Rev. Lett.*, 109:226101, 2012.

[128] M. Sulpizi, M. P. Gaigeot, and M. Sprik. The Silica-Water Interface: How the Silanols Determine the Surface Acidity and Modulate the Water Properties. *J. Chem. Theory Comput.*, 8:1037–1047, 2012.

[129] J. Cheng and M. Sprik. Acidity of the Aqueous Rutile TiO_2(110) Surface from Density Functional Theory Based Molecular Dynamics. *J. Chem. Theory Comput.*, 6:880–889, 2010.

[130] J. Wang, L. S. Pedroza, A. Poissier, and M. V. Fernandez-Serra. Photocatalytic Water Oxidation at the GaN($10\bar{1}0$) Water Interface. *J. Phys. Chem. C*, 116:14382–14389, 2012.

[131] K. C. Hass, W. F. Schneider, Curioni A, and W. Andreoni. The Chemistry of Water on Alumina Surfaces: Reaction Dynamics from First Principles. *Science*, 282:265–268, 1998.

[132] B. C. Wood, E. Scwegler, W. I. Choi, and T. Ogitsu. Hydrogen-Bond Dynamics of Water at the Interface with InP/GaP (001) and the Implications for Photoelectrochemistry. *J. Am. Chem. Soc.*, 135:15774–15783, 2013.

[133] L. Martínez-Suárez, J. Frenzel, D. Marx, and B. Meyer. Tuning the Reactivity of a Cu/ZnO Nanocatalyst via Gas Phase Pressure. *Phys. Rev. Lett.*, 110:086108, 2013.

[134] Y. Wang, M. Muhler, and Ch. Wöll. Spectroscopic Evidence for the Partial Dissociation of H_2O on ZnO($10\bar{1}0$). *Phys. Chem. Chem. Phys.*, 8:1521, 2006.

[135] D. Raymand, A. C. T. van Duin, W. A. Goddard, K. Hermansson, and D. Spangberg. Hydroxylation Structure and Proton Transfer Reactivity at the Zinc Oxide-Water Interface. *J. Phys. Chem. C*, 115:8573–8579, 2011.

[136] S. G. Holthaus, S. Köppen, T. Frauenheim, and L. Colombi Ciacchi. Atomistic simulations of the zno($1\bar{2}10$)/water interface: A comparison between first-principles, tight-binding, and empirical methods. *J. Chem. Theory Comput.*, 8:4517–4526, 2013.

[137] M. Valtiner, M. Todorova, G. Grundmeier, and J. Neugebauer. Temperature Stabilized Surface Reconstructions at Polar ZnO(0001). *Phys. Rev. Lett.*, 103:065502, 2009.

[138] G. Cicero, A. Catellani, and G. Galli. Atomic Control of Water Interaction with Biocompatible Surfaces: The Case of SiC(001). *Phys. Rev. Lett.*, 93:016102, 2004.

[139] Li-Min Liu, A. Laio, and A. Michaelides. Initial Stages of Salt Dissolution Determined with Ab Initio Molecular Dynamics. *Phys. Chem. Chem. Phys.*, 13:13162, 2011.

[140] T. Song and P. Hu. Insight into the Solvent Effect: A Density Functional Theory Study of Cisplatin Hydrolysis. *J. Chem. Phys.*, 125:091101, 2006.

[141] J. Haw, Teng Xu, J. B. Nicholas, and Patrick W. Goguen. Solvent-Assisted Proton Transfer in Catalysis by Zeolite Solid Acids. *Nature*, 389:832–835, 1997.

[142] M. J. Janik, R. J. Davis, and M. Neurock. Anhydrous and Water-Assisted Proton mobility in phosphotungstic acid. *J. Am. Chem. Soc.*, 127:5328–5245, 2005.

[143] G. V. Lewis and C. R. A. Catlow. Potential models for ionic oxides. *J. Phys. C.: Solid State Phys*, 18:1149–1161, 1985.

[144] Y. Wu, H. L. Tepper, and G. A. Voth. Flexible simple point-charge water model with improved liquid-state properties. *J. Chem. Phys.*, 124:024503, 2006.

[145] I-C. Lin, A. P. Seitsonen, I. Tavernelli, and U. Rothlisberger. Importance of van der Waals Interactions in Liquid Water. *J. Chem. Theory Comput.*, 8:3, 2012.

[146] G. Bussi, D. Donadio, and M. Parrinello. Canonical Sampling Through Velocity Rescaling. *J. Chem. Phys.*, 126:014101, 2007.

[147] B. Santra, J. Klimeš, D. Alfè, B. Slater, A. Michaelides, R. Car, and M. Scheffler. Hydrogen Bonds and van der Waals Forces in Ice at Ambient and High Pressures. *Phys. Rev. Lett.*, 107:185701, 2011.

[148] C. Zhang, J. Wu, G. Galli, and F. Gygi. Structural and Vibrational Properties of Liquid Water from van der Waals Density Functionals. *J. Chem. Theory Comput.*, 7:3054, 2011.

[149] L. Liu, M. Krack, and A. Michaelides. Density Oscillations in a Nanoscale Water Film on Salt: Insight from Ab Initio Molecular Dynamics. *J. Am. Chem. Soc.*, 130:8572, 2008.

[150] G. Cicero, Jeffrey C. Grossman, E. Schwegler, F. Gygi, and G. Galli. Water confined in nanotubes and between graphene sheets: A first principle study. *J. Am. Chem. Soc.*, 130:1871–1878, 2008.

[151] P. Fenter and N. C. Sturchio. Mineral-water interfacial structures revealed by synchrotron x-ray scattering. *Prog. Surf. Sci.*, 77:171, 2004.

[152] T. Fukuma, Y. Ueda, S. Yoshioka, and H. Asakawa. Atomic-scale distribution of water molecules at the mica-water interface visualized by three-dimensional scanning force microscopy. *Phys. Rev. Lett.*, 104:016101, 2010.

[153] D. Argyris, T. Ho, D. R. Cole, and A. Striolo. Molecular dynamics studies of interfacial water at the alumina surface. *J. Phys. Chem. C*, 115(5):2038–2046, 2011.

[154] B. G. Walker, N. Marzari, and C. Molteni. Ab initio studies of layering behavior of liquid sodium surfaces and interfaces. *J. Chem. Phys.*, 124(17):174702, 2006.

[155] I. F. W. Kuo and C. J. Mundy. An ab Initio Molecular Dynamics Study of the Aqueous Liquid-Vapor Interface. *Science*, 303:658, 2004.

[156] From a separate set of geometry optimizations we established that the contact layer of the LF (without the liquid overlayer above it) is 90 $\pm$ 30 meV/H_2O less stable than the structure of the ML. This value was obtained by comparing the energy of the optimized ML with the average energy of 5 characteristic snapshots of the contact layer from the LF simulation (each relaxed in the absence of the liquid overlayer).

[157] S. Woutersen and H. J. Bakker. Ultrafast vibrational and structural dynamics of the proton in liquid water. *Phys. Rev. Lett.*, 96:138305, 2006.

[158] A. V. Akimov, J. T. Muckerman, and O. V. Prezhdo. Nonadiabatic Dynamics of Positive Charge during Photocatalytic Water Splitting on GaN(10$\bar{1}$0) Surface: Charge Localization Governs Splitting Efficiency. *J. Am. Chem. Soc.*, 135:8682–8691, 2013.

[159] Brandon C. Wood, Eric Schwegler, Woon Ih Choi, and Tadashi Ogitsu. Surface Chemistry of GaP(001) and InP(001) in Contact with Water. *J. Phys. Chem. C*, 118(2):1062–1070, 2014.

[160] David Raymand, Adri C.T. van Duin, Daniel Spångberg, William A. Goddard III, and Kersti Hermansson. Water adsorption on stepped ZnO surfaces from MD simulation. *Surf. Sci.*, 604(9-10):741 – 752, 2010.

[161] Li-Min Liu, Changjun Zhang, Geoff Thornton, and Angelos Michaelides. Structure and Dynamics of Liquid Water on Rutile TiO_2(110). *Phys. Rev. B*, 82:161415(R), 2010.

[162] Li-Min Liu, Changjun Zhang, Geoff Thornton, and Angelos Michaelides. Reply to "Comment on 'Structure and Dynamics of Liquid Water on Rutile TiO_2(110)' ". *Phys. Rev. B*, 85:167402, 2012.

[163] A. Michaelides, A. Alavi, and D. A. King. Different Surface Chemistries of Water on Ru{0001} From Monomer Adsorption to Partially Dissociated Bilayers. *J. Am. Chem. Soc.*, 125:2746–2755, 2003.

[164] M. Odelius. Mixed Molecular and Dissociative Water Adsorption on MgO[100]. *Phys. Rev. Lett.*, 82:3919–3922, 1999.

[165] X. L. Hu, J. Klimeš, and A. Michaelides. Proton transfer in adsorbed water dimers. *Phys. Chem. Chem. Phys.*, 12:3953, 2010.

[166] X. Z. Li, Matthew I. J. Probert, Ali Alavi, and Angelos Michaelides. Quantum nature of the proton in water-hydroxyl overlayers on metal surfaces. *Phys. Rev. Lett.*, 104:066102, 2010.

[167] Lindsay R. Merte, Guowen Peng, Ralf Bechstein, Felix Rieboldt, Carrie A. Farberow, Lars C. Grabow, Wilhelmine Kudernatsch, Stefan Wendt, Erik Lægsgaard, Manos Mavrikakis, and Flemming Besenbacher. Water-Mediated Proton Hopping on an Iron Oxide Surface. *Science*, 336:889–893, 2012.

[168] Jason K. Holt, Hyung Gyu Park, Yinmin Wang, Michael Stadermann,

Alexander B. Artyukhin, Costas P. Grigoropoulos, Aleksandr Noy, and Olgica Bakajin. Fast mass transport through sub-2-nanometer carbon nanotubes. *Science*, 312(5776):1034–1037, 2006.

[169] M. Majumder, N. Chopra, R. Andrews, and B. J. Hinds. Nanoscale hydrodynamics - enhanced flow in carbon nanotubes. *Nature*, 438(7064):44–44, 2005.

[170] G. Hummer, J. C. Rasaiah, and J. P. Noworyta. Water conduction through the hydrophobic channel of a carbon nanotube. *Nature*, 414:188–190, 2001.

[171] R. R. Nair, H. A. Wu, P. N. Jayaram, I. V. Grigorieva, and A. K. Geim. Unimpeded permeation of water through helium-leak-tight graphene-based membranes. *Science*, 335(6067):442–444, 2012.

[172] L. Bocquet and E. Charlaix. Nanofluidics, from bulk to interfaces. *Chem. Soc. Rev.*, 39(3):1073–1095, 2010.

[173] A. Striolo. The mechanism of water diffusion in narrow carbon nanotubes. *Nano Lett.*, 6(4):633–639, 2006.

[174] L. Bocquet and J. L. Barrat. Flow boundary conditions from nano- to micro-scales. *Soft Matter*, 3(6):685–693, 2007.

[175] C. Y. Won and N. R. Aluru. Water Permeation through a Subnanometer Boron Nitride Nanotube. *J. Am. Chem. Soc.*, 129:2748, 2007.

[176] C. Y. Won and N. R. Aluru. Structure and Dynamics of Water Confined in a Boron Nitride Nanotube. *J. Phys. Chem. C*, 112:1182–1818, 2008.

[177] A Niguès, A. Siria, P. Vincent, Poncharal P., and L. Bocquet. Ultrahigh interlayer friction in multiwalled boron nitride nanotubes. *Nat. Mater.*, 13:688–693, 2014.

[178] R. Zhang, Z. Ning, Y. Zhang, Q. Zheng, Q. Chen, H. Xie, Q. Zhang, W. Qian, and F. Wei. Superlubricity in centimetres-long double-walled carbon nanotubes under ambient conditions. *Nat. Nanotech.*, 8:912–916, 2013.

[179] Hui Li and Xiao Cheng Zeng. Wetting and interfacial properties of water nanodroplets in contact with graphene and monolayer boron-nitride sheets. *ACS Nano*, 6:2401–2409, 2012.

[180] A. Vanossi, N. Manini, M. Urbakh, S. Zapperi, and E. Tosatti. Colloquium: Modeling friction: From nanoscale to mesoscale. *Rev. Mod. Phys.*, 85:529, 2013.

[181] Chih-Jen Shih, Qing Hua Wang, Shangchao Lin, Kyoo-Chul Park, Zhong Jin, Michael S. Strano, and Daniel Blankschtein. Breakdown in the wetting transparency of graphene. *Phys. Rev. Lett.*, 109:176101, 2012.

[182] X. Mi Javad Rafiee, H. Gullapalli, A. V. Thomas, F. Yavari, Y. Shi, Ajayan P. M., and N. A. Koratkar. Wetting transparency of graphene. *Nat. Mater.*, 11:217–222, 2012.

[183] G. Tocci and A. Michaelides. Solvent-induced proton hopping at a water-oxide interface. *J. Phys. Chem. Lett.*, 5(3):474–480, 2014.

[184] Kühne, M. Krack, and M. Parrinello. Static and Dynamical Properties of Liquid Water from First Principles by a Novel Car-Parrinello-like Approach. *J. Chem. Theory Comput.*, 23:5161, 1998.

[185] D. Alfè and M. J. Gillan. First-Principles Calculation of Transport Coefficients. *Phys. Rev. Lett.*, 23:5161, 1998.

[186] Peter J. Feibelman. Viscosity of ultrathin water films confined between aluminol surfaces of kaolinite: Ab initio simulations. *J. Phys. Chem. C*, 117(12):6088–6095, 2013.

[187] Kerstin Falk, Felix Sedlmeier, Laurent Joly, Roland R. Netz, and Lyderic Bocquet. Ultralow liquid/solid friction in carbon nanotubes: Comprehensive theory for alcohols, alkanes, omcts, and water. *Lang.*, 28:14261–14272, 2012.

[188] G. Graziano, J. Klimeš, F. Fernandez-Alonso, and A. Michaelides. Improved description of soft layered materials with van der Waals density functional theory. *J. Phys.: Condens. Matter*, 24:424216, 2012.

[189] B. Hess, C. Kurzner, D van der Spoel, and E. Lindahl. Algorithms for Highly Efficient, Load-Balanced, and Scalable Molecular Simulation. *J. Chem. Theory Comput.*, 4:435, 2008.

[190] H. J. C. Berendsen, J. R. Grigera, and T. P. Straatsma. The missing term in effective pair potentials. *J. Phys. Chem.*, 91:6269, 1987.

[191] T. Werder, J. H. Walther, R. L. Jaffe, T. Halicioglu, and P. Koumoutsakos. On the Water–Carbon Interaction for Use in Molecular Dynam-

ics Simulations of Graphite and Carbon Nanotubes. *J. Phys. Chem. B*, 107:1345, 2003.

[192] A. Luzar and D. Chandler. Hydrogen-bond Kinetics in Liquid Water. *Nature*, 379:55, 1996.

[193] Chyuan-Yih Lee, J. Andrew McCammon, and P. J. Rossky. The structure of liquid water at an extended hydrophobic surface. *J. Chem. Phys.*, 80:4448–4455, 1984.

[194] Tuan A. Ho and Alberto Striolo. Polarizability effects in molecular dynamics simulations of the graphene-water interface. *J. Chem. Phys.*, 138(5):054117, 2013.

[195] Guillaume Stirnemann, Peter J. Rossky, James T. Hynes, and Damien Laage. Water reorientation, hydrogen-bond dynamics and 2D-IR spectroscopy next to an extended hydrophobic surface. *Faraday Discuss.*, 146:263–281, 2010.

[196] L. Bocquet and J. L. Barrat. Hydrodynamic boundary-conditions, correlation-functions, and kubo relations for confined fluids. *Phys. Rev. E*, 49:3079–3092, 1994.

[197] L. Bocquet and J. L. Barrat. On the green-kubo relationship for the liquid-solid friction coefficient. *J. Chem. Phys.*, 139:044704, 2013.

[198] Abdelhamid Maali, Touria Cohen-Bouhacina, and Hamid Kellay. Measurement of the slip length of water flow on graphite surface. *Appl. Phys. Lett.*, 92(5):053101, 2008.

[199] D. Ortiz-Young, H.-C. Chiu, S. Kim, K. Voïtchovsky, and E. Riedo. The interplay between apparent viscosity and wettability in nanoconfined water. *Nat. Commun.*, 4:24282, 2013.

[200] V. V. Gobre and A. Tkatchenko. Scaling laws for van der Waals interactions in nanostructured materials. *Nat. Commun.*, 4:2341, 2013.

[201] D. M. Huang, C. Sendner, D. Horinek, R. R. Netz, and L. Bocquet. Water slippage versus contact angle: A quasiuniversal relationship. *Phys. Rev. Lett.*, 101:226101, 2008.

[202] Tuan Anh Ho, Dimitrios V. Papavassiliou, Lloyd L. Lee, and Alberto Striolo. Liquid water can slip on a hydrophilic surface. *Proc. Natl. Acad. Sci. USA*, 108(39):16170–16175, 2011.

[203] J. Krim. Friction and energy dissipation mechanisms in adsorbed molecules and molecularly thin films. *Adv. Phys.*, 61(3):155–323, 2012.

[204] Kannam, Sridhar Kumar and Todd, B. D. and Hansen, J. S. and Daivis, Peter J. How fast does water flow in carbon nanotubes? *J. Chem. Phys.*, 138(9):094701, 2013.

[205] J. Ma, A. Michaelides, D. Alfè, L Schimka, G. Kresse, and E. Wang. Adsorption and Diffusion of Water on Graphene from First Principles. *Phys. Rev. B*, 84:003402, 2011.

[206] A. K. Geim and I. V. Grigorieva. Van der waals heterostructures. *Nature*, 499:419–425, 2013.

[207] Ming D. Ma, Luming Shen, John Sheridan, Jefferson Zhe Liu, Chao Chen, and Quanshui Zheng. Friction of water slipping in carbon nanotubes. *Phys. Rev. E*, 83:036316, 2011.

[208] C. L. Pang, R. Lindsay, and Geoff Thornton. Chemical Reactions on rutile TiO_2(110). *Chem. Soc. Rev.*, 66(6–7):185–297, 2011.

[209] U. Diebold. The surface science of titanium dioxide. *Surf. Sci. Rep.*, 48:53 – 229, 2003.

[210] F. Allegretti, S. O'Brien, M. Polcik, D. I. Sayago, and D. P. Woodruff. Adsorption bond length for h_2O on tio_2(110): A key parameter for theoretical understanding. *Phys. Rev. Lett.*, 95:226104, 2005.

[211] D. A. Duncan, F. Allegretti, and D. P. Woodruff. Water does partially dissociate on the perfect tio_2(110) surface: A quantitative structure determination. *Phys. Rev. B*, 86:045411, 2012.

[212] M. Amft, L. E. Walle, D. Ragazzon, A. Borg, P. Uvdal, N. V. Skorodumova, and A. Sandell. A Molecular Mechanism for the Water–Hydroxyl Balance during Wetting of TiO_2. *J. Phys. Chem. C*, 117(33):17078–17083, 2013.

[213] Nitin Kumar, Paul R. C. Kent, David J. Wesolowski, and James D. Kubicki. Modeling Water Adsorption on Rutile TiO_2(110) Using van der Waals Density Functional and DFT+U Methods. *J. Phys. Chem. C*, 117(45):23638–23644, 2013.

[214] Michael A. Henderson. A surface science perspective on photocatalysis. *Surf. Sci. Rep.*, 66(6–7):185–297, 2011.

[215] J. Goniakowski and M. J. Gillan. The adsorption of H_2O on TiO_2 and SnO_2(110) studied by first-principles calculations. *Surf. Sci.*, 350:145–158, 1996.

[216] Oier Bikondoa, C. L. Pang, Roslinda Ithnin, Christopher A. Muryn, Hiroshi Onishi, and Geoff Thornton. Direct visualization of defect-mediated dissociation of water on TiO_2(110). *Nat. Mater.*, 5(6–7):189–192, 2011.

[217] J. Matthiesen, S. Wendt, J. Hansen, G. K. H. Madsen, E. Lira, P. Galliker, E. K. Vestergaard, R. Schaub, E. Lægsgaard, B. Hammer, and F. Besenbacher. Observation of All the Intermediate Steps of a Chemical Reaction on an Oxide Surface by Scanning Tunneling Microscopy. *ACS Nano*, 3(3):517–526, 2009.

[218] H. H. Kristoffersen, J. Ø. Hansen, U. Martinez, Y. Y. Wei, J. Matthiesen, R. Streber, R. Bechstein, E. Lægsgaard, F. Besenbacher, B. Hammer, and S. Wendt. Role of steps in the dissociative adsorption of water on rutile tio_2(110). *Phys. Rev. Lett.*, 110:146101, 2013.

[219] L. E. Walle, A. Borg, P. Uvdal, and A. Sandell. Probing the influence from residual Ti interstitials on water adsorption on TiO_2(110). *Phys. Rev. B*, 86:205415, 2012.

[220] N. A. Deskins, R. Rousseau, and M. Dupuis. Defining the Role of

Excess Electrons in the Surface Chemistry of TiO_2. *J. Phys. Chem. C*, 114:5891–5897, 2010.

[221] B. J. Morgan and G. W. Watson. A DFT+U description of oxygen vacancies at the TiO_2 rutile (110) surface. *Surf. Sci.*, 601:5034, 2007.

[222] Xinchun Mao, Xiufeng Lang, Zhiqiang Wang, Qunqing Hao, Bo Wen, Zefeng Ren, Dongxu Dai, Chuanyao Zhou, Li-Min Liu, and Xueming Yang. Band-Gap States of TiO_2(110): Major Contribution from Surface Defects. *J. Phys. Chem. Lett.*, 4(22):3839–3844, 2013.

[223] A. Janotti, J. B. Varley, P. Rinke, N. Umezawa, G. Kresse, and C. G. Van de Walle. Hybrid functional studies of the oxygen vacancy in TiO_2. *Phys. Rev. B*, 81:085212, 2010.

[224] Livia Giordano, Jacek Goniakowski, and Jean Suzanne. Partial dissociation of water molecules in the (3×2) water monolayer deposited on the mgo (100) surface. *Phys. Rev. Lett.*, 81:1271–1273, 1998.

[225] Marek R. Włodarczyk Sierka, Karolina Kwapień, Joachim Sauer, Esther Carrasco, Andreas Aumer, Janaina F. Gomes, Martin Sterrer, and Hans-Joachim Freund. Structures of the Ordered Water Monolayer on MgO(001). *J. Phys. Chem. C*, 115:6764–6774, 2011.

[226] R. G. Pearson. Absolute electronegativity and hardness: application to inorganic chemistry. *Inorg. Chem.*, 27(4):734–740, 1988.

[227] Stefan Wendt, Phillip T. Sprunger, Estephania Lira, Georg K. H. Madsen, Zheshen Li, Jonas Hansen, Jesper Matthiesen, Asger Blekinge-

Rasmussen, Erik Lægsgaard, B. Hammer, and F. Besenbacher. The Role of Interstitial Sites in the Ti3*d* Defect State in the Band Gap of Titania. *Science*, 320:1755, 2008.

[228] Cristiana Di Valentin, Gianfranco Pacchioni, and Annabella Selloni. Electronic structure of defect states in hydroxylated and reduced rutile tio$_2$(110) surfaces. *Phys. Rev. Lett.*, 97:166803, 2006.

[229] A. Janotti, J. B. Varley, P. Rinke, N. Umezawa, G. Kresse, and C. G. Van de Walle. Hybrid functional studies of the oxygen vacancy in tio$_2$. *Phys. Rev. B*, 81:085212, 2010.

[230] A M. Saitta, F. Saija, and P. V. Giaquinta. *Ab initio* molecular dynamics study of dissociation of water under an electric field. *Phys, Rev. Lett.*, 108(20):207801, 2012.

[231] F. Schiffmann, J. VandeVondele, J. Hutter, A. Urakawa, R. Wirz, and A. Baiker. An atomistic picture of the regeneration process in dye sensitized solar cells. *Proc. Natl. Acad. Sci.*, 107(11):4830–4833, 2010.

[232] Michael Grätzel. Photoelectrochemical cells. *Nature*, 414:338, 2001.

[233] Annapaola Migani, Duncan J Mowbray, Amilcare Iacomino, Jin Zhao, Hrvoje Petek, and Angel Rubio. Level alignment of a prototypical photocatalytic system: Methanol on TiO_2(110). *J. Am. Chem. Soc.*, 135(31):11429–11432, 2013.

[234] Y. Ma, M. Rohlfing, and C. Molteni. Modeling the excited states of

biological chromophores within many-body green's function theory. *J. Chem. Theory Comput.*, 6(1):257–265, 2009.

[235] Stephen J. Cox, Zamaan Raza, Shawn M. Kathmann, Ben Slater, and Angelos Michaelides. The microscopic features of heterogeneous ice nucleation may affect the macroscopic morphology of atmospheric ice crystals. *Faraday Discuss.*, 167:389–403, 2013.

[236] Jun Cheng and Michiel Sprik. Alignment of electronic energy levels at electrochemical interfaces. *Phys. Chem. Chem. Phys.*, 14:11245–11267, 2012.

[237] Raffaele Resta. Macroscopic polarization in crystalline dielectrics: the geometric phase approach. *Rev. Mod. Phys.*, 66:899–915, Jul 1994.

[238] Manuel Guidon, JuÌĺrg Hutter, and Joost VandeVondele. Auxiliary density matrix methods for hartreeâĹŠfock exchange calculations. *Journal of Chemical Theory and Computation*, 6(8):2348–2364, 2010.

[239] Manuel Guidon, JÃijrg Hutter, and Joost VandeVondele. Robust periodic hartree-fock exchange for large-scale simulations using gaussian basis sets. *Journal of Chemical Theory and Computation*, 5(11):3010–3021, 2009.

[240] Jun Cheng, Xiandong Liu, John A. Kattirtzi, Joost VandeVondele, and Michiel Sprik. Aligning electronic and protonic energy levels of proton-coupled electron transfer in water oxidation on aqueous tio_2. *Angewandte Chemie International Edition*, 53(45):12046–12050, 2014.

Acknowledgements

I wish to thank all the people who supported me in the course of my PhD. In particular, I wish to thank my supervisor, Prof. Angelos Michaelides, for his constant guidance and useful discussions throughout my studies. I also owe to him the chance to work in a field of Science that I found fascinating ever since I have embarked on it, about four years ago. Thanks to his insights and suggestions I have significantly improved my overall skills as a scientist, and I have had the opportunity to attend to a number of very interesting workshops and conferences. I also thank my second supervisor Prof. Geoff Thornton for his insights into the interesting experiments performed in his group. I wish to thank Prof. Laurent Joly, for sharing his expertise on nanoscale liquid transport during his visit in our group.

My thanks go also to all the members to the ICE group that I have met during my stay here: Xinzheng, Thor, Ming, Jiri, Brent, Erlend, Nanaxhi, Wei, Philipp, Chiara, Yasmine, Steve and Gabriella. Not only did I learn a lot during our discussions, but I have also had good fun with them. I wish to thank the Marie Curie "SMALL Initial Training Network", for making me be part of this great network and for funding my studies. Finally, I thank my parents for all their support and encouragement and Sara, my love.